Karlsruher Institut für Technologie

Tailored Light Scattering and Emission in Solar Cells and LEDs Using Ordered and Disordered Interfaces

Zur Erlangung des akademischen Grades eines
Doktors der Naturwissenschaften
(Dr. rer. nat.)

von der KIT-Fakultät für Physik
des Karlsruher Instituts für Technologie (KIT)

angenommene

DISSERTATION

von

M. Sc. Stefan Nanz

Datum der mündlichen Prüfung: 7. Juni 2019

Referent: Prof. Dr. Carsten Rockstuhl
Korreferent: Prof. Dr. Ulrich Lemmer

Publications

Publications whose contents is part of this thesis are highlighted in **bold**.

1. A. Abass, M. Zilk, S. Nanz, S. Fasold, S. Ehrhardt, T. Pertsch, and C. Rockstuhl: *A Green's function based analytical method for forward and inverse modeling of quasi-periodic nanostructured surfaces*. Journal of Applied Physics, **122** (18), 183103, 2017.
2. **H. Chen, S. Nanz, A. Abass, J. Yan, T. Gao, D.-Y. Choi, Y. S. Kivshar, C. Rockstuhl, and D. N. Neshev: *Enhanced Directional Emission from Monolayer* WSe_2 *Integrated onto a Multiresonant Silicon-Based Photonic Structure*. ACS Photonics, 4 (12), 3031–3038, 2018.**
3. **S. Nanz, A. Abass, P. M. Piechulla, A. Sprafke, R. B. Wehrspohn, and C. Rockstuhl: *Strategy for tailoring the size distribution of nanospheres to optimize rough backreflectors of solar cells*. Optics Express, 26 (2), A111–A123, 2018.**
4. **P. M. Piechulla, L. Muehlenbein, R. B. Wehrspohn, S. Nanz, A. Abass, C. Rockstuhl, and A. Sprafke: *Fabrication of Nearly-Hyperuniform Substrates by Tailored Disorder for Photonic Applications*. Advanced Optical Materials, 6 (7), 1701272, 2018.**
5. **S. Nanz, A. Abass, P. M. Piechulla, A. Sprafke, R. B. Wehrspohn, and C. Rockstuhl: *Light-Trapping Front Textures for Solar Cells from Tailored Mixtures of Nanospheres: A Numerical Study*. Physica Status Solidi A, 215 (24), 1800699, 2018.**
6. **A. Vaskin, S. Mashhadi, M. Steinert, K. E. Chong, D. Keene, S. Nanz, A. Abass, E. Rusak, D.-Y. Choi, I. Fernandez-Corbaton, T. Pertsch, C. Rockstuhl, M. A. Noginov, Y. S. Kivshar, D. N. Neshev, N. Noginova, and I. Staude: *Manipulation of Magnetic Dipole Emission from* Eu^{3+} *with Mie-Resonant Dielectric Metasurfaces*. Nano Letters, 19 (2), 1015–1022, 2019.**
7. **S. Nanz, R. Schmager, M. G. Abebe, C. Willig, A. Wickberg, A. Abass, G. Gomard, M. Wegener, U. W. Paetzold, and C. Rockstuhl: *Photon Recycling in Nanopatterned Perovskite Thin-Films for Photovoltaic Applications*. APL Photonics, 4 (7), 076104, 2019.**
8. A. Abass, A. Martins, S. Nanz, B.-H. V. Borges, E. R. Martins, and C. Rockstuhl: *Perturbing beyond the shallow amplitude regime: Green's function scattering formalism with Bloch modes*. Journal of the Optical Society of America B, **36** (8), F89–F98, 2019.

Conference Contributions

Conference contributions with presentations done by myself are highlighted in **bold**.

1. **S. Nanz, A. Abass, and C. Rockstuhl: *An Analytical Method to Describe Quasi-Periodic and Aperiodic Light Trapping Structures*. PhotoVoltaic Technical Conference, Marseille, France, May 2016.**
2. **S. Nanz, A. Abass, P. M. Piechulla, A. Sprafke, R. B. Wehrspohn, and C. Rockstuhl: *Absorption enhancement using surface textures defined by a monolayer of tailored nanospheres*. Optical Nanostructures and Advanced Materials for Photovoltaics, Leipzig, Germany, November 2016.**
3. A. Abass, S. Nanz, and C. Rockstuhl: *A Green's Function Based Inverse Method to Perceive Gratings that Critically Couple Light into Solar Cells*. Optical Nanostructures and Advanced Materials for Photovoltaics, Leipzig, Germany, November 2016.
4. H. Chen, S. Nanz, A. Abass, J. Yan, T. Gao, D.-Y. Choi, C. Rockstuhl, Y. S. Kivshar, and D. N. Neshev: *Enhanced and directional photoluminescence from doubly-resonant* WSe$_2$-Si *hybrid structure*. CLEO: Applications and Technology, San Jose, California, United States, May 2017.
5. **S. Nanz, A. Abass, C. Rockstuhl: *Tailored Disorder of Scattering Interfaces*, Karlsruhe Days of Optics & Photonics, Karlsruhe, Germany, November 2017**
6. P. M. Piechulla, L. Muehlenbein, S. Nanz, A. Abass, A. Sprafke, C. Rockstuhl, and R. B. Wehrspohn: *Tailored substrate topographies by self-organized colloidal particles*. Optical Nanostructures and Advanced Materials for Photovoltaics, Boulder, Colorado, United States, November 2017.
7. **S. Nanz, A. Abass, P. M. Piechulla, A. Sprafke, R. B. Wehrspohn, and C. Rockstuhl: *Tailoring Nanospheres for Rough Interfaces in Solar Cells*. 11th Annual Meeting Photonic Devices, ZIB, Berlin, Germany, February 2018.**
8. A. Vaskin, S. Mashhadi, N. Noginova, K. E. Chong, S. Nanz, A. Abass, I. Fernandez-Corbaton, E. Rusak, M. A. Noginov, Y. S. Kivshar, D. Keene, C. Rockstuhl, T. Pertsch, D. Neshev, and I. Staude: *Manipulation of electric and magnetic dipole emission from* Eu^{3+} *with silicon metasurfaces*. DPG spring meeting, Berlin, Germany, March 2018.
9. **S. Nanz, A. Abass, P. M. Piechulla, A. Sprafke, R. B. Wehrspohn, and C. Rockstuhl: *Strategy for tailoring nanospheres for rough interfaces in solar cells*. SPIE Photonics Europe, Strasbourg, France, April 2018.**
10. A. Abass, S. Nanz, P. M. Piechulla, A. Sprafke, R. B. Wehrspohn, and C. Rockstuhl: *Tailoring disordered structures for light management*. 20th International Conference on Transparent Optical Networks, Bucharest, Romania, July 2018.
11. **S. Nanz, R. Schmager, A. Abass, M. G. Abebe, G. Gomard, U. W. Paetzold, and C. Rockstuhl: *Rigorous Wave-Optical Simulation of Photon Recycling in Nanostructured Perovskite Solar Cells*. OSA Light, Energy and Environment Congress, Singapore, November 2018.**

Abstract

Solar cells are an integrated part of our strategy to undergo the transition from an energy supply that relies on fossil energy sources to a supply that relies on renewable ones. A large fraction of solar cells nowadays available is based on silicon. While the fabrication of silicon solar cells has a long history and is, therefore, highly optimized, there is a continuous effort to further increase solar cell efficiency by means of new materials and designs. Among these heavily investigated topics are thin-film solar cells, that promise to widen the possible applications of solar cells to mobile devices, cars, and building-integrated systems. Thin-film solar cells are characterized by absorber layers with thicknesses down to only a few micrometers. However, decreasing the thickness of the absorber layer negatively affects the generated short-circuit current density and with that the total efficiency.

To mitigate this problem, advanced nanostructures are required to improve the photon management in thin-film solar cells. Such nanostructures are typically combined within the front or back textures in solar cell multilayers. For optimal efficiency, the nanostructures should provide a spectrally broad increase of the short-circuit current density. As it got more and more apparent, this can be achieved with rough disordered textures. Among inexpensive fabrication methods of such nanostructures, bottom-up approaches are particularly useful, since the building blocks assemble themselves to the desired structures. Here, we will present results of the analysis of a bottom-up approach that inherently enables to tailor the disorder of the resulting nanostructured interfaces to achieve favorable light-trapping properties. We will also offer an analysis of the often neglected mechanism of photon recycling in solar cells. For this, we will use the relatively new and highly luminescent material class of perovskites.

Besides efficient energy production, energy-saving light sources which are also tunable in their properties are increasing their market share in the recent years. Compared to the long-standing light bulbs, light-emitting diodes can be engineered to emit light in a tailored wavelength range. While such light sources are already quite energy-efficient, they often suffer from losses in the total luminescence yield due to internal absorption or unsufficient light-outcoupling. Furthermore, the emitting materials often show intrinsically low luminescence, and photonic environments to enhance the luminescence are desired. Here, we address these problems by investigating the photoluminescence enhancement of an electric dipole near a textured waveguide multilayer structure. We also consider a spectrally close magnetic and electric dipole emission of a different emitter. By engineering a grating structure in the vicinity of this emitter, we can demonstrate a relative enhancement of the magnetic dipole emission compared to the electric dipole emission.

In summary, we show in this thesis that the advanced and tailored design of nanostructures is an important resource to engineer the interaction of light with matter.

Contents

1 Introduction

> *Everything of importance has been said before by somebody who did not discover it.*
> ALFRED NORTH WHITEHEAD

With time passing, it has been more and more appreciated that the way we have been generating and the way we have been using energy can no longer continue just like it has been in the recent decades. Fossil sources of energy come to an end and global warming caused by an ever increasing emission of CO_2 are a clear indication that things have to change. Photonic technologies can contribute to the solution of some of these problems that are of societal importance. The exploration of the basic principles and the engineering of devices associated to these problems is a prime research goal and at stake in this thesis. For example, a large and continuously increasing amount of the energy consumption all over the world can be fed by photovoltaic systems that convert solar energy into electric energy, either in private setups or operated by companies. Also, light-emitting diodes (LEDs) form the basis of modern telecommunication displays, urban and traffic lightning, while being much more energy-efficient and versatile when compared to classical light sources. The improvement of such devices by specific means will be explored in this thesis. Both types of devices, solar cells and LEDs, have undergone already quite some developments in the past, but there continues to be plenty of room for improvements.

The technological processes for the fabrication of solar cells, for example, are optimized and rationalized to a very high degree. Beginning in the 1980s, the rise of solar cells was possible thanks to the exploitation of fabrication experiences from the microelectronics industry. Since the 2000s, a growing number of governments made efforts to increase the fraction of solar energy in the total energy production. Most notably, in the course of time solar cells changed from a high-tech product that used to be very expensive to a mass product with huge fabrication capabilities that turn out to be rather inexpensive. While more and more absorber materials entered the research and the market, silicon remained the most frequently used material, mainly because of its optimized fabrication process.

Nevertheless, there is always the desire to improve the efficiency even further and to push it towards fundamental limits. One way to lower the cost-per-watt ratio of solar cells is to decrease the thickness of the silicon while retaining the efficiency on a high level. This is the driving idea behind the transition from thick wafer-based solar cell devices to thin-film cells. Thinner absorber layers are also accompanied with increased mechanical flexibility and portability [1].

However, a thinner absorber layer is rather detrimental with respect to the total absorbed power, since the optical path in the light absorbing layer is shortened. To retain a high efficiency, nanostructures can be used that enhance the effective light path and increase with that the absorption. Unfortunately, the fabrication of nanostructures can be very difficult and expensive, especially if the special needs that solar cells have are considered. Due to their broadband nature across the entire visible wavelength range and beyond, simple periodic gratings are not sufficient to increase the absorption significantly. Alternatively, broadband light-trapping can be achieved by using randomly rough textured interfaces. However, the degree of disorder of such textures has to be engineered carefully to achieve a good light-trapping efficiency. As a consequence, the fabrication of these interfaces is typically done with top-down methods that suffer from high-fabrication costs and are not readily scalable to large-scale devices.

To tie together the advantages of bottom-up approaches and the possibility to tailor the required degree of disorder, a fabrication scheme has been proposed where nanospheres are used as building blocks [2]. The nanospheres are immersed in a colloidal solution, which is then deposited onto a substrate. By tuning the parameters of the colloidal solution and the substrate, one can achieve the formation of a monolayer of nanospheres with a suitable topography [3]. In this way, the roughness of the resulting height profile can directly be controlled by the radii of the nanospheres. As we will show in this thesis, textures that can be fabricated with such an approach are suitable for both front anti-reflection structures, but also back reflectors in solar cell multilayers. Using a bottom-up approach could help to overcome expensive and size-limited fabrication and potentially yield a fabrication scheme suitable for large-scale applications.

According to Kirchhoff's law of thermal radiation, every material body that absorbs light also emits radiation. This is of course detrimental for solar cell devices. While for silicon, the photoluminescence is negligible, it can noticeably affect the efficiency in more contemporary materials of interest such as the perovskites, since there the radiative recombination is a relatively strong effect [4]. The emission of radiatively generated photons may be impaired by suitably engineering the solar cell geometry. In this context, the reabsorption of a previously generated photon via recombination of an electron and hole is known as photon recycling [5–8]. Photon recycling bears conceptual possibilities for improving the efficiency of solar cells. Therefore, it is important to understand also how nanostructures affect the light emission from perovskite thin-films and it will be explored in this thesis.

The light extraction from LEDs is another major research topic. Not only the portion of outcoupled light, also the wavelengths and the directionality are heavily investigated. In this thesis, we will contribute to this research by analyzing two systems where the photoluminescence of dipole emitters is enhanced and, in one case, strongly directional. With silicon being the most important material for chip fabrication, silicon renders an important material to constitute the photonic environment of light-emitting materials and to engineer their emission properties at on-chip optoelectronic applications [9–11]. Appreciating this necessity, we investigate a transition metal dichalcogenide monolayer (TMDC) when used as emission source. Being placed in the spatial proximity of a silicon waveguide multilayer, we demonstrate enhanced and directional emission. In a second approach, an array of silicon nanodisks is used to enhance the emission of the magnetic dipole transition of a lanthanide ion as compared to the electric dipole transition of the same ion.

Structure of the Thesis

This thesis has five main chapters. After the introduction in chapter 1, the theory that is required to understand the remainder of the thesis is laid out in chapter 2. We will first introduce quantities that are specifically relevant for the discussion and analysis of the near- and far-field. We will introduce the Bloch theorem for periodic structures and a related method that allows reconstructing a single-dipole response placed inside a grating structure from many calculations using periodically arranged dipole emitters. Afterwards, the physics of waveguides is laid out and grating couplers as an important tool for applications are introduced. We will then finish the analytical foundations and elucidate the working principle of solar cells and light-emitting structures. Last but not least, we will introduce the Finite Element Method as one of the most important numerical methods to solve Maxwell's equations.

Chapter 3 focuses on optimizing interfaces in solar cell devices by looking at the far-field. Core of the study is a bottom-up approach that employs nanospheres, whose sizes and occurrence fractions are tailored such that a monolayer fabricated from the nanospheres possesses desired scattering properties. We will particularly analyze this bottom-up approach with respect to light-trapping and anti-reflection front textures in solar cells. Using both the real space and the Fourier space, we will identify guidelines in which parameter regimes the nanospheres should be chosen to provide favorable results. We also show that the computational expensive calculation of the short-circuit current density can be reduced to a single diffraction simulation at a wavelength that is relevant for light-trapping purposes.

In chapter 4, the near-field of dipolar emitters is considered and the implications of the photonic environment on the far-field of the emission is investigated. First, the undesired photon reemission in solar cell absorber layers is studied and the second order process of photon recycling is quantitatively analyzed in a typical perovskite solar cell geometry. We will show that photon recycling yields a relevant contribution to the open-circuit voltage and should therefore be considered in optimization procedures of solar cell geometries. Afterwards, light emission is discussed in contexts that are particularly envisioned for LEDs. In this respect, we investigate the enhanced and strong directional pattern of the photoluminescence of an electric dipole near a textured multilayer waveguide. We resolve the origin of the PL enhancement as due to an increase of the local density of states at both the pump and emission wavelength. As we further show, the directional emission can be directly linked to guided modes sustained in the multilayer system. Last but not least, a spectrally close magnetic and electric dipole transition is analyzed. Measurements show an enhancement of the magnetic dipole emission as compared to the electric dipole emission for a specifically engineered photonic environment. Exploiting the duality of Maxwell's equations in our simulations, we perform calculations to numerically reproduce these results. Additionally, the far-field spectra of the dipole emission is calculated.

Finally, chapter 5 provides a summary of the discussed topics. It offers a holistic view on the results and also provides an outlook for further research possibilities.

2 Theory and Computational Methods

This chapter shall serve as a starting point to unfold the research results in the further chapters. We lay out the most important formulae from electromagnetic theory and various relations that will be needed at a later stage. Furthermore, the applications that were the main subject of research are introduced from a perspective useful for later analyses. At the end of the chapter, the reader should have a state-of-the-art overview.

2.1 Basic Electromagnetic Theory

This section summarizes equations governing the propagation of electromagnetic waves. We start from describing Maxwell's equations and continue from there to discuss the Poynting theorem and the Fresnel equations. The section closes by writing down the duality transformation of Maxwell's equations that will be applied in Sec. 4.3.

2.1.1 Maxwell's Equations and Helmholtz Equation

We want to begin by writing down the equations which this thesis revolves around: the Maxwell equations. They are solved for given initial or boundary conditions. Assuming vacuum for the moment as the medium in which the electromagnetic fields evolve, they are in differential form and in space-time domain explicitly given by [12]

$$\vec{\nabla} \cdot \vec{E}(\vec{r},t) = \frac{1}{\varepsilon_0}\rho(\vec{r},t)\,, \tag{2.1}$$

$$\vec{\nabla} \times \vec{E}(\vec{r},t) = -\frac{\partial}{\partial t}\vec{B}(\vec{r},t)\,, \tag{2.3}$$

$$\vec{\nabla} \cdot \vec{B}(\vec{r},t) = 0\,, \tag{2.2}$$

$$\vec{\nabla} \times \vec{B}(\vec{r},t) = \mu_0\vec{j}(\vec{r},t) + \mu_0\varepsilon_0\frac{\partial}{\partial t}\vec{E}(\vec{r},t)\,. \tag{2.4}$$

Equation 2.3 is also called Faraday's law and Eq. 2.4 is Maxwell's version of Ampere's law. Equation 2.1 is Gauss's law and Eq. 2.2 is Gauss's law for magnetism. ε_0 is the vacuum permittivity and μ_0 is the vacuum permeability. For the systems focused on in this thesis, it is useful to consider Maxwell's equations in the frequency domain. Using the Fourier decomposition

$$\vec{E}(\vec{r},t) = \frac{1}{\sqrt{2\pi}}\int \mathrm{e}^{-\mathrm{i}\omega t}\tilde{\vec{E}}(\vec{r},\omega)\,\mathrm{d}\omega \tag{2.5}$$

for the fields and the sources, Maxwell's equations can be written as

$$\vec{\nabla} \cdot \tilde{\vec{E}}(\vec{r},\omega) = \frac{1}{\varepsilon_0}\tilde{\rho}(\vec{r},\omega)\,, \tag{2.6}$$

$$\vec{\nabla} \times \tilde{\vec{E}}(\vec{r},\omega) = \mathrm{i}\omega\tilde{\vec{B}}(\vec{r},\omega)\,, \tag{2.8}$$

$$\vec{\nabla} \cdot \tilde{\vec{B}}(\vec{r},\omega) = 0\,, \tag{2.7}$$

$$\vec{\nabla} \times \tilde{\vec{B}}(\vec{r},\omega) = \mu_0\tilde{\vec{j}}(\vec{r},\omega) - \mathrm{i}\mu_0\varepsilon_0\omega\tilde{\vec{E}}(\vec{r},\omega)\,. \tag{2.9}$$

From now on, we will, for clarity of the notation, omit the tilde. It will become clear from the arguments of the fields which quantity is referred to. The propagation of electromagnetic waves can be described with the Helmholtz equation that one can obtain by taking the curl of Eq. 2.8 and using Eqs. 2.6 and 2.9 to arrive at

$$\vec{\nabla}^2 \vec{E}(\vec{r},\omega) + k_0^2(\omega)\vec{E}(\vec{r},\omega) = \frac{1}{\varepsilon_0}\vec{\nabla}\rho(\vec{r},\omega) - \mathrm{i}\omega\mu_0\vec{j}(\vec{r},\omega)\,, \tag{2.10}$$

where we defined the wavenumber $k_0 = \frac{\omega}{c} = \omega\sqrt{\varepsilon_0\mu_0}$ with c the speed of light in vacuum. The solutions of the homogeneous case, i. e. without charges and currents, are elliptically polarized plane waves that have a spatial dependency according to

$$\vec{E}(\vec{r},\omega) = \vec{\mathscr{E}}_1(\omega)\mathrm{e}^{\mathrm{i}\vec{k}_0(\omega)\cdot\vec{r}} + \vec{\mathscr{E}}_2(\omega)\mathrm{e}^{-\mathrm{i}\vec{k}_0(\omega)\cdot\vec{r}}\,, \tag{2.11}$$

where the vectorial amplitudes $\vec{\mathscr{E}}_1(\omega)$ and $\vec{\mathscr{E}}_2(\omega)$ depend on the specific initial and boundary conditions and the angular frequency.

In a homogeneous medium that can be described with a macroscopic isotropic permittivity $\varepsilon(\omega) = \varepsilon_0\,\varepsilon_r(\omega)$ and permeability $\mu(\omega) = \mu_0\,\mu_r(\omega)$, the vacuum wavenumber $k_0(\omega)$ is exchanged by the medium wavenumber $k(\omega) = k_0(\omega)\sqrt{\varepsilon_r(\omega)\mu_r(\omega)}$. The systems under consideration in this thesis only consist of non-magnetic media with $\mu_r = 1$, so that it holds $\vec{B} = \mu_0\vec{H}$ and we can use $\vec{B}$ and $\vec{H}$ essentially interchangeably.

For a nonmagnetic and isotropic medium, the general refractive index is related to the dielectric function $\varepsilon(\omega)$ via $\varepsilon(\omega) = \mathcal{n}^2(\omega)$, where

$$\mathcal{n}(\omega) = n(\omega) + \mathrm{i}\kappa(\omega) \tag{2.12}$$

has a real part corresponding to the refractive index $n(\omega)$ and an imaginary part corresponding to the extinction coefficient $\kappa(\omega)$.

The electric and magnetic fields are not directly observable, and one is typically interested in the power flow due to the electromagnetic field. This is expressed with the Poynting vector, which is defined as [12]

$$\vec{S}(\vec{r},t) = \Re\{\vec{E}(\vec{r},t)\} \times \Re\{\vec{H}(\vec{r},t)\}\,. \tag{2.13}$$

In experiments, detectors can only measure the field intensity, which corresponds to the time-averaged Poynting vector $\langle\vec{S}(\vec{r},t)\rangle$. For a monochromatic field at angular frequency ω_0, $\langle\vec{S}(\vec{r},t)\rangle$ is given by

$$\langle\vec{S}(\vec{r},\omega_0)\rangle = \frac{1}{2}\Re\{\vec{E}(\vec{r},\omega_0) \times \vec{H}^*(\vec{r},\omega_0)\}\,. \tag{2.14}$$

In many applications, one is interested in the amount of absorbed power in some spatial region. According to the general divergence theorem of Gauss, this can be expressed with an integral of the power flow over the surface of the respective volume [13]:

$$\int \langle\vec{S}(\vec{r},\omega)\rangle \cdot \mathrm{d}\vec{A} = -\frac{1}{2}\int \Re\left\{\vec{j}^*(\vec{r},\omega)\cdot\vec{E}(\vec{r},\omega)\right\}\,\mathrm{d}V\,. \tag{2.15}$$

This is also known as Poynting's theorem.

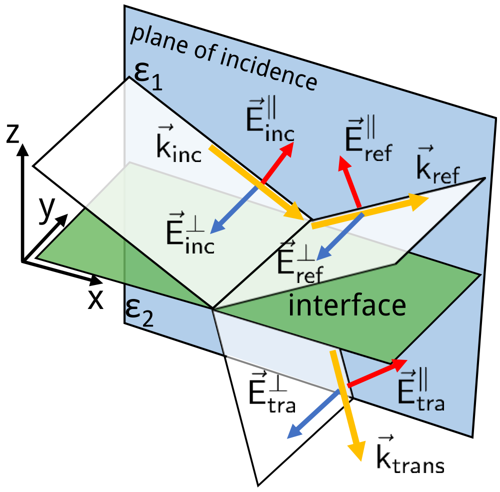

Figure 2.1: Illustration of the decomposition of an electric field $\vec{E}_{\mathrm{inc}}$ incident onto a planar interface (green area) between two media with permittivities ε_1 and ε_2. The wavevector (yellow) and the normal vector of the interface span the plane of incidence (blue), in which the parallel component $\vec{E}^{||}_{\mathrm{inc}}$ lies. The perpendicular field component $\vec{E}^{\perp}_{\mathrm{inc}}$ lies in the same plane as the wavevector and the normal vector of the plane of incidence. $\vec{E}^{||}_{\mathrm{ref}}$ and $\vec{E}^{||}_{\mathrm{tra}}$ correspond to the component of the reflected and transmitted field parallel to the plane of incidence, respectively. Similarly, $\vec{E}^{\perp}_{\mathrm{ref}}$ and $\vec{E}^{\perp}_{\mathrm{tra}}$ correspond to the perpendicular component of the reflected and transmitted field.

2.1.2 Relations for Interfaces

For actual problems, the propagation of electromagnetic fields in the presence of media and interfaces has to be considered. An arbitrary electric field that impinges on an interface can be decomposed into components parallel and perpendicular to the plane of incidence (see Fig. 2.1). The parallel component is denoted with $\hat{p}$ or p, the perpendicular component with $\hat{s}$ or s. Let the interface lie in the x-y-plane and the light be incident from the positive z-direction, then the polarization unit vectors are calculated as

$$\hat{s} = \hat{k} \times \hat{z} \quad \text{and} \quad \hat{p} = \hat{k} \times \hat{s}\,, \tag{2.16}$$

where $\hat{k} = \frac{\vec{k}}{k}$ is the unit vector in the direction of the wavevector. Often, one uses the terms "transverse electric" (TE) instead of s-polarization and "transverse magnetic" (TM) instead of p-polarization. In this thesis we will use both termini.

In general, the different impedances of two adjacent media determine the fraction of reflected and transmitted power. For flat interfaces, the reflection and transmission can be calculated by virtue of the Fresnel equations. For non-magnetic media, the Fresnel reflection coefficients for the amplitudes of p- and s-polarized electric fields are

$$r_{\mathrm{s}} = \frac{n_1 \cos\theta_{\mathrm{i}} - n_2 \cos\theta_{\mathrm{t}}}{n_1 \cos\theta_{\mathrm{i}} + n_2 \cos\theta_{\mathrm{t}}}\,, \tag{2.17}$$

$$r_{\mathrm{p}} = \frac{n_1 \cos\theta_{\mathrm{t}} - n_2 \cos\theta_{\mathrm{i}}}{n_1 \cos\theta_{\mathrm{t}} + n_2 \cos\theta_{\mathrm{i}}}\,. \tag{2.18}$$

Here, θ_{i} (θ_{t}) is the angle of the incident (transmitted) electric field. The reflectance coefficient for the power is calculated as

$$R = |r|^2\,. \tag{2.19}$$

For the transmission coefficients of the amplitudes of p- and s-polarized electric fields, it holds

$$t_\mathrm{s} = r_\mathrm{s} + 1\,, \tag{2.20}$$

$$t_\mathrm{p} = \frac{n_1}{n_2}(r_\mathrm{p} + 1)\,, \tag{2.21}$$

as well as

$$T = \left| \Re \left\{ \frac{n_2 \cos\theta_\mathrm{t}}{n_1 \cos\theta_\mathrm{i}} \right\} \right| |t|^2\,. \tag{2.22}$$

In the absence of absorption, it always holds

$$R + T = 1\,. \tag{2.23}$$

Snell's law of refraction gives a relation between the incoming and transmission angle for two media with different refractive indices. Considering only non-absorbing media, it holds

$$n_1 \sin\theta_\mathrm{i} = n_2 \sin\theta_\mathrm{t}\,, \tag{2.24}$$

where n_1 and n_2 are the refractive indices of the incident and transmitted medium, respectively (cf. Fig. 2.1). The physical origin of this relation is the conservation of the photon momentum parallel to the interface [14]. If medium 1 has a higher refractive index as medium 2, there is a maximal angle under which a wave that impinges the interface between the two media can still propagate in medium 2. For a maximum transmission angle $\theta_\mathrm{t} = 90°$, the critical angle of incidence is

$$\theta_\mathrm{c} = \arcsin\frac{n_2}{n_1}\,, \tag{2.25}$$

and for larger angles, all light will be reflected. For example, for light travelling from glass ($n_1 = 1.45$) into air ($n_2 = 1$), $\theta_\mathrm{c} = 43.6°$. Another example relevant for this thesis is the silicon/air interface. At a wavelength of 700 nm, the refractive index of silicon is $n_\mathrm{Si} = 3.77$ [15], which yields for the critical angle of light that can leave the silicon $\theta_\mathrm{c} = 15.26°$.

2.1.3 Duality Symmetry of Maxwell's Equations

To prepare the reader for a later section where we will analyze the emission of a magnetic dipole, we will briefly introduce the concept of duality.

In the absence of charges and currents, Maxwell's equations 2.1–2.4 are symmetric under the following transformation of the $\vec{E}$ and $\vec{H}$ field [16, 17]:

$$\vec{E}_\theta(\vec{r},t) = \vec{E}(\vec{r},t)\cos\theta - Z_0\vec{H}(\vec{r},t)\sin\theta\,, \tag{2.26}$$

$$\vec{H}_\theta(\vec{r},t) = \frac{1}{Z_0}\vec{E}(\vec{r},t)\sin\theta + \vec{H}(\vec{r},t)\cos\theta\,. \tag{2.27}$$

θ is an arbitrary real angle. Symmetric means here that if $(\vec{E}, \vec{H})$ is a solution of Maxwell's equations, then $(\vec{E}_\theta, \vec{H}_\theta)$ is also a solution. For $\theta = \frac{\pi}{2}$, one obtains the special case

$$\vec{E}_\theta(\vec{r},t) = -Z_0\vec{H}(\vec{r},t)\,, \tag{2.28}$$

$$\vec{H}_\theta(\vec{r},t) = \frac{1}{Z_0}\vec{E}(\vec{r},t)\,, \tag{2.29}$$

where $\vec{E}$ and $\vec{H}$ exchange their role up to the prefactor $Z_0 = \sqrt{\frac{\mu_0}{\varepsilon_0}}$, which is the vacuum impedance. If matter with permittivity ε and permeability μ is present, one also needs to perform the transformation

$$\varepsilon \to \mu\,, \tag{2.30}$$

$$\mu \to \varepsilon\,. \tag{2.31}$$

Using this set of transformations, one can e. g. calculate the electromagnetic fields of a magnetic dipole by actually calculating the electromagnetic fields of an electric dipole, but exchanging permeability and permittivity of the surrounding environment. This feature of Maxwell's equations will be exploited in Sec. 4.3.

2.2 Green's Tensor and Near-Field Quantities

In this section, we will introduce the Green's tensor and outline important aspects related to the electromagnetic near-field. The section introduces, in the context of quantum emitters, the local density of states, the decay rate, and the Purcell effect. Also, a few examples are given for the Green's tensor of simple geometries for which analytical expressions can be provided. Besides those simple examples and in general, only numerical solutions can be obtained.

2.2.1 Green's Tensor

An optical system is fully characterized by its electromagnetic Green's tensor. An advantage of using the Green's tensor is that it has to be determined only once for a geometrical system, and can then be used to calculate the electric and magnetic field of an arbitrary source within this geometry. From the Green's tensor, various observable quantities can be derived, for example the power that is radiatively emitted from a localized source.

For a non-magnetic system ($\mu_r = 1$), the Green's tensor is the solution of the Helmholtz equation (Eq. 2.10) with a delta function as source term [18]:

$$\vec{\nabla} \times \vec{\nabla} \times \overset{\leftrightarrow}{\mathbb{G}}(\vec{r},\vec{r}_0,\omega) - k_0^2(\omega)\varepsilon(\vec{r},\omega)\,\overset{\leftrightarrow}{\mathbb{G}}(\vec{r},\vec{r}_0,\omega) = \mathbb{1}\delta(\vec{r}-\vec{r}_0)\,, \tag{2.32}$$

where the boundary condition $\overset{\leftrightarrow}{\mathbb{G}}(\vec{r},\vec{r}_0) \to 0$ for $|\vec{r}-\vec{r}_0| \to \infty$ has to be fulfilled additionally.

The quantity $\overset{\leftrightarrow}{\mathbb{G}}$ is called the Green's tensor; it is a 3×3 dyad. This is due to the fact that every source of electromagnetic fields can be represented as a superposition of three sources oriented in either x-, y-, or z-direction, respectively. Then, the individual orientiations cause each an electric field with x-, y-, and z-components. In the simplest case, vacuum, the tensor is given by

$$\overset{\leftrightarrow}{\mathbb{G}}(\vec{r},\vec{r}_0,\omega) = \left(\mathbb{1} + \frac{\mathrm{i}k_0R - 1}{k_0^2R^2}\mathbb{1} + \frac{3 - 3\mathrm{i}k_0R - k_0^2R^2}{k_0^2R^4}\vec{R} \otimes \vec{R}\right)\frac{\mathrm{e}^{\mathrm{i}k_0R}}{4\pi R}\,. \tag{2.33}$$

$R = |\vec{r} - \vec{r}_0|$ is the distance of the observer at point $\vec{r}$ from a source at point $\vec{r}_0$, and $\vec{R} \otimes \vec{R}$ is the dyadic product of two vectors that yields a 3×3 matrix.

For systems where scattering objects of any kind are present, the solution of the Helmholtz equation (Eq. 2.10) can be decomposed into the solution of the homogeneous case (with delta function as source term) and the particular solution, which is only there due to the scattering object [19]. The Green's tensor is then written as

$$\overset{\leftrightarrow}{\mathbb{G}}(\vec{r},\vec{r}_0,\omega) = \overset{\leftrightarrow}{\mathbb{G}}^{(0)}(\vec{r},\vec{r}_0,\omega) + \overset{\leftrightarrow}{\mathbb{G}}^{(1)}(\vec{r},\vec{r}_0,\omega)\,. \tag{2.34}$$

$\overset{\leftrightarrow}{\mathbb{G}}^{(0)}(\vec{r},\vec{r}_0,\omega)$ is the Green's tensor of the homogeneous case and $\overset{\leftrightarrow}{\mathbb{G}}^{(1)}(\vec{r},\vec{r}_0,\omega)$ essentially contains the part of the electromagnetic field that arises due to the reflections at the boundaries or in the interior of the scattering object.

In this thesis, mostly multilayer systems as exemplarily depicted in Fig. 2.2 are analyzed. For such a geometry, the Green's tensor is derived by first expressing the Green's tensor of a homogeneous background (Eq. 2.33) in terms of plane waves by a Fourier transform [18]:

$$\overset{\leftrightarrow}{\mathbb{G}}(\vec{r},\vec{r}_0,\omega) = -\frac{\hat{z}\hat{z}}{k^2}\delta(\vec{r} - \vec{r}_0) + \frac{\mathrm{i}}{8\pi^2k^2}\int\int \mathrm{d}k_x\,\mathrm{d}k_y \frac{\mathbb{1}k^2 - \vec{k} \otimes \vec{k}}{k_z}\mathrm{e}^{\mathrm{i}\vec{k}\cdot(\vec{r}-\vec{r}_0)}\,. \tag{2.35}$$

The first term is the singular part that only contributes at the position of the source. Fields that propagate purely parallel to the interface, i. e. $k_z = 0$, are called guided modes [20]. For a more detailed analysis of guided modes, we refer to Sec. 2.4.

Additional layers would be taken into account in the Green's tensor by considering all plane waves that result from multiple reflections at all interfaces. The reflections depend on the polarization, and to be able to use the Fresnel equations (Eq. 2.18), it is necessary to express the plane waves using the basis of s- and p-polarization as defined in Eq. 2.16. Utilizing this, one can rewrite Eq. 2.35 as

$$\overset{\leftrightarrow}{\mathbb{G}}(\vec{r},\vec{r}_0,\omega) = -\frac{\hat{z}\hat{z}}{k^2}\delta(\vec{r} - \vec{r}_0) + \frac{\mathrm{i}}{8\pi^2}\int\int \mathrm{d}k_x\,\mathrm{d}k_y \frac{\hat{s} \otimes \hat{s} + \hat{p} \otimes \hat{p}}{k_z}\mathrm{e}^{\mathrm{i}\vec{k}\cdot(\vec{r}-\vec{r}_0)}\,. \tag{2.36}$$

A convenient method to calculate the Green's tensor of a multilayer system is the transfer matrix method (TMM) [21, 22]. TMM is an exact solution of Maxwell's equations as long as the interfaces are planar and a coherent wave-optical treatment is valid. The full Green's

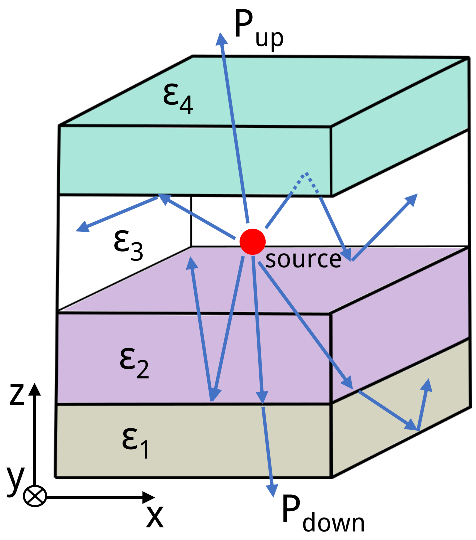

Figure 2.2: Multilayer stack, as we will consider it several times throughout this thesis. When computing the Green's tensor of the optical system at the position of the source, one has to account for all possible reflections at the interfaces. In this example, a source (for example an electric dipole) is located in one of the planar layers and emits radiation. The layers have permittivities ε_1, ε_2, ε_3, and ε_4. P_{up} and $\mathrm{P}_{\mathrm{down}}$ denote the power that is coupled out of the multilayer in positive and negative z-direction, respectively.

tensor is then composed by adding the Green's tensor for the homogenous case and the Green's tensor due to the presence of the interfaces.

For more complicated media, such as the ones analyzed in this work with textured interfaces between different layers, the Green's tensor has to be determined numerically. This is for example done by discretizing the considered domain and solving Maxwell's equations in each of the resulting small volumes. The continuity conditions between the small volumes are afterwards used to fix remaining free parameters. This is essentially the idea of the Finite Element Method, which will be described in Sec. 2.8.

2.2.2 Local Density of States, Decay Rate, and Purcell Factor

In the following, the Green's tensor will be, without assuming a specific geometry, exploited to derive near-field quantities that are relevant for the thesis. First, the electric field is the particular solution with a localized, but otherwise arbitrary current distribution [23],

$$\vec{E}(\vec{r},\omega) = \mathrm{i}\omega\mu(\omega)\int \overleftrightarrow{\mathbb{G}}(\vec{r},\vec{r}\,',\omega)\cdot\vec{j}(\vec{r}\,',\omega)\;\mathrm{d}V'\,. \tag{2.37}$$

The current density resulting from an electric dipole $\vec{p}$ at point $\vec{r}_0$ is given by [23]

$$\vec{j}(r,\omega) = -\mathrm{i}\omega\vec{p}\,\delta(\vec{r}-\vec{r}_0)\,, \tag{2.38}$$

so that it follows

$$\vec{E}(\vec{r},\omega) = \omega^2\mu(\omega)\overleftrightarrow{\mathbb{G}}(\vec{r},\vec{r}_0,\omega)\cdot\vec{p}\,. \tag{2.39}$$

The rate of energy dissipation of a current distribution can be expressed, using Poyntings theorem (Eq. 2.15), as [23]

$$P = \frac{dW}{dt} = -\frac{1}{2}\int \Re\left\{\vec{j}^{\,*}(\vec{r},\omega)\cdot\vec{E}(\vec{r},\omega)\right\}\mathrm{d}V\,. \tag{2.40}$$

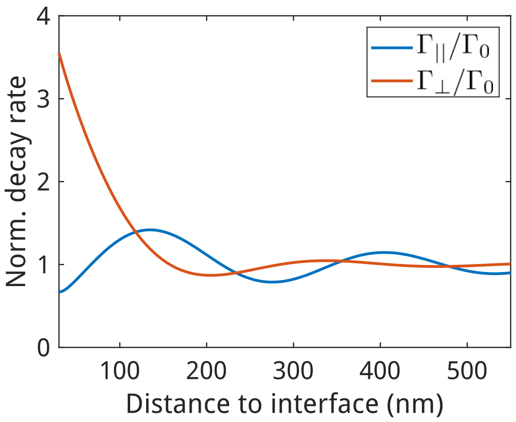

Figure 2.3: Normalized decay rates of an emitter for varying distance to a planar silver interface. The emission wavelength is 500 nm, and we plot the parallel and perpendicular decay rate normalized to the decay rate in the vacuum case. While the decay rates converge to the free-space case for distances larger than the wavelength, for smaller distances the decay rates oscillate and the perpendicular decay rate strongly increases.

Inserting Eqs. 2.38 and 2.39 into Eq. 2.40, we obtain at a fixed emission frequency $\omega = \omega_0$ [23]

$$P = \frac{dW}{dt} = \frac{|\vec{p}|^2\omega_0^3}{2c^2\varepsilon(\omega_0)} \left[\hat{e}_{\vec{p}} \cdot \Im\left\{\overleftrightarrow{\mathbb{G}}(\vec{r}_0, \vec{r}_0, \omega_0)\right\} \cdot \hat{e}_{\vec{p}}\right] . \tag{2.41}$$

The rate of dissipated energy is proportional to the decay rate of an emitter. It holds [23]

$$\frac{\Gamma}{\Gamma_0} = \frac{P}{P_0}, \tag{2.42}$$

where Γ_0 and P_0 are normalization factors obtained from a reference system, e. g. free space. One can derive an expression for the decay rate in a quantum mechanical treatment starting from Fermi's golden rule [23]. This yields

$$\Gamma(\vec{r}_0, \omega_0) = \frac{\pi\omega_0}{3\hbar\varepsilon_0}|\vec{p}|^2\rho(\vec{r}_0, \omega_0) \tag{2.43}$$

with the local density of states (LDOS) as [23]

$$\rho(\vec{r}_0, \omega_0) = \frac{6\omega_0}{\pi c^2} \left[\hat{e}_{\vec{p}} \cdot \Im\left\{\overleftrightarrow{\mathbb{G}}(\vec{r}_0, \vec{r}_0, \omega_0)\right\} \cdot \hat{e}_{\vec{p}}\right] . \tag{2.44}$$

The LDOS is a measure how many radiation channels are available at a given point in space and also how probable an emitter is to emit photons into those modes. Physically, more modes to which an emitter can couple result in faster extraction of power from the emitter and thus a shorter emitter lifetime, which is defined via

$$\tau = \frac{1}{\Gamma}. \tag{2.45}$$

For example, the decay rate in free space at a fixed frequency ω_0 is [23]

$$\Gamma_0(\omega_0) = \frac{|\vec{p}|^2\omega_0^3}{3\pi\hbar c^3\varepsilon_0}. \tag{2.46}$$

The local density of states and therefore also the decay rate depend heavily on the optical environment. This was first appreciated by Purcell [24]. Therefore, one is often not interested in absolute values of the emitter lifetime, but only in the change relative to the lifetime τ_0 compared to a homogeneous optical environment. The normalized value

$$F_\mathrm{P} = \frac{\Gamma}{\Gamma_0} = \frac{\tau_0}{\tau} \tag{2.47}$$

is known as Purcell factor. To calculate the Purcell factor in an optical environment, the electric field can be separated into the part $\vec{E}_0$, corresponding to the electric field for an homogeneous background, and a part $\vec{E}_\mathrm{sca}(\vec{r})$ arising from scattering at the photonic environment. For the latter part, the full optical response of the system is required. For the normalized decay rate, one then obtains [23]

$$\frac{\Gamma}{\Gamma_0} = 1 + \frac{6\pi\varepsilon(\omega)}{|\vec{p}|^2}\frac{1}{k^3}\Im\{\vec{p}^* \cdot \vec{E}_\mathrm{sca}(\vec{r}_0)\}\,. \tag{2.48}$$

We show the spatial dependence of the decay rate for the simple case of one planar interface separating two homogeneous semi-infinite halfspaces. For such geometry, one additional term for each field polarization has to be added to the homogeneous Green's tensor, Eq. 2.36, since plane waves are reflected either zero times or once at the interface before propagating towards infinity. The coordinate system is chosen so that the interface is located at $z_I = 0$ in the x-y-plane. For the decay rate of an emitter polarized parallel to the interface, one obtains [25]

$$\begin{aligned}\frac{\Gamma_{||}(d)}{\Gamma_0} =& \frac{6\pi}{k}\Im\Bigg\{\hat{e}_x \cdot \frac{\mathrm{i}}{8\pi^2}\int \mathrm{d}k_x\,\mathrm{d}k_y \frac{1}{k_z}\Big[\hat{s}\otimes\hat{s} + \hat{p}\otimes\hat{p} \\ &+ \left(r_\mathrm{s}\,\hat{s}\otimes\hat{s} + r_\mathrm{p}\,\hat{p}\otimes\hat{p}\right)\mathrm{e}^{2\mathrm{i}k_z d}\Big]\cdot\hat{e}_x\Bigg\}\,,\end{aligned} \tag{2.49}$$

where the first term results from the homogeneous Green's tensor and the second term accounts for all the reflected plane waves. Note that $k_z = \sqrt{k^2 - k_{||}^2}$ with $k_{||} = \sqrt{k_x^2 + k_y^2}$ depends on both k_x and k_y and therefore needs to be considered for the integration. The expression for the decay rate of an emitter polarized perpendicular to the interface can be found in Ref. [25].

Experimentally, such spatial dependency of the decay rate was first demonstrated by Drexhage [26]. He showed that a mirror placed in spatial proximity of an emitter changes the LDOS and leads to oscillations of the decay rate for varying distance of the emitter to the mirror. This is illustrated in Fig. 2.3, where the perpendicular and parallel decay rates are plotted, normalized to the vacuum case. We use a dipole emitter at a wavelength of 500 nm above a planar silver interface ($n_\mathrm{Ag} = 0.05 + 3.093\mathrm{i}$ [27]) in the x-y-plane. The half space for $z > 0$, where the dipole is located, shall be vacuum.

From Fig. 2.3, it is also apparent that the decay rate depends on the orientation of the emitter relative to the interface: For a perpendicular oriented dipole (i. e. polarized in z-direction), the decay rate $\Gamma_\perp$ is significantly larger than the decay rate of a parallel oriented dipole, $\Gamma_{||}$, for distances up to around 100 nm. This is due to the fact that radiation of the perpendicular oriented emitter can couple easier to surface modes. For larger distances, both decay rates oscillate with decreasing amplitude and converge to the free space value. Since the oscillations are due to the interference between the light travelling towards the mirror and the light that was already reflected, the oscillations are more pronounced for the longitudinal emitter [23]. For arbitrary textured interfaces, the decay rate not only depends on the emitter distance and the orientation to the interface, but also on the lateral position.

The presence of e. g. near-field enhancements due to sharp geometrical features, surface resonances, or guided modes can also significantly in- or decrease the radiative lifetime of an emitter. This will be exploited in the thesis, where the emitters will be placed in the vicinity of tailored nanostructures to achieve enhanced and directional emission, respectively, due to coupling to leaky guided modes.

To gain insights into an optical system, often one does not need the full information about the electromagnetic field, but only the far-field distribution. Having this in mind, the next section explicitly deals with diffraction and the angular representation of far-fields.

2.3 Diffraction Theory and Gratings

A main feature of this thesis is the design of periodic or rough interfaces to provide an optimal scattering response in specific wavelength regimes. The following section introduces some important concepts how such situations can be studied theoretically. For this purpose, the angular spectrum representation of far-fields and the description of the diffraction from gratings are discussed in devoted subsections. Furthermore, we will introduce the important Bloch theorem and show how this theorem can be utilized to obtain the emission pattern of a single dipole from periodically arranged dipoles.

2.3.1 Angular Spectrum Representation

A very useful tool in diffraction theory is the angular spectrum representation. The angular spectrum is the Fourier expansion of an arbitrary electric (or magnetic) field in terms of propagating and evanescent plane waves in a given referential plane [28]. Assume that a field $\vec{E}(x, y, z)$ emanates from an object, either by an intrinsic emitter or after being scattered, and propagates in positive z-direction. Then, at an arbitrary z-position, the angular spectrum of the field is given by the two-dimensional Fourier transform [23, 29]

$$\tilde{\vec{E}}(k_x, k_y; z) = \frac{1}{(2\pi)^2} \int_{-\infty}^{\infty} \int_{-\infty}^{\infty} \vec{E}(x, y, z)\, \mathrm{e}^{-\mathrm{i}k_x x}\, \mathrm{e}^{-\mathrm{i}k_y y}\, \mathrm{d}x\, \mathrm{d}y\,. \tag{2.50}$$

Conversely, the field in real space is

$$\vec{E}(x, y, z) = \int_{-\infty}^{\infty} \int_{-\infty}^{\infty} \tilde{\vec{E}}(k_x, k_y, z)\, \mathrm{e}^{\mathrm{i}k_x x}\, \mathrm{e}^{\mathrm{i}k_y y}\, \mathrm{d}k_x\, \mathrm{d}k_y\,. \tag{2.51}$$

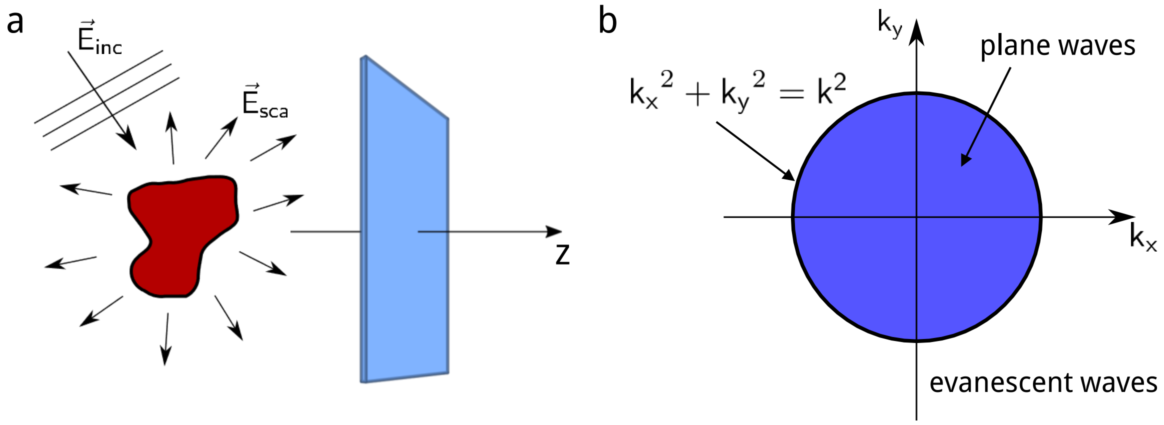

Figure 2.4: a) The angular spectrum of the scattered field is measured at an arbitrary but fixed z-position (indicated by the blue plane). b) For the far-field, only the propagating field components are relevant. Both images are adapted from Ref. [23].

Assuming a non-lossy and isotropic medium in which the field propagates, the field that emanates from an object at $z = 0$ only differs by a phase factor from the field after propagation to an arbitrary z. This can be shown with the homogeneous Helmholtz equation (Eq. 2.10 with zero on the right side): The electric field has to fulfill [23]

$$\begin{aligned} 0 &= (\vec{\nabla}^2 + k^2)\vec{E}(\vec{r}) \\ &= (\vec{\nabla}^2 + k^2)\int_{-\infty}^{\infty}\int_{-\infty}^{\infty} \tilde{\vec{E}}(k_x, k_y, z)\, \mathrm{e}^{ik_x x}\, \mathrm{e}^{ik_y y}\, \mathrm{d}k_x\, \mathrm{d}k_y \\ &= \int_{-\infty}^{\infty}\int_{-\infty}^{\infty} \left(\frac{\partial^2}{\partial z^2} + k_z^2\right) \tilde{\vec{E}}(k_x, k_y, z)\, \mathrm{e}^{ik_x x}\, \mathrm{e}^{ik_y y}\, \mathrm{d}k_x\, \mathrm{d}k_y\,. \end{aligned} \tag{2.52}$$

Here, the z-component of the wavevector can not be chosen arbitrarily, but is fixed via the relation

$$k_z = \sqrt{k^2(\omega) - k_x^2 - k_y^2}\,. \tag{2.53}$$

k_z can be either real or imaginary. We will use here the convention that the imaginary part of k_z is positive. The entire expression 2.52 is zero if the integrand is zero. Therefore, to avoid exponential growth of a wave that propagates per assumption in positive z-direction, the only physical relevant solution of the differential equation

$$\left(\frac{\partial^2}{\partial z^2} + k_z^2\right) \tilde{\vec{E}}(k_x, k_y, z) = 0 \tag{2.54}$$

is

$$\tilde{\vec{E}}(k_x, k_y; z) = \tilde{\vec{E}}(k_x, k_y; 0)\, \mathrm{e}^{ik_z z}\,. \tag{2.55}$$

This means that the field at any distance z can be obtained from the field at $z = 0$ via

$$\vec{E}(x, y, z) = \int_{-\infty}^{\infty}\int_{-\infty}^{\infty} \tilde{\vec{E}}(k_x, k_y; 0)\, \mathrm{e}^{ik_x x}\, \mathrm{e}^{ik_y y}\, \mathrm{e}^{ik_z z}\, \mathrm{d}k_x\, \mathrm{d}k_y\,. \tag{2.56}$$

Relevant for this thesis is the fact that the far-field intensity can be expressed with coefficients $\tilde{\vec{E}}(k_x, k_y; 0)$ that only depend on the in-plane wavevector components, since the exponential phase factor cancels out when the intensity is calculated. The integration in Eq. 2.56 runs over the whole in-plane k-space, but from Eq. 2.53 we can deduce that there is a maximum radius in k-space of allowed wavevectors (see Fig. 2.4b), which is given by $k_{||} = |\vec{k}|$. Field components inside this circle contribute to the far-field intensity, while components outside are evanescent and can be neglected in the far-field (for $z \to \infty$ they are strictly zero).

To calculate the power for a given k_x-k_y combination inside the propagation cone, one projects the field intensity onto the angle relative to the z-axis,

$$P(k_x, k_y) = \frac{n}{2}\sqrt{\frac{\varepsilon_0}{\mu_0}} \left|\tilde{\vec{E}}(k_x, k_y; 0)\right|^2 \cos\theta \,. \tag{2.57}$$

where θ is determined via $\cos\theta = \Re\left\{\frac{k_z}{k}\right\}$ and n is the refractive index in the spatial region where the far-field is considered.

Often, one is not interested in the total scattered power, but only in the power that is diffracted into a certain angular region. To account for this, there exist additional figures of merit. An important quantity for identifying rough surfaces with weak specular reflection is the haze [30]. It is given by the fraction of the power scattered in non-specular direction to the total scattered power:

$$\mathscr{H} = \frac{\sum_{k_x,k_y} P(k_x, k_y) - P(k_x = 0, k_y = 0)}{\sum_{k_x,k_y} P(k_x, k_y)} \,. \tag{2.58}$$

However, the haze does not allow to distinguish rough surfaces with respect to their non-specular scattering properties. We will therefore use in Sec. 3.3 an adapted figure of merit that takes into account that the scattering to non-specular angles is not equally useful.

2.3.2 Gratings

In this subsection, we will briefly explain the scattering properties of gratings and derive the grating equation. Using gratings to couple light into waveguides will be discussed in Sec. 2.4.2.

We will now consider a one-dimensional binary grating lying in the x-y-plane that is illuminated from the positive z-axis, as depicted in Fig. 2.5a. The grating period shall be p. The inverse lattice vector is then $G = \frac{2\pi}{p}$. The medium above the grating shall have permittivity ε_1, the medium below the grating shall have permittivity ε_2. We denote with λ_1 the wavelength in medium 1 and with λ_2 the wavelength in medium 2.

If the interface between the two media was planar, there would be, according to Snell's law of refraction (Eq. 2.24), for an incident angle θ_{inc} only one reflection angle. The situation is different for a textured interface. With gratings, the scattering directionality can be controlled, at least for discrete wavelengths and incident angles.

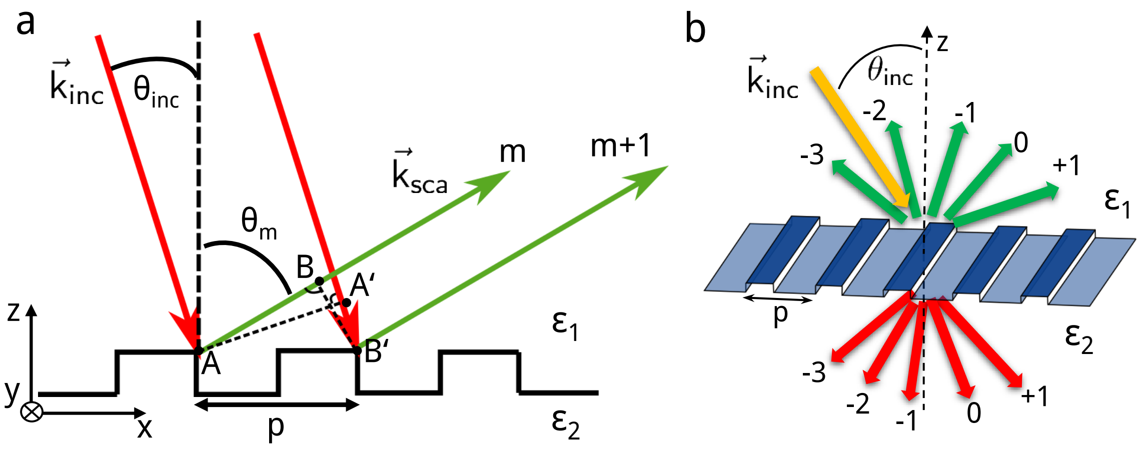

Figure 2.5: a) Sketch for the derivation of the grating equation. The incoming light is scattered at the grating at points A and B'. To enable constructive interference, only discrete scattering angles θ_m are allowed. b) Diffraction orders of a binary lamellar grating between two media with permittivites ε_1 and ε_2.

To derive an equation that connects the angle and wavelength of the indicent light with the grating period and the possible scattering angles, we look at Fig. 2.5a that illustrates a reflection process. When the left ray hits the interface at point A, the right ray is assumed to be at point A'. The reflection introduces a phase difference between the two rays due to different path lengths. We compare the two rays after reflection at the points B and B'. The distances d_{AB} and $d_{\mathrm{A'B'}}$ are given by

$$d_{\mathrm{AB}} = p \sin \theta_{\mathrm{m}} \tag{2.59}$$

$$d_{\mathrm{A'B'}} = p \sin \theta_{\mathrm{inc}} \,. \tag{2.60}$$

In the ray-optical picture, to obtain a diffraction order at an angle θ_m, constructive interference has to happen between the two scattered rays. In this case, the difference between the paths d_{AB} and $d_{\mathrm{A'B'}}$ has to be an integer multiple of the wavelength, $d_{\mathrm{AB}} = d_{\mathrm{A'B'}} + m\lambda_1$ with $m \in \mathbb{Z}$. Combining the three equations, we find

$$p \sin \theta_m = p \sin \theta_{\mathrm{inc}} + m\lambda_1 \,. \tag{2.61}$$

This is the grating equation that determines the possible reflected diffraction orders m for given angle of incidence, wavelength and grating period [31]. Figure 2.5b shows schematically a few of the lowest diffraction orders of a binary grating.

The grating equation can also be derived when considering the momentum of the photons impinging on the grating. To scatter a photon in a non-specular direction, a momentum parallel to the interface has to be imparted onto the photon. An incoming photon with wavelength λ_1 and wavenumber k has a momentum component $k_{1,||} = k_1 \sin \theta_{\mathrm{inc}}$ parallel to the grating interface. The reciprocal lattice vector G can transfer an additional momentum mG onto the photon, which will change the scattering angle according to

$$k_1 \sin \theta_m = k_1 \sin \theta_{\mathrm{inc}} + mG \,. \tag{2.62}$$

Multiplying with p/k_1 recovers the grating equation 2.61 as derived in the ray-optical picture. This momentum picture will be important in Sec. 3.2 when we optimize the back-reflector textures of solar cells.

2.3.3 Bloch Theorem and Inverse Floquet Method

An important theorem for periodic structures is the Bloch theorem, also called Bloch-Floquet theorem. It states that in the presence of a periodic potential $V(\vec{r}+\vec{R}) = V(\vec{r})$ with lattice vector $\vec{R}$, the wavefunctions are pseudo-periodic [32]:

$$\psi(\vec{k},\vec{r}) = u(\vec{r})\,\mathrm{e}^{\mathrm{i}\vec{k}\cdot\vec{r}}\,, \tag{2.63}$$

with $u(\vec{r}+\vec{R}) = u(\vec{r})$. Equation 2.63 expresses the fact that any wavefunction, while resembling a plane wave, is modulated with a function that contains the periodicity of the periodically structured environment.

We will consider now two-dimensional gratings with in general two different periods p_x and p_y, implying different reciprocal lattice vectors $G_x = \frac{2\pi}{p_x}$ and $G_y = \frac{2\pi}{p_y}$. An important property of Bloch states is that they are invariant upon shifting them by an integer multiple (m, q) along the reciprocal lattice periodicity. This is expressed by

$$\psi(\vec{k},\vec{r}) = \psi(\vec{k} + mG_x\hat{e}_x + qG_y\hat{e}_y, \vec{r})\,, \tag{2.64}$$

which means that identical wavefunctions exist for wavevectors that are separated by one reciprocal lattice vector. From this, we obtain that the phase factor has to fulfill the equation

$$\mathrm{e}^{\mathrm{i}\vec{k}\cdot\vec{r}} = \mathrm{e}^{\mathrm{i}(\vec{k}+mG_x\hat{e}_x+qG_y\hat{e}_y)\cdot\vec{r}}\,. \tag{2.65}$$

Therefore, it is sufficient to consider only wavevectors in the reciprocal unit cell, also called Brillouin zone, for the analysis of the modes.

In Ch. 4, we will consider electric and magnetic dipole emitters in periodic photonic environments where the Floquet-Bloch theorem is applicable. Calculating the field of an isolated dipole in a periodic environment requires to consider a large amount of unit cells to avoid truncation errors when the dipole radiation has a rather long decay length. Such large simulation domain is usually not feasible. Therefore, there is the desire to limit the computation to just one unit cell of the structure. However, just carrying out the simulation on a computational domain equal to the unit cell and with periodic boundaries would yield the field of a periodic dipole. Yet, by exploiting the Floquet boundary conditions of the periodic background and modifying the source term accordingly, calculating the dipole response within one unit cell is sufficient; this comes with the expense to repeat the simulation of the unit cell many times, each iteration with a different Bloch vector [33].

Using Eq. 2.63, a current density is Bloch periodic if it fulfills

$$\mathrm{e}^{\mathrm{i}\vec{k}\cdot\vec{R}}\vec{j}(\vec{r}) = \vec{j}(\vec{r}+\vec{R})\,, \tag{2.66}$$

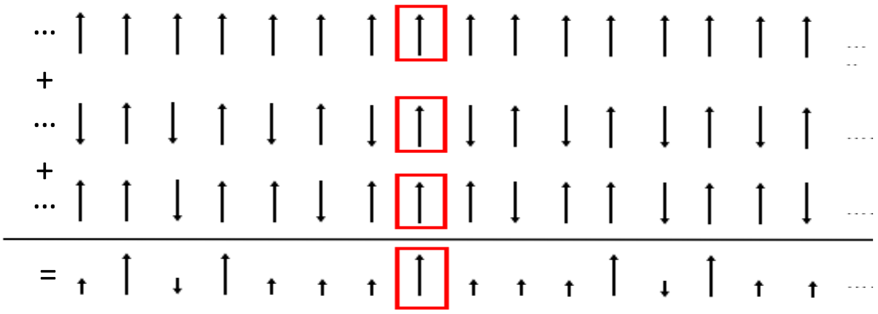

Figure 2.6: Schematic and simplified sketch of the idea of the inverse Floquet method, comprising only two different orientations of a dipole. By adding more terms with modulated phases, the central dipole that shall be simulated gets amplified, while the neighboring dipoles diminish.

and the physically measureable current density is obtained by taking the real part of Eq. 2.66. In this case, the resulting electric and magnetic fields will also be Bloch-periodic [33]. To express the source term of a single electric dipole with Bloch-periodic electric dipoles, one uses that an arbitrary localized current density $\vec{j}(\vec{r})$ can be expressed with an integral over the reciprocal unit cell U_k as [34]

$$\vec{j}(\vec{r}) = \int_{U_k} \tilde{j}(\vec{r},\vec{k})\, \mathrm{e}^{\mathrm{i}\vec{k}\cdot\vec{r}}\, \mathrm{d}\vec{k}\,, \tag{2.67}$$

with $\tilde{j}(\vec{r},\vec{k})$ given by

$$\tilde{j}(\vec{r},\vec{k}) = \frac{U}{(2\pi)^2}\mathrm{e}^{-\mathrm{i}\vec{k}\cdot\vec{r}} \sum_{\vec{\tau}\in Z^2} \mathrm{e}^{-\mathrm{i}\vec{k}\cdot(\hat{A}\cdot\vec{\tau})}\vec{j}(\vec{r}+\hat{A}\cdot\vec{\tau})\,, \tag{2.68}$$

and $\hat{A}$ contains the lattice vectors,

$$\hat{A} = \begin{pmatrix} p_x & 0 \\ 0 & p_y \end{pmatrix}. \tag{2.69}$$

This shows that one can vary the phase attributed to the current density (Eq. 2.66) and obtain via the inverse Floquet transform (Eq. 2.67) a resulting arbitrary current density. In Eq. 2.68, the sum runs over all integers, i. e. over the whole (infinite) lattice. When applying the inverse Floquet method to specific problems, one has to limit the sum to a finite number of terms, i. e. the sampling of the Brillouin zone will be discrete. The required number of terms typically depends on the size of the period compared to the wavelength: The larger the period compared to the wavelength, the more terms are needed to achieve a desired accuracy of the resulting source term. This is schematically illustrated for a dipole along one dimension in Fig. 2.6. Note that the sketch is for only two phase terms for simplicity.

In the next section, waveguides and the important concept of grating couplers will be introduced.

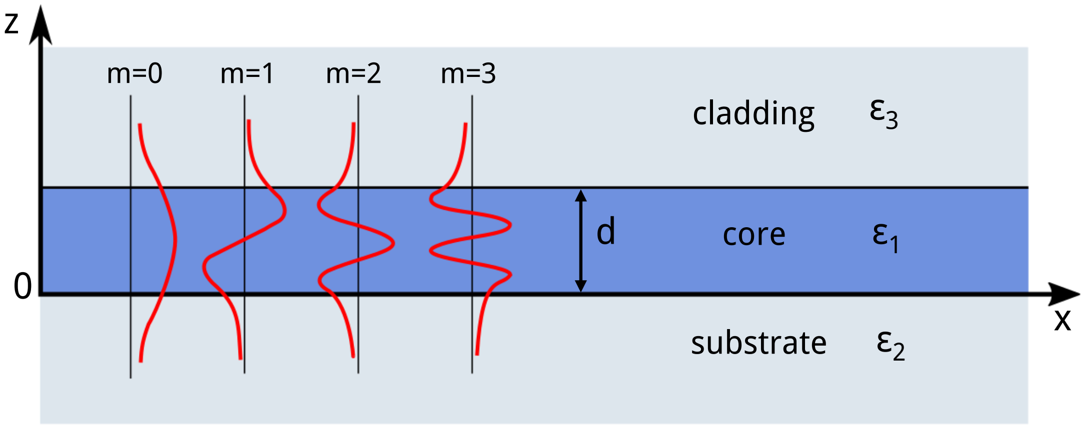

Figure 2.7: Planar waveguide consisting of a core material with permittivity ε_1, substrate with permittivity ε_2, and cladding with permittivity ε_3. To sustain modes in the core layer, it has to hold $\varepsilon_1 > \varepsilon_2, \varepsilon_3$. The thickness d of the core layer determines the number of the possible eigenmodes. The lowest four transverse-electric (TE) modes are shown in red. Adapted from Ref. [35].

2.4 Waveguide Theory

In this section, we will introduce the concept of waveguides and unfold the derivation of eigenmodes in planar dielectric waveguides. Furthermore, we will show how a grating can be used to couple light in and out of waveguides. Guided modes are relevant both for solar cells and LEDs; in the former, one aims to couple incoming light to them to enhance the absorption, while in the latter, they are typically avoided to not impair the photoluminescence yield of the device.

2.4.1 Eigenmodes in Multilayer Waveguides

A planar waveguide is a layered system that consists of a guiding material with permittivity ε_1, surrounded at the top and bottom with materials that have permittivities $\varepsilon_2, \varepsilon_3 < \varepsilon_1$. In the special case of a planar dielectric waveguide, all materials are dielectric. The top and bottom material can be different or the same material. An example three-layer waveguide system is shown in Fig. 2.7.

In the guiding layer, eigenmodes can be sustained. In general, a mode is a specific field pattern that can propagate without changing its shape and, in the absence of absorption, without fading away, along a waveguide. There are two different kinds of modes: For TE modes, the non-zero field components are E_y, H_x, and H_z. On the other hand, for TM modes, only the field components E_x, E_z, and H_y are non-zero [35]. The amplitudes of the lowest four TE modes are shown in Fig. 2.7.

Like in the previous chapter, we will first present a geometrical ray-optical approach to derive the propagation constant of the available modes, and afterwards, we will sketch the rigorous derivation. In Fig. 2.8, two propagating waves are shown in a guiding layer with

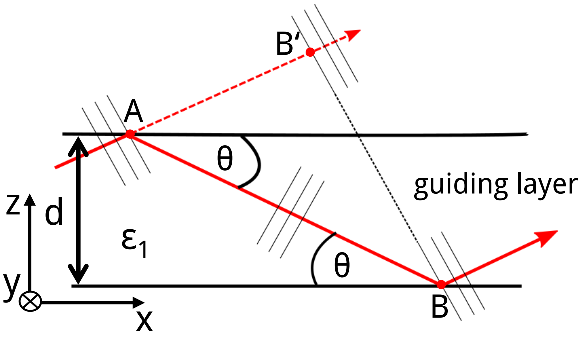

Figure 2.8: Ray-optical derivation of possible waveguide modes. One ray is travelling from A to B', whereas the other ray is travelling from A to B. For a resulting propagating wave, both rays have to constructively interfere. This yields a condition for possible modes.

thickness d. One of the waves is assumed to propagate without reflection at the interface from A to B', while the other is reflected twice and propagates from A to B. After these two reflections, this wave has a delay compared to the unreflected wave, which is given by

$$d_{\mathrm{AB}'} - d_{\mathrm{AB}} = 2d \sin\theta \,, \tag{2.70}$$

where θ is the angle of the two light rays measured relative to the x-axis. Furthermore, each reflection at the boundary between the core and the cladding entails an additional phase ϕ_r. A mode can only exist if the light rays interfere constructively, i. e. we demand

$$d_{\mathrm{AB}'} = d_{\mathrm{AB}} + m\lambda \tag{2.71}$$

with m being an integer. Given this, we obtain [35]

$$2d \sin\theta - \lambda/\pi\phi_r = m\lambda \,. \tag{2.72}$$

The propagation constant β_m of mode m propagating along the x-axis is [35]

$$\beta_m = n_1 k_0 \cos\theta_m \,, \tag{2.73}$$

with the angles determined by Eq. 2.72. This means that the effective refractive index

$$n_{\mathrm{eff}} = n_1 \cos\theta_m \tag{2.74}$$

is upper-bounded by the refractive index of the guiding layer. There is also a lower bound, which is given by the refractive index of the substrate (assuming that the substrate has the larger refractive index as the cladding).

To rigorously derive the modes in the waveguide, we start from Maxwell's equations in frequency space, Eqs. 2.6–2.9. Assuming the coordinate system of Fig. 2.7, the problem is translationally invariant along the y-axis, which directly implies $\frac{\partial \vec{E}}{\partial y} = \frac{\partial \vec{H}}{\partial y} = 0$. The remaining equations, hereby suppressing the dependencies of the fields, to solve are then

$$\begin{aligned}
\frac{\partial}{\partial z}E_y &= -\mathrm{i}\omega\mu_0 H_x\,,\\
\frac{\partial}{\partial z}E_x - \frac{\partial}{\partial x}E_z &= \mathrm{i}\omega\mu_0 H_y\,,\\
\frac{\partial}{\partial x}E_y &= \mathrm{i}\omega\mu_0 H_z\,,
\end{aligned} \tag{2.75}$$

and

$$\begin{aligned}
\frac{\partial}{\partial z}H_y &= \mathrm{i}\omega\varepsilon(x)E_x\,,\\
\frac{\partial}{\partial z}H_x - \frac{\partial}{\partial x}H_z &= -\mathrm{i}\omega\varepsilon(x)E_y\,,\\
\frac{\partial}{\partial x}H_y &= -\mathrm{i}\omega\varepsilon(x)E_z\,.
\end{aligned} \tag{2.76}$$

We now assume that the field is propagating along the x-axis. In such a geometry, eigenmodes can be written in the form

$$\begin{aligned}
\vec{E}(x,z) &= \vec{\mathscr{E}}^m(z)\,\mathrm{e}^{\mathrm{i}\beta_m x}\,,\\
\vec{H}(x,z) &= \vec{\mathscr{H}}^m(z)\,\mathrm{e}^{\mathrm{i}\beta_m x}\,.
\end{aligned} \tag{2.77}$$

β_m is the propagation constant along x. Combining Eqs. 2.75–2.76 and inserting the ansatz Eq. 2.77, we obtain

$$\left[\frac{\partial^2}{\partial z^2} + k^2\varepsilon(z)\right]\mathscr{E}_y^m(z) = \beta_m^2\mathscr{E}_y^m(z)\,, \tag{2.78}$$

$$\left[\varepsilon(z)\frac{\partial}{\partial z}\left(\frac{1}{\varepsilon(z)}\frac{\partial}{\partial z}\right) + k^2\varepsilon(z)\right]\mathscr{H}_y^m(z) = \beta_m^2\mathscr{H}_y^m(z)\,. \tag{2.79}$$

This is now an eigenvalue problem, where β_m^2 is the eigenvalue and $\mathscr{E}_y^m$ as well as $\mathscr{H}_y^m$ are the eigenfunctions of mode m. The first equation describes TE modes, the second equation TM modes. One can further simplify the problem by taking into account that the structure consists of discrete layers; then, $\varepsilon(z) = \varepsilon = \text{const.}$ within each layer and Eq. 2.79 reduces to Eq. 2.78.

Using the notation that $\phi^m(z)$ may either be $\mathscr{H}_y^m(z)$ or $\mathscr{E}_y^m(z)$, the solutions of

$$\left[\frac{\partial^2}{\partial z^2} + k^2\varepsilon\right]\phi^m(z) = \beta_m^2\phi^m(z) \tag{2.80}$$

in the guiding layer are oscillating functions whereas in the cladding and substrate, they have to decay for $z \to \pm\infty$. Furthermore, we can separate the solution of the modes that are

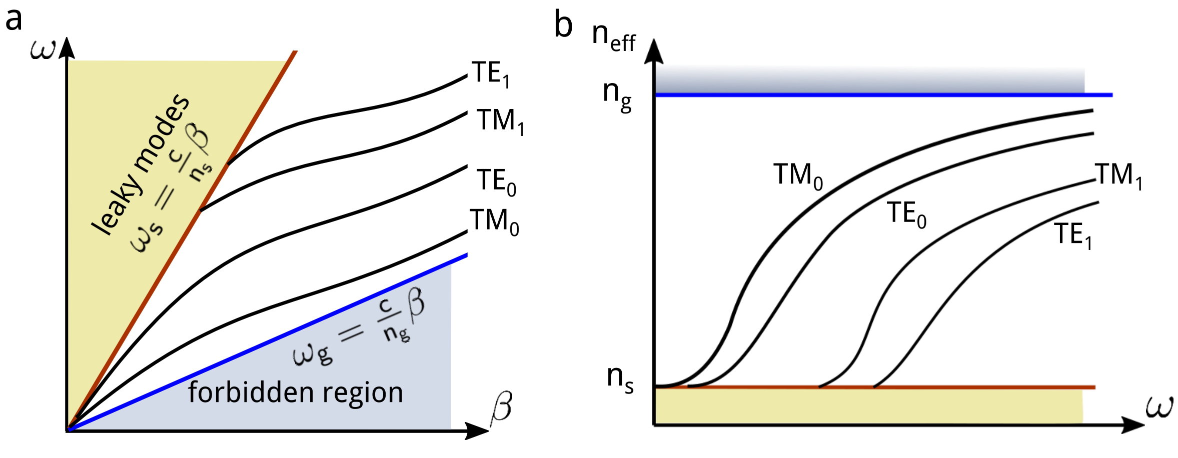

Figure 2.9: a) Schematic dispersion relations inside the guiding layer, plotted over the propagation constant β. With increasing angular frequeny ω, more modes emerge and approach the dispersion relation of a homogeneous medium with a refractive index $\mathrm{n_g}$ of the guiding layer. Adapted from Ref. [36]. b) Plot of the effective refractive index $\mathrm{n_{eff}}$ over the angular frequency. This plot can be obtained by inverting the dispersion relations plotted in a) and expressing the propagation constant β with $\mathrm{n_{eff}}$. The values of $\mathrm{n_{eff}}$ are bounded by the refractive indices of the substrate $\mathrm{n_s}$ (assuming the substrate index to be larger than the cladding index) and the guiding layer $\mathrm{n_g}$.

even with respect to the z-axis, and those that are odd. For the even modes, we obtain

$$\phi^m(z) = \begin{cases} A_m \mathrm{e}^{\gamma_m(d-z)} & d \le z\,, \\ B_m \cos\beta_m z & 0 \le z \le d\,, \\ C_m \mathrm{e}^{\delta_m z} & z \le 0\,, \end{cases} \tag{2.81}$$

with amplitude coefficients A_m, B_m, and C_m and wavenumbers β_m, γ_m, and δ_m. Here, we are only interested in the possible wavenumbers in the guiding layer, β_m. By invoking the continuity conditions of the tangential and normal components of the electric and magnetic field, one can eliminate the unknown field amplitudes and obtain an implicit equation for the dispersion relations of the possible modes in the guiding layer [35]:

$$\tan^2\left(\frac{d}{2}\sqrt{\frac{\omega^2}{c^2\varepsilon_1} - \beta_m^2} - \frac{\pi m}{2}\right) = \frac{\beta_m^2 - \omega^2/(c^2\varepsilon_2)}{\omega^2/(c^2\varepsilon_1) - \beta_m^2}\,, \tag{2.82}$$

where it was again assumed that the permittivity of the substrate is larger than the permittivity of the cladding. This equation has to be solved graphically or numerically. A resulting schematic dispersion graph for different m that contains TE and TM modes, is shown in Fig. 2.9a. For increasing β_m, more and more modes emerge and approach the straight dispersion line that corresponds to the propagation in a homogeneous medium with refractive index $n_1 = n_\mathrm{g}$.

One can transform the dispersion relation to obtain an equation for the possible effective refractive indices n_eff in the guiding layer. This is shown in Fig. 2.9b: Modes can only exist in the region that is bounded by the refractive index of the guiding layer (blue line) and the

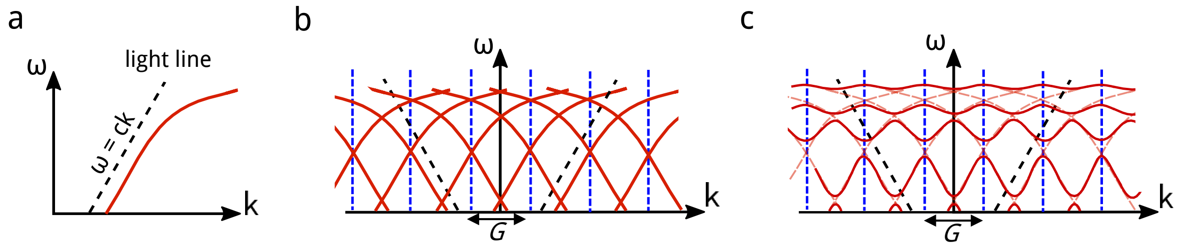

Figure 2.10: Dispersion relation evolution going from a single unit cell to a periodic array in one dimension. a) The dispersion relation of a single mode in a planar waveguide. b) Upon introducing a periodicity with reciprocal lattice vector G, the modes are, according to the Bloch theorem, periodically repeated for wavevectors shifted by an integer multiple of G. Due to the periodicity, it is sufficient to look only at the first Brillouin zone. c) The introduction of a grating will not only lead to a periodic repetition of the dispersion relations, but will also slightly modify them. This results in a split of the dispersions and leads to energy bands. Adapted from Ref. [37].

refractive index of the substrate (assuming that the refractive index of the substrate is larger than that of the cladding), indicated by the red line.

2.4.2 Grating Couplers

The presented analysis has so far assumed that the waveguide is planar. However, for this thesis relevant are textured waveguide multilayers to couple light in or out of the layer stacks into a medium with smaller permittivity, e. g. air. A typical way to achieve this are gratings [38]. In this case, the Bloch theorem (see Sec. 2.3.3) prescribes that the dispersion relations also become periodic according to the underlying symmetry of the lattice.

The change of the dispersion relations for a one-dimensional periodically textured waveguide is illustrated in Fig. 2.10: In (a), a single dispersion relation inside the waveguide is shown, that resembles Fig. 2.9a. Upon introduction of a periodicity, the dispersion relation is periodically repeated along the reciprocal lattice with a period of $\frac{2\pi}{p}$ (see Fig. 2.10b). In a real structure, the periodicity would also affect the dispersion relations itself, especially the intersection of different dispersion relations will not occur. The resulting dispersion relations are called bands. This is depicted in Fig. 2.10c. An example textured waveguide with permittivity ε_2 surrounded by a medium with permittivity ε_1 is shown in Fig. 2.11. For such a structure, light that is incident from the top can couple into the waveguide.

To illustrate the periodicity of the waveguide modes from a different perspective, we now look at a waveguide mode with an effective refractive index n_{eff}. For a two-dimensional grating with period p along x and y, the resulting dispersion relation is

$$\begin{aligned} k_x^m &= n_{\mathrm{eff}}\, k_0 \cos\theta + mG\,, \\ k_y^q &= n_{\mathrm{eff}}\, k_0 \sin\theta + qG\,. \end{aligned} \tag{2.83}$$

For θ continuously varying between 0 and 2π, these equations yield circles; they are shown in Fig. 2.11b. The yellow disk corresponds to the allowed wavevector region in the cladding

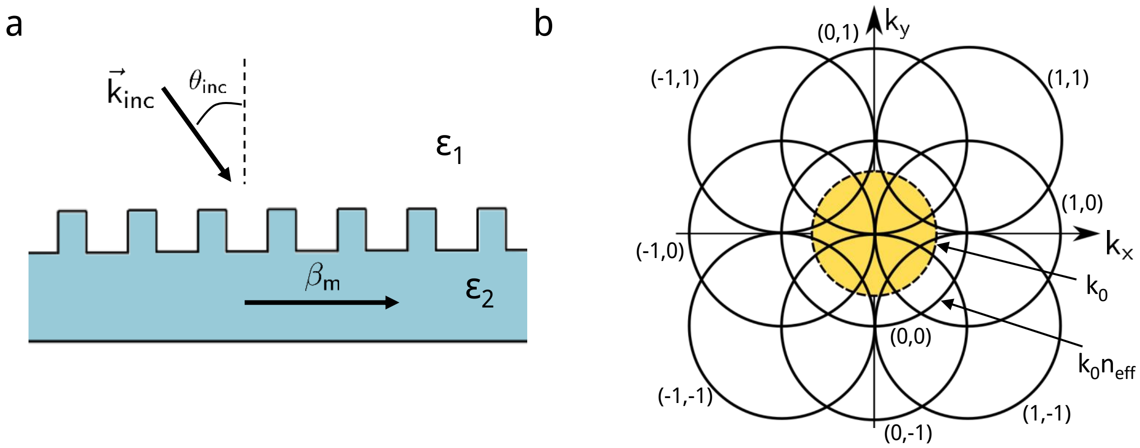

Figure 2.11: a) Waveguide with an inscribed binary grating, so-called grating coupler. Light is incident from the halfspace above the grating to couple into the waveguide. b) Allowed dispersion circles for a mode with effective refractive index n_{eff} inside a waveguide that is textured with a grating with two-dimensional square grating. The yellow region denotes the allowed wavevectors in the cladding region.

layer with permittivity ε_1. For example, if the cladding is vacuum, the radius of the yellow disk would be k_0. The black circles have radius $n_{\mathrm{eff}}k_0$ and are displaced by an integer multiple (m, q) of the reciprocal lattice vector G along k_x and k_y, respectively. The values of m and q that pertain to the different circles are also indicated in Fig. 2.11b.

With sufficient light out-coupling from the waveguide, it is possible to indirectly gain access to the dispersion relations inside the waveguide. This is achieved by looking at the angular spectrum representation of the far-field, as discussed in Sec. 2.3.1. With this, one can obtain a graph that corresponds to the yellow area in Fig. 2.11b. We will use this kind of method repeatedly in Ch. 4 when analyzing emitters in the vicinity of waveguide structures.

2.5 Basics of Solar Cells and Light-Trapping

In this section, we will introduce the basic ideas revolving around solar cells, the important concept of the p-n junction, and the fundamental efficiency limits for solar energy conversion. We will also describe some loss mechanisms and strategies how they can be mitigated by applying photon management strategies.

2.5.1 Working Principle and the p-n Junction

A solar cell is a semiconductor device that converts impinging photons into electron-hole pairs. Both drift into different regions of the semiconductor. Due to this, an electric potential difference builds up inside the cell, which in turn generates a current [39].

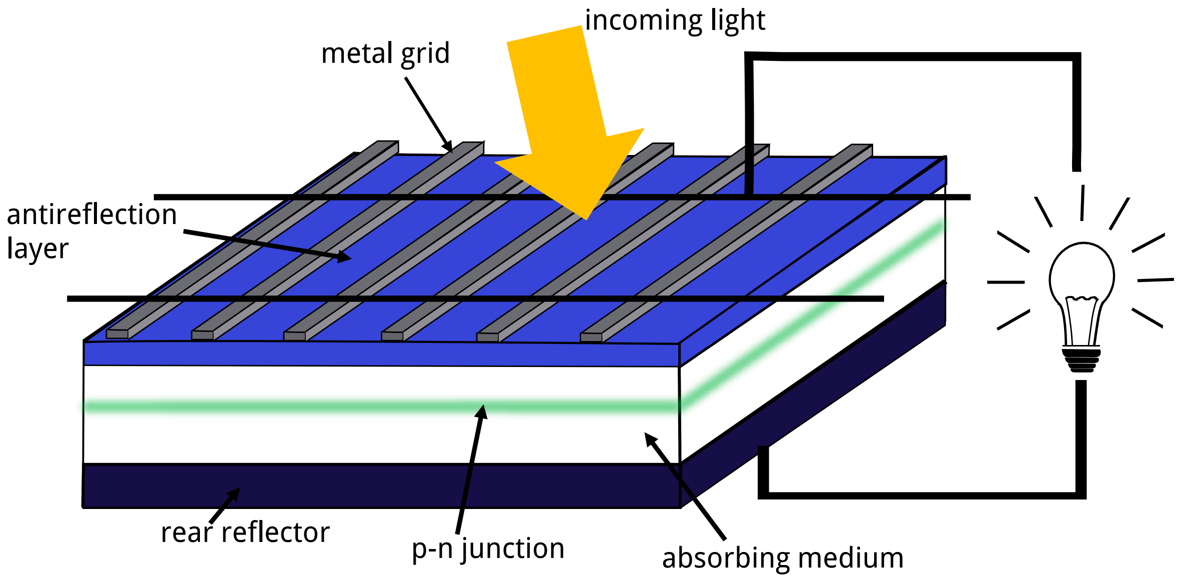

Figure 2.12: Basic geometry of a solar cell. The absorbing medium is sandwiched between the back reflector and the anti-reflection front layer. The absorbing medium features a p-n junction to separate the electron-hole pairs generated from incoming photons. Electrons and holes drift and diffuse to the front and back and are collected at electrode contact fingers. Hereby, a potential difference emerges and an electric current is generated that can be used to power a connected device. Adapted from Ref. [40].

On a very simplified and conceptual level, a solar cell consists from an optical perspective of three functional elements: An absorber medium featuring a p-n junction or a similar charge separation and charge extraction mechanism, an anti-reflective structure or layer on the side that faces the incoming light, and a mirror on the opposite side. A simple three-layer system is depicted in Fig. 2.12. The anti-reflective structure on the front side shall ensure that a large portion of the incident light enters the absorber medium by suppressing reflection. The mirror at the opposite side prevents light outcoupling on the backside. While backreflecting the impinging light, it also increases the light path in the absorbing medium and thereby the probability that the light gets absorbed. The proper engineering of the front and back interfaces is subject of the next subsection. Here, we focus on the discussion of the formation of the internal electric field and the current generation.

One distinguishes intrinsic and extrinsic semiconductors. For intrinsic semiconductors, an electric current will emerge for non-zero temperatures upon external voltage bias due to intrinsic material properties. However, the resulting current is typically very small. For applications, the more important class are extrinsic semiconductors. Here, the charge carrier concentration is increased by adding impurity atoms that either provide electrons or holes to the semiconductor material. For both types of semiconductors, the charges are spatially separated within the semiconductor material, hereby generating domains with net charge accumulation. This leads to the formation of a p-n junction [39].

A schematic cross section of a p-n junction is shown in Fig. 2.13a. The absorber material has

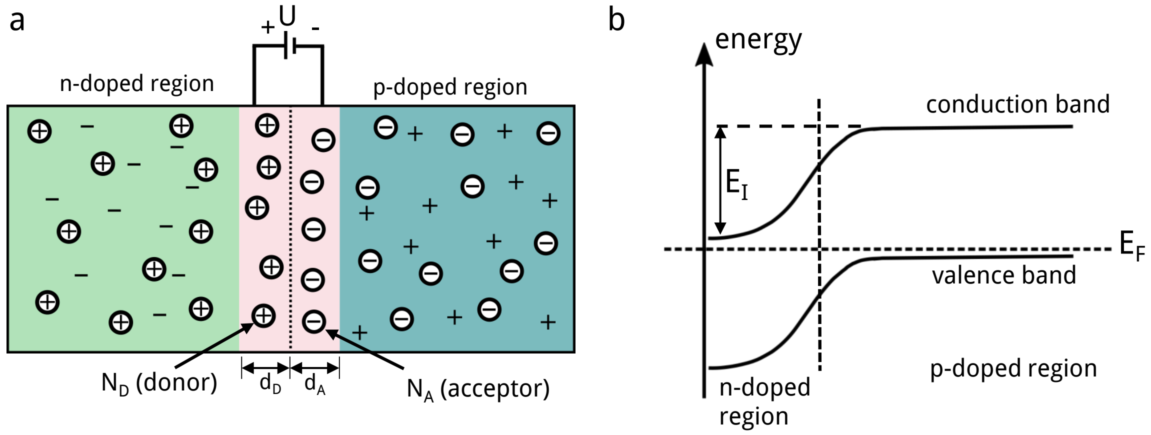

Figure 2.13: a) Schematic illustration of p-n-junction. On the left, the n-doped region, and on the right, the p-doped region are located. Majority charge carriers of both regions will drift towards the opposite charged region, leaving only fixed and oppositely charged ions that cause an electric field in the depletion zone (red shaded area). b) Sketch of the band structure in the spatial region of a p-n junction. In equilibrium, the Fermi energy E_F is constant for p- and n-doped region. The fixed ions of the doped regions cause a potential difference E_i across the p-n junction and with that also an internal electric field. Upon illumination, an electron that gets excited into the conduction band has sufficient energy to drift across the p-n junction into the n-doped region to eventually contribute to the electric current.

been doped on the left side with electron-donor dopants, while on the right side, electron-acceptor dopants have been added. As a result, on the left, there is an excess of free negatively charged carriers, while on the right there is an excess of positively charged free carriers. The free charge carriers will drift across the p-n junction, leaving behind the fixed oppositely-charged ions, particularly in the spatial region near the p-n junction. Due to this, an electric field will emerge between the p-doped and the n-doped region that acts contrary to the drift movement of the free charge carriers. The spatial region of the electric field is known as the depletion region, indicated by the red-shaded area in Fig. 2.13a. The thickness of the depletion zone, $d_D + d_A$ in Fig. 2.13a, depends on the relative doping concentration in the p-type and n-type region, N_A and N_D. Without external voltage bias or light illumination, the intrinsic field acts against the diffusion tendency of the majority mobile charge carriers and results in an equilibrium between the drifting charge carriers and their diffusion due to thermal effects or local variations of the carrier concentration [39].

The band structure in the vicinity of the p-n junction is shown in Fig. 2.13b: In the p-doped and n-doped regions, the electric potential due to the charge accumulation shifts the conduction and valence bands to smaller and larger energies, respectively. In the depletion zone, the bands are therefore bound. Upon illumination, incoming photons can excite electrons from the valence band into the conduction band upon leaving a hole in the valence band. The resulting free electron and hole have sufficient energy to cross the p-n junction towards the electric contacts and can then contribute to the electric current.

For absorber materials with large thicknesses, most of the absorbing material is too far away from the p-n junction and the free charge carriers in these regions are not affected by the internal electric field. For those carriers, only diffusion may cause them to come into the region with the electric field, in which they are then accelerated and cross the p-n-junction. However, if the typical diffusion length is too small, the charge carriers can recombine before reaching the p-n junction. The resulting radiative and nonradiative recombination mechanisms are described in Sec 2.6.2. To remedy this, one can either reduce the thickness of the absorbing medium, or change the electric properties by increasing the doping or adding layers which are higher doped. Indeed, research along these lines is a wide field conducted by many groups all over the world.

2.5.2 Solar Spectrum and Efficiency Measures

A major constraint for solar cell materials and structures is the solar spectrum arriving at the earth. Commonly used is the AM 1.5G solar irradiation photon spectrum $\varphi(\lambda)$ [41]. It is depicted in Fig. 2.14a. The peak of the spectral intensity (blue curve) is at a wavelength of around 500 nm. Having in mind that an electron-hole pair can only be generated if the energy of the incoming photon is larger than the bandgap of the absorber material, the suitability of absorber materials strongly depends on the energy irradiance provided by the sun. The solar spectrum also determines the highest achievable efficiency. From thermodynamical detailed-balance considerations, where it is assumed that light absorption is balanced by radiative recombination, a maximum efficiency for single-junction solar cells, the so-called Shockley-Queisser limit [42], was derived: $\eta_{\text{max}} = 33.7\,\%$ can be achieved for a bandgap of $E_{\text{g}} = 1.34$ eV [43]. With tandem solar cells, where absorber materials with different bandgaps are combined, this limit can be surpassed. To be precise, the maximum efficiency for an ideal infinite multi-junction solar cell is 68.2 % [44].

In Fig. 2.14a, we also plot the portion of the incoming power that is absorbed in a planar c-Si layer without any additional layers or textured interfaces. This was obtained from applying the Beer-Lambert law that will be introduced in the next subsection (Eq. 2.88), neglecting reflection losses at the air/silicon interface, and assuming one pass through the c-Si and perfect conversion efficiency. The fact that for wavelengths beyond 500 nm a major portion of the solar energy is not absorbed, demands for photon management strategies to enhance the light path inside the absorber medium and with that also the absorptance.

The blue curve in Fig. 2.14b shows the maximum efficiency dependent on the bandgap under the assumption that all recombination processes are radiative, i. e. that the internal quantum luminescence efficiency $\eta_{\text{lum}} = 1$. Due to the interplay of different (radiative and nonradiative) recombination mechanisms that we will explain in Sec. 2.6.2, η_{lum} will always be smaller than unity [46]. Figure 2.14b also shows two conversion efficiency curves for $\eta_{\text{lum}} = 0.8$ (red curve) and $\eta_{\text{lum}} = 0.6$ (yellow curve).

Besides η_{lum}, a few other coefficients that characterize the energy conversion capabilities of solar cells are important. For light-trapping purposes, the internal quantum efficiency η_{IQE} has to be considered. It expresses the fraction of the absorbed photons in the cell that generates an electron-hole pair, which subsequently contributes to the generated electric current. This describes an ideal situation, and in reality η_{IQE} will always be smaller than

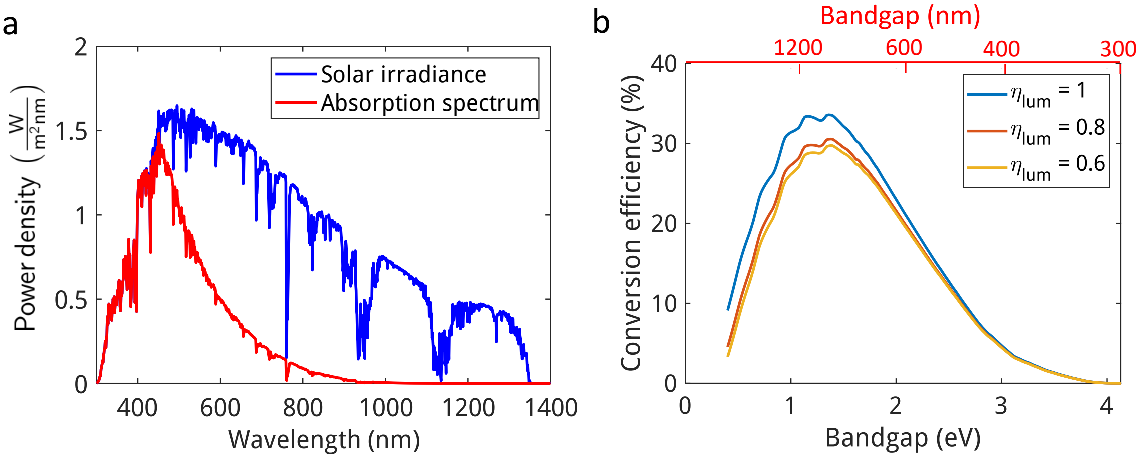

Figure 2.14: a) Solar irradiance spectrum AM 1.5G (blue curve) and portion of power that is absorbed in 1 µm thick c-Si (red curve) for normal incidence and one pass through the absorber. Reflection losses at the air/silicon interface have been neglected. Up to around 500 nm, all incoming photons are absorbed, but for longer wavelengths, the absorptance strongly decreases. The data for the solar irradiance was taken from Ref. [41]. b) Shockley-Queisser limit plotted over the bandgap energy for three values of the internal quantum luminescence efficiency [45]. The upper axis gives the bandgap energy in nanometer to allow for comparing it directly to the wavelength regime of the solar irradiance spectrum. Due to the reciprocal relation $\lambda = \frac{hc}{E}$, the spacing in both axes is not the same. The maximum efficiency for $n_{\mathrm{lum}} = 1$ is achieved at a bandgap energy of 1.34 eV and amounts to 33.7 %.

unity due to radiative and nonradiative recombination mechanisms and collection losses in the electric contacts.

Especially for measurements, the external quantum efficiency η_{EQE} is important. This is the fraction of the total light impinging on the solar cell that generates an electron-hole pair which is then collected at the contacts. The relation between η_{IQE} and η_{EQE} is

$$\eta_{\mathrm{EQE}} = A(\lambda) \cdot \eta_{\mathrm{IQE}} \,. \tag{2.84}$$

An important figure of merit to judge the optical quality and efficiency of a solar cell device is the short-circuit current density. Using the absorption spectrum $A(\lambda)$, it is calculated according to the formula [47, 48]

$$j_{\mathrm{sc}} = e \int \varphi(\lambda)\, A(\lambda)\, \eta_{\mathrm{IQE}}\, \mathrm{d}\lambda \,, \tag{2.85}$$

where e is the elementary charge. The integral boundaries depend on the specific material and bandgap. For silicon, having a bandgap of 1.12 eV, the relevant wavelength range is approximately 300 nm to 1150 nm. Perovskites have bandgaps between 1.5 eV and 2.3 eV, limiting the upper integration boundary to around 600 nm or 800 nm, depending on the specific material composition. Since j_{sc} is a spectrally averaged quantity, it renders a very useful figure of merit while assessing the light-trapping capabilities of solar cell devices. We will therefore use it in this thesis. For the calculations, we will focus on the optical properties of the structures and hence assume for the internal quantum efficiency $\eta_{\mathrm{IQE}} = 1$.

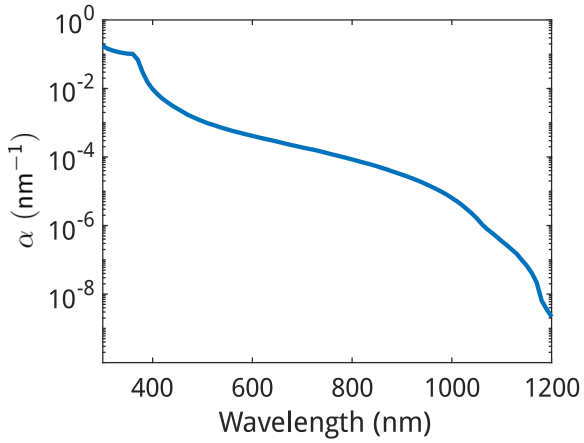

Figure 2.15: Absorption coefficient $\alpha(\lambda)$ of crystalline silicon. The values for the extinction coefficient were taken from Ref. [15]. Note the logarithmic y-axis. α varies over several orders of magnitude in the wavelength range relevant for light-trapping.

2.5.3 Concepts of Light-Trapping

Light-trapping denotes basically, on the one hand, the suppression of reflection losses when photons are incident on the solar cell device, and, on the other hand, the prevention of photons leaving the device without generating an electron-hole pair. Both of these basic tasks of light-trapping will be discussed in this thesis. In this subsection, we will give some basic expressions and introduce the Yablonovich limit and the Lambertian interface as two benchmarks for light-trapping structures. The specific forms of light-trapping nanostructures, particularly periodic and random textures, are subject of the next subsection.

According to the Fresnel equations (Eq. 2.18), the reflection at an interface between to non-magnetic media with refractive indices n_1 and n_2 is higher the larger the index mismatch of the two media is. For example, a bare air/c-Si interface has a reflectivity of 35 % at a wavelength of 600 nm and for normal incidence from the air side. The idea of anti-reflective methods is hence to minimize this reflection loss by introducing one or more thin layers between air and the absorbing medium, so that the light successively encounters interfaces with smaller impedance contrast. In this case, the intermediate medium must have a refractive index n_{ar} somewhere between n_1 and n_2.

As can be derived from the Fresnel equations, the most simple anti-reflection structure for a vacuum wavelength λ is a planar layer with a refractive index $n_{\mathrm{ar}} = \sqrt{n_1 n_2}$ [49] and a thickness of $\frac{\lambda}{4n_{\mathrm{ar}}}$. However, this only ensures perfect transmission for normal incidence and for the single wavelength λ. More layers can in principle ensure perfect transmission for more wavelengths, but experimental limitations of the total amount of layers will be always a decisive factor, and a broadband anti-reflection effect can not be achieved in this way. Theoretically, the best light-incoupling over a broad wavelength regime would be achieved by gradually increasing the refractive index from n_1 to n_2 [50, 51]. However, due to light reciprocity, anti-reflection coatings also increase the portion of outcoupled light which has not been absorbed during the first double-pass through the absorber layer. Another problem when realizing reflection coatings consisting of many layers is the potential parasitic absorption in these layers, that would act detrimental to the absorption in the main solar cell layer. In light of these problems, nanotextures are the main approach to achieve reflection suppression at the front interface.

Let us now turn to the light-trapping when the photons are already inside the absorbing medium. As given in Eq. 2.12, the general complex refractive index $\mathcal{n}(\lambda) = n(\lambda) + \mathrm{i}\kappa(\lambda)$ consists of the real-valued refractive index $n(\lambda)$ and the extinction coefficient $\kappa(\lambda)$. The latter is related to the absorption coefficient via [12]

$$\alpha(\lambda) = \frac{4\pi\kappa(\lambda)}{\lambda} \,. \tag{2.86}$$

$1/\alpha$ is the distance after which the intensity of a wave is attenuated inside a medium to $1/\mathrm{e}$ of its original value. With the absorption coefficient, one can calculate the absorptance in a homogeneous medium. The Beer-Lambert law [52, 53]

$$I(\lambda, z) = I_0 \mathrm{e}^{-\alpha(\lambda)z} \tag{2.87}$$

states that the light intensity decreases exponentially with the penetration depth z in a medium, when the initial intensity I_0 is known. Conversely, one can conclude that the absorbed energy $a(\lambda)$ increases with $1 - \mathrm{e}^{-\alpha z}$:

$$a(\lambda, z) = I_0 \left(1 - \mathrm{e}^{-\alpha(\lambda)z}\right) \,. \tag{2.88}$$

The absorptance for a given absorber thickness d is then simply

$$A(\lambda) = \frac{a(\lambda, d)}{I_0} = \left(1 - \mathrm{e}^{-\alpha(\lambda)d}\right) \,. \tag{2.89}$$

For typical solar cell materials, $\alpha(\lambda)$ varies very strongly, so that dispersive effects cannot be ignored. Figure 2.15 shows the absorption coefficient of crystalline silicon. Over the wavelength range where the solar spectrum provides the most energy, $\alpha(\lambda)$ varies over several orders of magnitude. In general, for small values of α one needs a very thick absorber to ensure complete absorption of the incident intensity, which would be too expensive and would also negatively affect the electrical properties of the cell. Therefore, light-trapping schemes are necessary to increase the effective light path within the absorbing medium [13, 54–57].

In Fig. 2.16, we show a few frequently used light-trapping textures. In Fig. 2.16a, the bare absorber medium is shown. Incoming light is lost by reflection at the front and by transmitting through the absorber material without getting absorbed. The transmittance loss can be mitigated using a metal backside mirror, which is shown in Fig. 2.16b. With this, one introduces small parasitic absorption in the metal. Still, all light which is not absorbed within a double pass through the material is lost [58].

Figures 2.16c and 2.16d show two approaches that aim to decrease the anti-reflection losses at the front side, while simultaneously keeping the light inside the absorber material. Though the idea is similar, the physical mechanisms of both approaches are different: In Fig. 2.16c, the light is randomly scattered at the front interface, as the nanostructures have a size comparable to the incoming wavelength. In contrast, the idea of the micropyramids in Fig. 2.16d is to deterministically scatter incoming light multiple times within the textured region. Since this thesis only focuses on nanotextures, we refrain from a deeper description

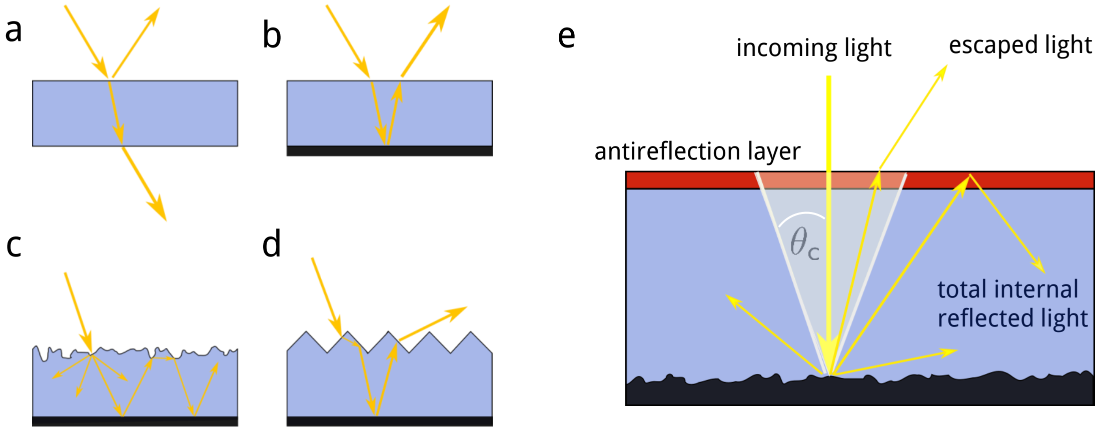

Figure 2.16: Schemes of different light-trapping methods. a) Planar absorber layer, no light-trapping schemes applied. A large amount of light is reflected at the front, another part is transmitted without being absorbed. b) A backside mirror prevents the light from being transmitted. c) Random nanotextures and d) microstructure pyramids can be used to decrease the reflection losses at the front interface. e) Sketch of the reflection from a rough back reflector, including the critical angle θ_c, outside of which the light is trapped in the absorber material. a)–d) are adapted from Ref. [59], e) from Ref. [60].

of microstructures. However, both textures have in common that they aim to increase the average path length of the first pass in the absorbing medium and to make light-outcoupling after a double pass less likely due to a lack of suitable outcoupling channels [58].

In Fig. 2.16e, we show a random rough back-reflector and the angle of total internal reflection θ_c. The aim when engineering back reflectors is to predominantly scatter light into angles larger than θ_c to avoid out-coupling at the front after only a double-pass. This is a non-trivial task, since the incident angle and the wavelength heavily affect the diffraction angle, as it was shown in Sec. 2.3. For a favorable broadband light-path enhancement, one has to use back reflectors with a very large amount of different periods, which is best realized with random textures. This is explained in more detail in Sec. 2.5.5.

An ideal interface that is often used as a kind of benchmark to compare experimental or numericals results of feasible geometries is the Lambertian interface. A Lambertian interface is characterized by a $\cos\theta$-angular distribution of the scattered light which is independent of the angular distribution of the light that is incident onto the Lambertian surface. The reflectance of a Lambertian interface can be derived by calculating the angle-averaged reflection coefficient [61]

$$R_{\mathrm{Lamb}}(\lambda) = \frac{\int_0^{\frac{\pi}{2}} R(\theta,\lambda)\cos\theta\sin\theta\,\mathrm{d}\theta}{\int_0^{\frac{\pi}{2}} \cos\theta\sin\theta\,\mathrm{d}\theta}\,. \tag{2.90}$$

The domininator simply yields 2. Assuming that one considers internal reflection in an absorber material with air on the other side of the boundary, one can define a critical angle θ_c. This, however, is with non-zero extinction coefficient κ just an approximation [62]. If the extinction coefficient is small when compared to the refractive index, the error can usually

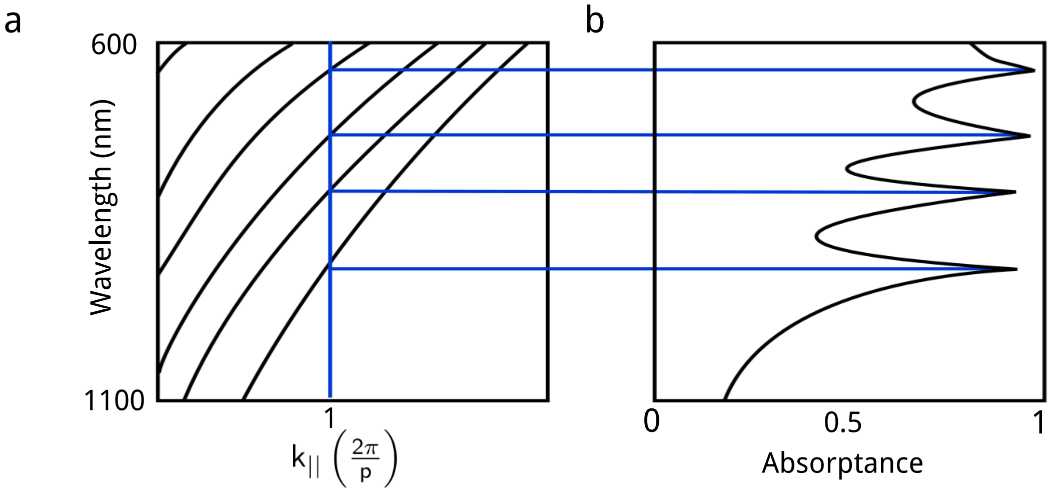

Figure 2.17: a) Generic plot of the dispersion relations of the parallel component of waveguide modes in a thin absorbing medium on top of a grating with period p. b) Absorptance response of an absorber medium, where waveguide modes as shown in (a) are present. At those wavelengths where the corresponding $k_{||}$ of the modes fulfills $k_{||} = \frac{2\pi}{p}$, distinct absorption peaks occur due to coupling the incoming light into guided modes. Adapted from Ref. [64].

be neclected and one can approximate the critical angle as if $\kappa = 0$. Splitting the integral into two parts for angles smaller and larger than θ_c, one obtains

$$\begin{aligned} R_{\text{Lamb}}(\lambda) &= \int_0^{\theta_c} R(\theta,\lambda)\sin(2\theta)\,\mathrm{d}\theta + \int_{\theta_c}^{\frac{\pi}{2}} \sin(2\theta)\,\mathrm{d}\theta \\ &= \int_0^{\theta_c} R(\theta,\lambda)\sin(2\theta)\,\mathrm{d}\theta + 1 - \sin^2\theta_c\,. \end{aligned} \tag{2.91}$$

Using Snellius' law in the second term and neglecting the first term , we obtain the frequently used formula

$$R_{\text{Lamb}} \simeq 1 - \frac{1}{n^2}\,, \tag{2.92}$$

which we will also use in this thesis.

Using a Lambertian texture, the maximum achievable enhancement factor of the light path is $4n^2$, with n the refractive index of the absorber material. This is known as the Yablonovitch limit [63]. For the derivation, the validity of the ray-optical treatment was assumed, hence the formula is only valid for absorber thicknesses larger than the wavelength, so that wave-optical effects can be neglected. Furthermore, the assumptions were perfect in-coupling of sunlight into the cell, a perfectly reflecting mirror at the backside, and the extinction coefficient of the solar cell material to be small compared to the refractive index.

2.5.4 Guided Mode Resonances

For advanced engineering of solar cell interfaces for light-trapping purposes, the concept of coupling to guided modes is exploited. The idea is schematically shown in Fig. 2.17: The wavevector component parallel to the interface, $k_{||}$, is plotted in Fig. 2.17a over the relevant wavelength regime. At wavelengths where $k_{||}$ equals an integer multiple of the reciprocal lattice vector $\frac{2\pi}{p}$, coupling to guided modes can occur. This would be equivalent to scattering into angles close to 90°. For these wavelengths, the effective light path in the absorber layer is then strongly enhanced and a large absorption enhancement can be expected. The coupling to guided modes can be seen in the absorptance spectrum (Fig. 2.17b) in the emergence of large and narrow peaks at distinct wavelengths. For light-trapping, it would be optimal to couple every wavelength to such guided mode, because then the absorptance would approach unity over the whole spectral region. Since this is not possible, one has to find other ways. One way is to use rough random textures, which we will explain in the next subsection.

2.5.5 Periodic vs. Random Light-Trapping Textures

In this subsection, we will briefly motivate the use of random rough nanotextures for interfaces in solar cells instead of periodic gratings.

In general, dielectric nanostructures are more suitable for light-trapping schemes compared to metallic nanostructures [56, 65, 66]. While metallic structures can have a large scattering cross section and near-field enhancement [67, 68], they are accompanied with significant parasitic absorption, hereby acting detrimental to the goal of maximum absorptance in the absorber layer.

As explained in Sec. 2.3.2 in the context of gratings, for scattering light at interfaces into angles different from the incident angle, the interface has to provide an in-plane momentum. Obviously, a one-period grating only provides one additional momentum contribution or integer multiples thereof. In the previous subsection, we have described that the coupling to a guided mode can increase the absorption at discrete wavelengths. These two insights can be combined to engineer interfaces for solar cells such that the coupling to modes parallel to the interface is possible for a broad wavelength regime.

Random rough textures can be viewed as an infinite number of periodic gratings that are superimposed, i. e. they offer a vast amount of available spatial frequencies where incoming light can couple to. This enables, in principle, a spectrally broader absorption enhancement by scattering the incoming light for many wavelengths into large angles. Indeed, it has been established over the recent decade that disorder can be beneficial for light-trapping purposes in photovoltaic applications [48, 69–76].

However, a disordered texture itself does not guarantee per se an optimal absorption response. Too much disorder can also reduce the absorption again [77]. It can for example occur that disorder increases the scattering within the escape cone, thereby decreasing the effective light path length and weakening the absorption. It is therefore a difficult design challenge to obtain the most out of disorder. One question in this context is, how disorder can be quantified, such that one can tailor the required amount of disorder to obtain an optimum absorption enhancement. Furthermore, the reliable large-area fabrication of

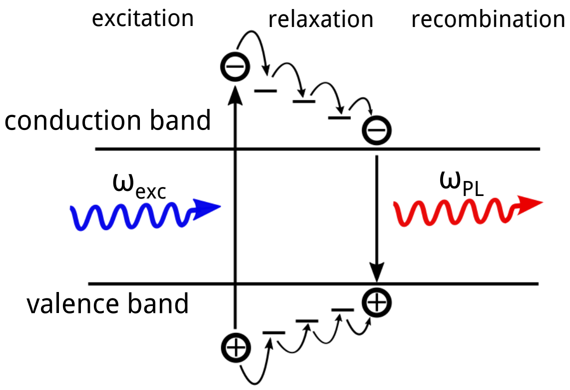

Figure 2.18: Sketch of photoluminescence. An incoming photon with angular frequency ω_{exc} excites an electron from the valence band into the conduction band, thereby creating a hole in the valence band. Subsequently, electron and hole relax towards the band edges and then recombine radiatively, which produces a photon with angular frequency ω_{PL}. Adapted from Ref. [78].

optimum disordered light-trapping surface textures is a difficult task. Both questions will be addressed and elaborated on in Ch. 3.

2.6 Photoluminescence and Recombination Mechanisms

This section introduces the photoluminescence (PL) as an important material property. Afterwards, we will introduce recombination loss mechanisms in solar cells and describe the concept of photon recycling.

2.6.1 Photoluminescence

In general, luminescence describes the property of a material to spontaneously emit electromagnetic radiation that is not due to a high temperature and black-body radiation. There are many different subtypes of luminescence, and we will limit this introduction to photoluminescence, since this is the type that is analyzed in Ch. 4

Photoluminescence is caused by the absorption and subsequent re-radiation of photons [79]. This process is illustrated in Fig. 2.18: In the first step, a photon is incident onto a material. It excites an electron from the valence band into the conduction band. How deep the electron and hole are excited into the bands depends on the frequency of the incoming photon. Then, through relaxation processes, the electron and hole thermalize back to the band edges and recombine, thereby generating a photon. This photon may either be absorbed again or leave the material. In the latter case, one observes photoluminescence. Due to this origin, the emitted energy is in principle equal to the bandgap energy. However, some intermediate energy bands due to defects, relaxation processes, or thermal noise can yield an emission energy slightly smaller or larger than the bandgap energy. This then results in an emission spectrum forming a narrow peak with the maximum at the wavelength corresponding to the bandgap energy.

In semiconductors, the process of electron-hole recombination with the eventual emission of a photon that may lead to photoluminescent radiation is an important process, and we will explain it in detail in the next subsection.

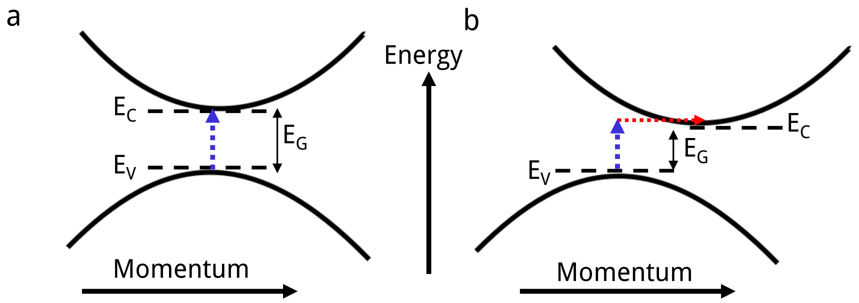

Figure 2.19: Schematic illustrations of two types of bandgaps in semiconductors: a) Direct bandgap and b) indirect bandgap. In the case of the direct bandgap, the photon, indicated by the blue arrow, does not need additional transverse momentum to shift from the valence band E_V to the conduction band E_C (or the other way round), since the edges of the valence and conduction band are at the same wavevector. For the indirect bandgap, the edges of the conduction and valence band are at different wavevectors, and thus there has to be some additional momentum contribution (red arrow) to enable the electron to change between the bands. This is typically imparted by phonons.

2.6.2 Recombination Mechanisms

As explained in Sec. 2.5.2, in a solar cell electrons and holes are created through absorption of an incoming photon. We will now consider the case where the electron and hole do not reach the contacts and therefore do not contribute to the electric current yield. Instead, the two particles can recombine, which is, due to the reciprocity of Maxwell's equations, an intrinsic property of all absorbing materials [39]. In thermal equilibrium, the rates of absorption and recombination are equal, which is known as 'detailed balance'.

Two basic mechanisms of recombination are possible, the radiative and nonradiative recombination. Radiative recombination is the inverse process of absorption, i. e. an electron and hole recombine and produce a photon. This photon may eventually leave the absorbing material or can be reabsorbed. Nonradiative recombination describes the case, when the energy that is set free upon the recombination of electron and hole is transferred to either a phonon or another electron or hole [79]. These mechanisms are always present in every semiconductor material. However, the type of bandgap present in the materials has strong influence on the prevalent recombination process. As illustrated in Fig. 2.19, a bandgap can be (a) direct or (b) indirect. In the direct case, the electron can shift between valence and conduction band without additional momentum change. The radiative recombination is therefore faster in such materials. Contrary, for an indirect bandgap, some additional momentum has to be transferred to the electron, because the band edges of valence and conduction band are not at the same wavevector. This additional momentum can typically result from coupling to phonons. Consequently, for semiconductors with indirect bandgap, the nonradiative recombination is more important, and the radiative recombination is suppressed.

If the energy of the recombination is transferred to a phonon, one also calls this Shockley-Read-Hall (SRH) recombination. It mainly occurs in the presence of impurities. Since any real solar cell material suffers from crystal defects and also contains dopants, SRH recombination is for many solar cells the dominant recombination process. The mechanism

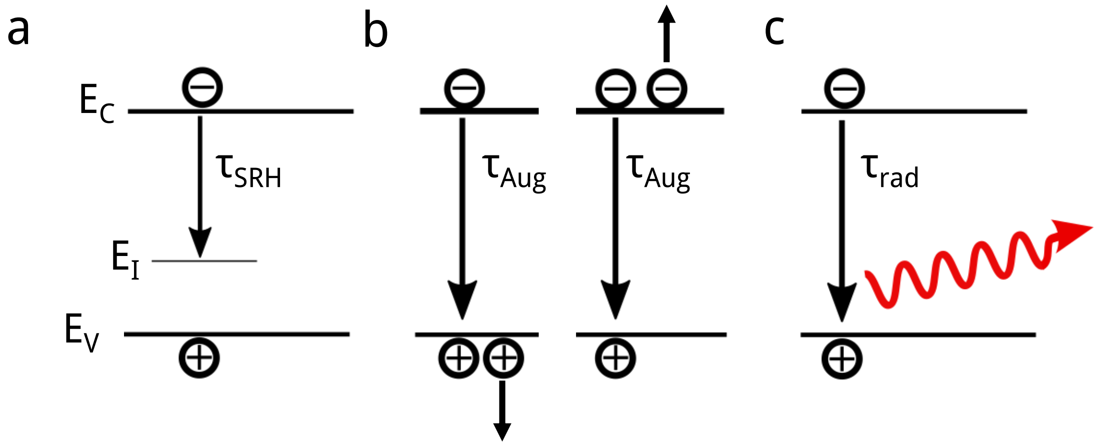

Figure 2.20: Schematic band diagram of the three types of recombination: a) Shockley-Read-Hall recombination, b) Auger recombination, and c) radiative recombination. E_C denotes the conduction band, E_V the valence band, and E_I intermediate energy levels caused e. g. by impurities. Also shown are the radiative lifetimes of the individual processes, τ_{SRH}, τ_{Aug}, and τ_{rad}. Adapted from Ref. [79].

is schematically depicted in Fig. 2.20a. The electron-hole recombination happens over one or more intermediate states that are caused by impurities. The energy E_I of these intermediate states is in between the valence band energy E_V and the conduction band energy E_C. With such intermediate states, the electron energy can be transferred to the crystal lattice in small portions. This causes a relatively high recombination rate [79].

Figure 2.20b shows the second possible nonradiative recombination mechanism, also known als Auger recombination. Here, the energy that is set free upon electron-hole recombination is imparted either on an electron or a hole. In the first case, the electron is excited high into the conduction band. In the latter case, the hole is excited deep into the valence band. In both cases, the excited electron (hole) will subsequently thermalize back into the conduction (valence) band edge upon emission of phonons [79]. In the Auger recombination, always three particles are involved. Due to this, Auger recombination is only relevant if the carrier concentration is high [79].

Finally, in Fig. 2.20c, the radiative recombination is shown: An electron transits from the conduction band to the valence band and recombines with a hole. If the resulting photon leaves the material, it contributes to the photoluminescence yield. But it can also happen that the photon excites another electron-hole pair that will eventually contribute to the electric power yield. This mechanism of recycling a radiatively emitted photon to generate another electron-hole pair is explained in detail in the next subsection.

In Fig. 2.20, the individual lifetimes associated with the recombination processes are denoted. From Eq. 2.45, we know that the decay rate of an excited state is inversely proportional to its lifetime. Hence we have $\tau_{rad} = \Gamma_{rad}^{-1}$ and analogue for the other recombination mechanisms. The total carrier lifetime is given by

$$\frac{1}{\tau} = \frac{1}{\tau_{rad}} + \frac{1}{\tau_{SRH}} + \frac{1}{\tau_{Aug}}, \tag{2.93}$$

which means that the effective lifetime is mainly determined by the smallest individual lifetime.

Similar as for solar cells, also for LEDs some coefficients exist to numerically express the efficiency of the involved processes. For the discussion here, the only relevant coefficient is the internal quantum luminescence efficiency η_{lum}. We have already introduced it in the discussion of the Shockley-Queisser limit in Sec. 2.5.2. We can now express it with the individual recombination rates as [35, 80]

$$\eta_{\mathrm{lum}} = \frac{\Gamma_{\mathrm{rad}}}{\Gamma_{\mathrm{rad}} + \Gamma_{\mathrm{nrad}}} . \tag{2.94}$$

Obviously, η_{lum} approaches unity if the nonradiative recombination rate is negligible compared to the radiative recombination rate. We will use this approximation in a later section when we analyze the mechanism of photon recycling, which will be introduced in the next subsection.

2.6.3 Photon Recycling

In solar cell materials, one aims ideally for the suppression of all recombination mechanisms. While the nonradiative recombination can be diminished to a large extent by improved crystal quality, radiative recombination can be important for the relatively new solar cell material class of perovskites [4]. For such materials, a second-order process called photon recycling needs to be taken into account. A schematic sketch of the involved processes is depicted in Fig. 2.21: First, an incoming photon generates an electron-hole pair in the absorber material. As described in the previous subsection, there is a non-zero probability that an electron and a hole recombine radiatively, hereby generating a photon. This photon may eventually transfer its energy again onto an electron-hole pair, which can then either contribute to the total open-circuit voltage and short-circuit current density, or recombine again [5–8].

In quantifying the impact of photon recycling, one typically looks at the open-circuit voltage V_{oc}, which characterizes the equibalance point of absorption and (radiative and nonradiative) recombination processes. Therefore, by increasing the portion of photons that is reabsorbed, one can enhance the V_{oc}. However, the effect is only noticeable if the parasitic absorption and nonradiative processes are largely suppressed and the nonradiative recombination rates are sufficiently low. The crystal quality that can currently be achieved should be already sufficient to see an effect due to photon recycling [81, 82]. In general, one can expect that photon recycling will be lower in nanostructured perovskite layers that are typically used for solar cell devices [83–85] as compared to planar layers due to the absence of out-coupling channels in the latter ones [81, 86–88].

The additional gain in the open-circuit voltage due to photon recycling, $\Delta V_{\mathrm{oc}}^{\mathrm{PR}}$, has only recently been derived. Rau *et al.* developed a comprehensive treatment by taking into account thermodynamical principles for the photon management in solar cells [89]. Later,

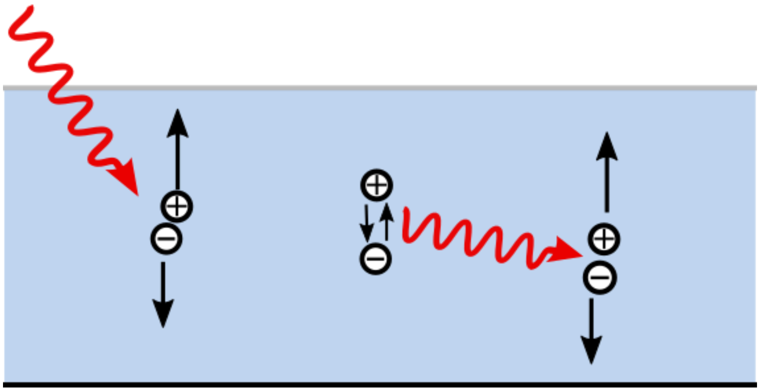

Figure 2.21: Mechanism of photon recycling. First, an electron-hole pair is generated by an incident photon. In a second step, an electron and hole recombine radiatively, hereby creating a photon. The key step is the reabsorption of this photon, accompanied by the generation of another electron-hole pair.

Kirchartz *et al.* applied this formalism to solar cell multilayers with planar and Lambertian-textured interfaces [81] and found that photon recycling can have a significant effect for such structures. A further extension was made by Abebe *et al.* by considering also situations where wave-optical calculations are necessary to calculate $\Delta V_{\mathrm{oc}}^{\mathrm{PR}}$. They derived an expression which enables the calculation of $\Delta V_{\mathrm{oc}}^{\mathrm{PR}}$ for arbitrary geometries, given that the emitted and absorbed portions of the power are known [82]:

$$\Delta V_{\mathrm{oc}}^{\mathrm{PR}} = \frac{k_{\mathrm{B}} T}{e} \ln\left(\frac{1}{1-(1-p_{\mathrm{e}}-p_{\mathrm{a}})\,\eta_{\mathrm{lum}}}\right). \tag{2.95}$$

Here, p_{a} is the propability of parasitic absorption in adjacent layers, p_{e} is the probability that the photon escapes the device, k_{B} is the Boltzmann constant, T is the temperature at which the solar cell is operated, and η_{lum} is the internal quantum luminescence efficiency as defined in Eq. 2.94.

In Sec. 4.1, photon recycling will be analyzed for nanostructured interfaces. In the next section we will introduce a few measures for corrugated interfaces.

2.7 Quantitative Description of Corrugated Interfaces

One key feature of this thesis is the investigation of a bottom-up approach to fabricate rough random interfaces. For the analysis, quantitative measures are necessary, which we introduce in this section.

Rough height profiles can be characterized by several statistical parameters. Such parameters help to compare height profiles which are quite different at first sight, but show similar behavior with regards to light scattering. Such measures can also be used to formulate guidelines for the design of favorable height profiles.

One important parameter is the root-mean-square (RMS) roughness.

$$\bar{r} = \sqrt{\frac{1}{A}\int_A h^2(x,y)\ \mathrm{d}x\ \mathrm{d}y}\,, \tag{2.96}$$

where the height profile $h(x,y)$ is assumed to cover an area A. The definition of $\bar{r}$ only makes sense if height profiles with the same mean value are compared. The RMS roughness value can give a first impression of how strongly corrugated a surface is, that means, it is a measure for the vertical roughness. The horizontal roughness, however, is not quantified at all with the RMS roughness value. For this, one needs additional measures.

The horizontal roughness can e. g. be obtained using the autocorrelation function, given by

$$ACF(\vec{s}) = \frac{\int_A h(x,y)\,h(x+s_x,y+s_y)\ \mathrm{d}x\ \mathrm{d}y}{\int_A h(x,y)\,h(x,y)\,\mathrm{d}x\ \mathrm{d}y}\,. \tag{2.97}$$

For periodic gratings, ACF returns to unity for arbitrary large $|\vec{s}|$ due to periodic repetition of the height profile's features. The correlation length ξ would be given by the distance $|\vec{s}|$ where the ACF has dropped to $1/\mathrm{e}$. The correlation length provides a lower limit for the necessary domain size that needs to be considered for scattering calculations so that statistically stable results are ensured [90]. Applying the ACF to partially periodic textures results in a heavy oscillation of the ACF over the distance from the reference point. Then, ξ would have to be constructed from the envelope of the fast oscillations. For such textures, a more suitable quantity is the height-height correlation function,

$$HHCF(\vec{s}\,) = \frac{\int_A [h(x,y) - h(x+s_x,y+s_y)]^2\ \mathrm{d}x\ \mathrm{d}y}{\int_A h(x,y)\,h(x,y)\ \mathrm{d}x\ \mathrm{d}y}\,. \tag{2.98}$$

For rough random surfaces, the height-height correlation function typically increases strongly for small distances and then saturates. The distance where the large slope changes into a horizontal saturation corresponds to the correlation length ξ.

To quantitatively analyze a textured interface concerning its Fourier components, the Power Spectral Density (PSD) is a frequently used tool. It is given by [75, 91]

$$\mathscr{P}(\vec{G}) = \frac{1}{A}\left|\int_A h(x,y)\,\mathrm{e}^{-\mathrm{i}(G_x x + G_y y)}\,\mathrm{d}x\ \mathrm{d}y\right|^2\,. \tag{2.99}$$

G_x and G_y are the reciprocal lattice vectors of the height profile in x- and y-direction, respectively. The PSD contains for each reciprocal lattice vector the amplitude of the Fourier component of the height profile. For every non-zero amplitude, a plane wave incoming to the texture might get transferred a lateral momentum. However, it is important that the amplitude does not tell anything about the portion of light that couples to this reciprocal lattice vector. To obtain the portion of light that scatters in a given direction, simple approximate tools are not sufficient. Instead, one has to rigorously solve Maxwell's equations. For such corrugated geometries, this has to be done numerically. We will therefore describe in the following section the Finite Element Method as a common technique to solve Maxwell's equations numerically.

2.8 Finite Element Method

A large part of the calculations in this thesis were done using the Finite Element Method (FEM). Therefore, we want to give a brief overview how the method works. Since there is extensive literature about numerical methods in general and the Finite Element Method in particular, we will just pinpoint the most important facts. An in-depth introduction is available e. g. in Ref. [92]. For our calculations, we used the commercially available software package JCMsuite. The accuracy and solving abilities of JCMsuite have been demonstrated in several publications [93].

The Finite Element Method is one of the main numerical techniques to solve differential equations in science and technology, among them there are Maxwell's equations. For electromagnetic problems, it solves the Helmholtz equation (Eq. 2.10), either for the electric or magnetic field, for arbitrary boundary conditions. The solution is carried out component-wise and in small spatial regions by using ansatz functions. Due to the solution in small spatial regions, simple ansatz functions like low-order polynoms are sufficient for a good approximation. Notably, the solution is carried out in frequency space. This means that to obtain the response of an optical system in a broad frequency range, one has to perform multiple calculations.

All FEM solvers employ the following steps to calculate the field distribution [94]:

1. The spatial region in which the Helmholtz equation shall be solved is discretized (meshed) into small elements characterized by nodes and edges. In three dimensions, these small finite elements are usually tetrahedrons, for simple geometries also hexahedrons are used.

2. Ansatz functions with free parameters are chosen to approximate the solution at each node and to interpolate the element in-between.

3. For each element, the ansatz functions are plugged into the Helmholtz equation and a part of the unknown parameters of the ansatz functions are related to the geometry inside the small element.

4. The solution for the whole computational domain is computed by combining the obtained element-wise equations and taking into account continuity relations of Maxwell's equations and boundary conditions to determine the unknown amplitudes of the ansatz functions.

5. From the field solution, quantities like power flow or absorptance are post-processed.

To go a bit more into detail, we will in the following only consider a scalar field. The one-dimensional Helmholtz equation reads as

$$b_1 \frac{\mathrm{d}^2}{\mathrm{d}x^2} E(x) + b_2 E(x) - f(x) = 0 \tag{2.100}$$

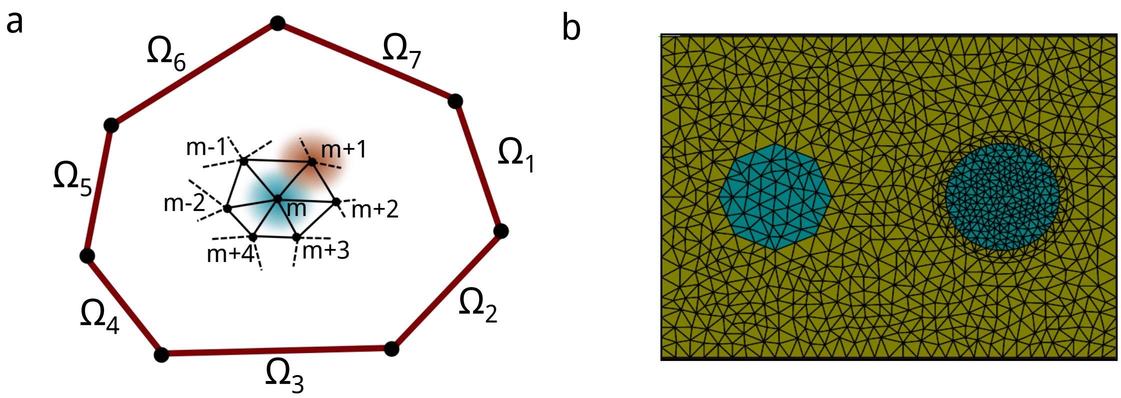

Figure 2.22: a) Schematic illustration of the edges and nodes of a triangular two-dimensional FEM grid. The blue shaded area is the region where the ansatz function pertaining to node m, ϕ_m, is valid. The neighboring ansatz function ϕ_m is displayed as red shaded spot. Also shown is the computational boundary, denoted by Ω_1 to Ω_7. Adapted from Ref. [37]. b) Different meshes for the same object. The edge size of the finite element heavily influences the accuracy of the solution, both via the interpolation of the ansatz function and the representation of the geometrical objects with the mesh.

with given parameters b_1 and b_2. The exact solution $E(x)$ at node m is approximated with the function [37]

$$E_a(x) = \sum_m a_m \phi_m(x - x_m)\,. \tag{2.101}$$

ϕ_m are ansatz functions that are only defined in the vicinity of node m. As ansatz functions, most of the time polynomials are used, because of their easy mathematical handling. The task is then to determine the coefficients a_m in a way that the error with respect to the exact solution is minimized.

A schematic graph of a two-dimensional grid is shown in Fig. 2.22a: At node m, the ansatz function ϕ_m is used (blue-shaded area), and ϕ_m is valid in the spatial domain around node m. Also shown is the validity regime of ansatz function ϕ_{m-3} for node $m-3$ (red-shaded area). The boundaries of the computational domain are indicated with Ω_1 to Ω_7.

To find values for a_m, we insert Eq. 2.101 into Eq. 2.100 and calculate the scalar product with another base function:

$$\int \phi_n(x)\left[b_1 \frac{\mathrm{d}^2}{\mathrm{d}x^2}\sum_m a_m\phi_m(x-x_m) + b_2\sum_m a_m\phi_m(x-x_m)\right]\mathrm{d}V = \int \phi_n(x) R\,\mathrm{d}V = 0\,. \tag{2.102}$$

R is the residual error for the choice of base functions ϕ_m and coefficients a_m. Plugging in the choice of basis functions ϕ_m yields a system of linear equations, that corresponds to the matrix equation [37]

$$\begin{pmatrix} M_{11} & M_{12} & \dots & M_{1m} \\ M_{21} & & & \\ \dots & & & \\ M_{n1} & \dots & \dots & M_{nm} \end{pmatrix} \begin{pmatrix} a_1 \\ a_2 \\ \dots \\ a_m \end{pmatrix} = \begin{pmatrix} f_1 \\ f_2 \\ \dots \\ f_n \end{pmatrix}, \tag{2.103}$$

where the matrix $\hat{M}$ is calculated from the lefthand side of Eq. 2.102, the numbers f_m depend on the imposed boundary conditions and source terms as given in Eq. 2.100. Inverting this matrix equation yields the unknown coefficients a_m. As it is apparent from Eq. 2.105, the size of the matrix scales with the number of nodes. Thus, FEM can become computationally very expensive, if many mesh nodes have to be considered. This can happen when the computational domain is large compared to the considered wavelength or the geometries inside the computational domain have to be meshed very fine in order to achieve the required accuracy.

In this thesis, we will analyze both driven and undriven systems. For a driven system, $f(x)$ in Eq. 2.100 is an incident electric field, for example a plane wave or a Gaussian beam, that excites the structure under investigation, typically from one side of the computational domain. Then, $E(x) = E_{\text{inc}}(x) + E_{\text{sca}}(x)$ and Eq. 2.100 can be rewritten in an equation to only determine E_{sca}:

$$b_1 \frac{\mathrm{d}^2}{\mathrm{d}x^2} E_{\text{sca}}(x) + b_2 E_{\text{sca}}(x) - b_3 E_{\text{inc}}(x) = 0\,, \tag{2.104}$$

and $E_{\text{inc}}(x)$ fulfills

$$b_1 \frac{\mathrm{d}^2}{\mathrm{d}x^2} E_{\text{inc}}(x) + b_2 E_{\text{inc}}(x) = 0\,. \tag{2.105}$$

For an undriven system, $f(x)$ in Eq. 2.100 is zero and only the boundary conditions of the computational domain need to be fulfilled. This is then an eigenvalue problem, where one seeks for the eigenfunctions and eigenvalues, which physically represent the modes sustained in the structure and the associated propagation constants (cf. Eq. 2.78).

The boundaries of the computational domain are either transparent or periodic. For periodic boundary conditions, the structures that are simulated need to be periodic in the in-plane direction perpendicular to the respective boundary. Then, the electric field at one boundary has to fulfill the Floquet-Bloch boundary condition and is related to the electric field at the opposite boundary via [37]

$$E_{\Omega_a} = E_{\Omega_b} \mathrm{e}^{\mathrm{i}\chi}\,. \tag{2.106}$$

E_{Ω_a} and E_{Ω_b} are the electric field values at the two boundaries Ω_a and Ω_b, respectively, and χ is a phase that depends on the geometry and simulation parameters. Specific types of domain boundaries are for example Perfect Electric Conductors (PEC) or more general prescriptions that fix the tangential or normal electric field components.

On the other hand, when using transparent boundary conditions, one has to make sure that the presence of the boundary of the computational domain does not affect the physical results and conclusions. To this end, Perfectly Matched Layers (PMLs) are used [95]. This comprises an artificial layer that attenuates the electromagnetic waves to avoid unphysical reflections or interferences. The quality of the PML is determined mainly by its thickness. The software JCMsuite is able to automatically refine the thickness to achieve the desired accuracy of the results.

There are two parameters that determine the accuracy of the solution obtained by FEM: First, the size of the grid elements h. The smaller the grid elements, the better the mesh reproduces the actual geometry, and the better the ansatz functions can interpolate the field distribution in the interior of an element. This is illustrated in Fig. 2.22b: Two circular objects are meshed with different mesh sizes. The object on the right side was meshed with a smaller edge length of the finite elements, i. e. a finer mesh. This directly translates to a better approximation of the circular shape by the mesh as compared to the left object. The larger edge lengths at the left object approximates the circular shape much worse, and retains clearly visible corners. In a simulation where the wavelength would be in the order of the radius of the circle, one can expect that the finer mesh will yield a much more accurate solution.

Second, the order p of the ansatz polynomials; the higher the order, the better the solution can be due to more freedom in the choice of the unknown parameters. The error of the obtained solution often scales with h^p. Due to this non-linear dependency on the grid size and the order of the ansatz functions, care has to be taken when choosing the size of the grid and the polynomial order to find a good trade-off between accuracy and required computational resources. It can also happen that a further increase of p does not increase the accuracy even more, especially, when the mesh is too coarse.

The last step is the post-processing of the obtained field. For example, the absorption in a certain domain D is calculated by integrating the divergence of the Poynting vector across the whole domain:

$$A(\omega) = \int_D \vec{\nabla} \cdot \vec{S}(\vec{r}, \omega) \, \mathrm{d}V \,. \tag{2.107}$$

We now conclude the description of the basics regarding theory, methodology, and applications, and proceed to present results obtained during the PhD in the next two chapters.

3 Interfaces for Solar Cells

In the following chapter, we will consider a bottom-up approach that uses nanospheres as building blocks to deduce rough random textures that can be employed in thin-film solar cell devices. With suitable sizes of nanospheres, the scattering properties of the resulting interfaces can be tuned to be favorable for light-trapping applications.

In Sec. 3.1, the bottom-up approach will be motivated and described in detail. To complement the theoretical considerations, we will present some experimental results from our project partners at the Martin-Luther-Universität Halle-Wittenberg. We will briefly describe two different approaches how the nanospheres on the substrate can be arranged. One approach uses experimentally obtained nanosphere distributions to extract a placement prescription, while the other one was considered in the numerical analysis. Afterwards, we will briefly describe how we retrieve the height profile data required for numerical simulations from a given nanosphere distribution on the substrate.

In going one step further, in Sec. 3.2, we will first discuss in detail the prerequisites which should be fulfilled to obtain a back reflector that is useful for light-trapping applications. The section then proceeds by providing an analysis of the monolayers formed by the nanospheres with regard to suitable diffraction properties and absorption enhancement. We will show that two nanosphere size species that are randomly distributed on the substrate are sufficient to improve the short-circuit current density as compared to an ordered texture by more than 10 %. Another important result of the section is that one can circumvent computationally expensive calculations of the short-circuit current density by calculating the diffraction efficiency at only one wavelength where light-trapping is important to be able to predict reliably the efficacy of a given surface.

In a last step, in Sec. 3.3, we will investigate the applicability of the bottom-up approach for anti-reflection front interfaces. Here, it is important to choose the nanosphere sizes in a way that the resulting height profile approaches a graded-index transition. We will show that using suitable nanosphere sizes and disorder, the reflectance at an air/silicon interface can be reduced to around 5 %. This is significantly lower than the reflectance of an ordered nanosphere texture, where the reflectance takes values up to 15 %. We will also show that the resulting textures are insensitive to the angle of the incoming light in a large angular regime.

3.1 The Nanospheres-Based Bottom-Up Approach

3.1.1 Motivation and Approach

Thin-film solar cells are sought to yield efficiencies similar to wafer-based devices, while using much less costly material. Due to its suitable bandgap [96] and the large variety and technological maturity of thin-film deposition techniques [97, 98], silicon is the most widely used absorber material in photovoltaic devices [99]. However, as we have shown in Sec. 2.5.3, the absorption coefficient of silicon rapidly decreases for wavelengths above 500 nm (cf. Fig. 2.15), which has a negative effect onto the short-circuit current density generated in the cell [56, 57]. As a consequence, many attempts have been taken to increase the absorption in thin-film layers. Nanostructures have become quite common in this context, especially gratings. Periodic [65, 66] or random [48, 69, 70, 75, 76] gratings have often been investigated, either placed at the back [100] or front side of the cell, or both. These nanostructures increase the light incoupling from air into the higher-index absorbing material and also the effective light path within the silicon.

As shown by many groups, random gratings can surpass the absorption enhancement compared to regular gratings, if the surface parameters are suitably tuned [71–74]. However, there is a tradeoff between the large, but wavelength-limited enhancement of regular gratings, and medium, but broadband enhancement of rough surfaces. So far, there have been reports about the combination of photonic crystals and disordered layers [101], deterministically fabricated quasi-random structures with supercells [102, 103], or statistical evaluation of rough surface parameters [104]. Especially the concept of supercells promises to provide broadband absorption enhancement via a densely populated Fourier spectrum while still retaining distinct diffraction orders [105, 106]. A drawback of such structures is the necessary top-down fabrication process, which renders them typically relatively expensive [55, 107].

With the idea to merge the advantages of random textures and bottom-up fabrication methods, a method to fabricate rough interfaces with tailored scattering properties has been proposed [2]. This method uses nanospheres as building blocks. The original suggestion was to immerse the nanospheres in a solution and then to deposit this solution onto a substrate via spray-coating. It has then to be ensured that the nanospheres form a monolayer while being arranged sufficiently dense. Using this method, the scattering properties of the monolayer are expected to be related to the statistical distribution of the radii of the nanospheres. By overcoating the monolayer with a metal or using it as a template, rough interfaces for solar cells or other scattering applications where a tailored scattering response is desired, are envisioned to be fabricated.

3.1.2 Experimental Realization

In an attempt to realize the above sketched bottom-up approach, our project partners in Halle have performed detailed studies of the deposition process to find parameters that allow placing the nanospheres as a monolayer. Experiments were done by Peter Piechulla in the group of Prof. Ralph Wehrspohn. The results were reported in Ref. [3], to which we have contributed. We will briefly summarize a few of the findings to provide a frame for the upcoming numerical considerations.

The procedure of the deposition process is illustrated in Fig. 3.1. First, a colloidal suspension is prepared, that contains nanospheres consisting of polymethylmethacrylate (PMMA) dispersed in an aqueous solution. The size distribution of the nanospheres is subject to an optimization process depending on the envisioned application. Another property that has

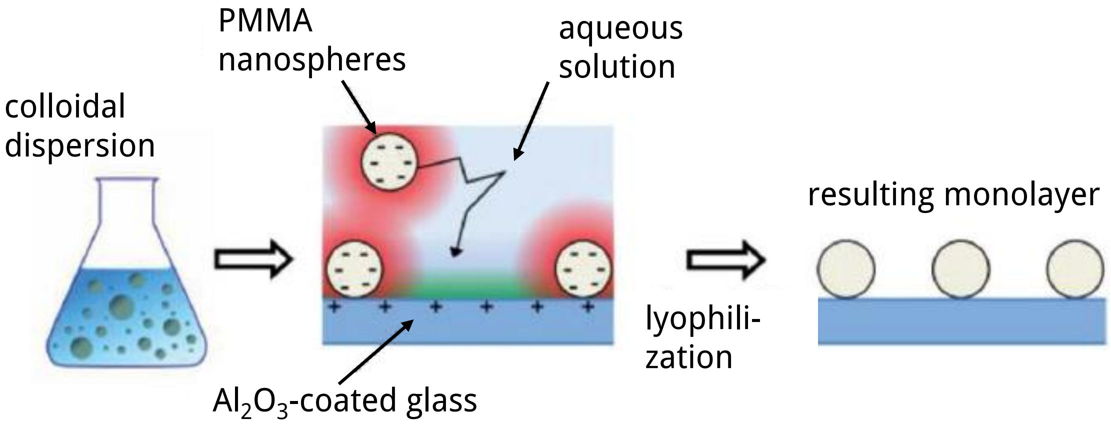

Figure 3.1: Experimental procedure of the bottom-up approach. A dispersion with nanospheres is prepared, and the substrate, consisting of an Al_2O_3-coated glass, is immersed into the dispersion. The nanospheres will adhere to the substrate, and after the substrate is removed from the dispersion, lyophilization is applied to avoid aggregations of nanospheres while the sample is dried. Reprinted with permission from Ref. [3] (Copyright 2018 Wiley).

to be carefully adjusted is the ionic strength of the dispersion, since it directly affects the average nearest-neighbor distance of the resulting monolayer, as will be illustrated below.

As a substrate to host the nanosphere monolayer, a microscope glass is covered with a thin Al_2O_3 layer, e. g. via magnetron-sputter deposition. The substrate is then immersed into the prepared colloidal dispersion. Opposite surface charges of the substrate and the nanospheres then cause the nanospheres to adhere to the substrate in the form of a monolayer. The substrate is then removed after a certain time from the dispersion and dried using lyophilization to prevent the nanospheres from aggregating due to surface tension.

3.1.3 Height Profile Retrieval

In the following, we will briefly sketch two different numerical procedures to obtain nanosphere monolayers. The first approach will obtain the nanospheres arrangement as encountered in the experiments that have been described in the previous subsection. There, the nanosphere monolayer has significant gaps between neighboring nanospheres, and the nearest-neighbor distance can be tuned by the ionic strength of the nanospheres. Details are found in Ref. [3]. Afterwards, we will describe a random placement algorithm where the nanospheres lie directly next to each other, so that they are touching the neighboring nanospheres. The latter placement algorithm was used for the numerical simulations in this thesis, since at the time when most of the calculations have been performed, the experimental approach was not yet available.

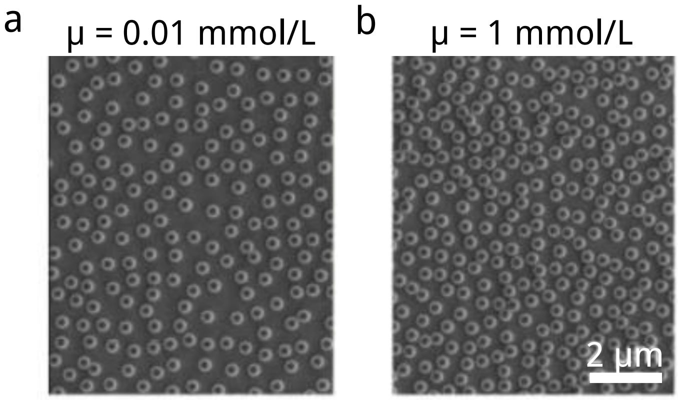

Figure 3.2: Influence of the ionic strength μ of the nanosphere dispersion on the density of the nanospheres on the substrate. The ionic strength μ is in a) 0.01 mmol/L and in b) 1 mmol/L. A higher ionic strength leads to a higher density of nanospheres on the substrate due to the larger electrostatic interaction between the nanospheres and the substrate. Reprinted with permission from Ref. [3] (Copyright 2018 Wiley).

Experiment-based Placement Algorithm

In the experiments, monolayers as depicted in Fig. 3.2 were obtained. The gaps between the nanospheres are in the order of the nanosphere radius or larger, and it has turned out to be experimentally very difficult to produce randomly arranged monolayers of nanospheres with no separation between the nanospheres. In Fig. 3.2a, the ionic strength of the nanosphere dispersion was $\mu = 0.01\,\text{mmol/L}$, while in Fig. 3.2b, $\mu = 1\,\text{mmol/L}$.

The algorithm that reproduces the nanosphere distributions from the experiment works as follows: First, a mean distance $\bar{d}$ between the nanospheres and a standard deviation σ is chosen, e. g. extracted from experiments. Then, in a predefined area a random x- and y-coordinate are initialized. For the first six nanospheres that are to be placed, the placement is simply performed if no overlay to already placed nanospheres occurs. During all the placements, it is assumed that the nanospheres can not lie partially below each other. Beginning with the seventh nanosphere, first, overlapping nanospheres are ruled out, and then the six nearest neighbors of the tested placing point and the distances d^{NN} to them are identified. For each of these nearest neighbors (abbreviated in the following as NN), the probability $p_{\text{stick}}^{\text{NN}}$ that the nanosphere finally sticks to the initialized place will be calculated with the formula

$$p_{\text{stick}}^{\text{NN}}(x,y) = \begin{cases} \exp \frac{\left(d^{\text{NN}}(x,y)-\bar{d}\right)^2}{2\sigma^2} & d^{\text{NN}}(x,y) \leq \bar{d} \\ 1 & d^{\text{NN}}(x,y) > \bar{d} \end{cases}. \tag{3.1}$$

The total probability is then obtained by multiplying the six individual probabilities. To finally decide if the nanosphere will stick to the initialized place, the total probability is compared to a random number between zero and one, and only if the probability is larger than the random number, the nanosphere is actually placed. This process is repeated up to a certain limit that needs to be predefined at the beginning.

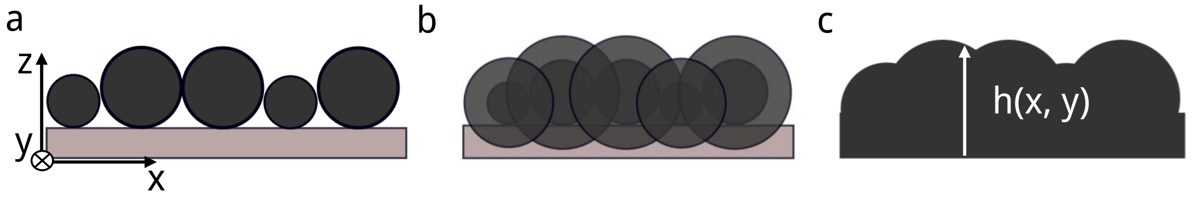

Figure 3.3: Steps that have been used to retrieve the height profile, illustrated with a two-dimensional cross section of a texture. a) Random placement of nanospheres. b) Isotropic radial enhancement to model the ALD. c) Homogenization of the combination of nanospheres and substrate. Reprinted from Ref. [108] (Copyright 2018 Optical Society of America).

Densely-packed Nanosphere Monolayer

With the assumption of nanospheres that are densely-packed, the monolayer is numerically generated as follows: Nanospheres of the desired radii and occurrence fractions are initialized. An area which should be completely covered by the nanosphere monolayer is chosen, and the approximate number of nanospheres needed to cover the area is determined. With this, it is ensured that the occurrence fraction of the nanospheres is not distorted after the deposition, as it would happen if a large number of nanospheres could not be placed inside the area. The required approximate number of nanospheres has to be determined individually for different size distributions.

To place a nanosphere inside the area, a random x-coordinate is initialized that is inside the area. Then, the largest possible y-coordinate that is still inside the area is chosen and successively decreased until the nanosphere hits either an already placed nanosphere or the boundary of the area. While decreasing y, it is tested along x if there are positions where the nanosphere could be moved even further in y-direction. This is done to ensure uniform filling along x. This process is repeated until either all nanospheres are placed into the area or the area is filled completely. Like in the previously described algorithm, we exclude the possibility that nanospheres could partially be located below a larger nanosphere species. It can of course happen that the number of nanospheres in the initialized set was not enough to cover a sufficient fraction of the area, or that it were too many nanospheres and a large portion could not be placed. Then, the result is discarded, the initial number is adapted and the placing process is restarted.

Calculation of the Resulting Height Profile

A layer of nanospheres, no matter if densely-packed or with gaps, does not immediately yield a continuous surface, as illustrated in Fig 3.3a. The next step is therefore to add an additional thin layer with the aim to homogenize the texture. This can be e. g. done using atomic layer deposition (ALD) [109]. To account for the isotropic and normal growth process of an ALD, we radially enhance the nanospheres on the substrate by a thickness δr that corresponds to the thickness of the ALD layer, see Fig. 3.3b. The height profile is then taken as the highest continuous surface resulting from the combination of radially enhanced nanospheres and substrate (cf. Fig. 3.3c). We then remove a small strip at each side of the considered area to ensure that edge effects in the placement algorithm do not affect the later calculations. We also continue the height profile periodically in the lateral directions by continuously changing a small strip at two adjacent sides to achieve a smooth transition to the opposite side of the texture (i. e. to the next unit cell). This will enable FEM calculations with periodic boundary conditions. Finally, in order to be able to compare different height profiles with respect to statistical quantities, we set the average height to zero.

The resulting height at each x-y-point is calculated by first determining which nanospheres are close enough to the considered point to have an effect on the height at that point. For all nanospheres that fulfill this requirement, the resulting height is determined with the formula

$$h(x,y) = \max_{k\in\mathscr{K}} \left\{ r_k + \sqrt{(r_k+\delta r)^2 - d_k^2} \right\} , \tag{3.2}$$

where r_k is the radius and d_k is the distance of the center of nanosphere k to the respective x-y-point out of the set of nanospheres $\mathscr{K}$ that are close enough. Of course, this set can be empty, and the formula is only applicable when d_k is smaller than the enhanced radius $r_k + \delta r$. If the set is empty, the formula is not applied, and the height is chosen to be δr in accordance with the properties of the isotropic atomic layer deposition.

3.1.4 Summary of the Nanospheres-Based Bottom-Up Approach

In this section, we have described the nanospheres-based bottom-up approach to fabricate rough random textures. We have summarized some experimental findings regarding parameters that influence the density of the resulting monolayer of nanospheres. We have also described two placement algorithms how the nanospheres could be arranged on the substrate, and we showed how the resulting rough texture is obtained from the monolayer. Such rough textures are considered in the next sections for rough interfaces in solar cells.

3.2 Back Reflector Optimization Strategy

In this section, we will put emphasis on the proper engineering of the morphology of solar cell back reflectors to increase the absorption. We will show that the above described nanospheres-based bottom-up approach can be used to achieve interfaces with favorable scattering properties over a broad wavelength regime. The nanosphere sizes and occurrence fractions are tailored such that the resulting textures possess a Fourier spectrum that favors coupling of normal incident light to oblique scattering angles in a large spectral domain. Using the limited parameter space of only two different nanosphere sizes, we will discuss how the tendency of the short-circuit current density can be estimated using the Power Spectral Density and diffraction calculations. With the described computationally cheap strategy, the necessity for full-wave simulations is thereby strongly reduced. The contents of this section to a large extent has been published in Ref. [108].

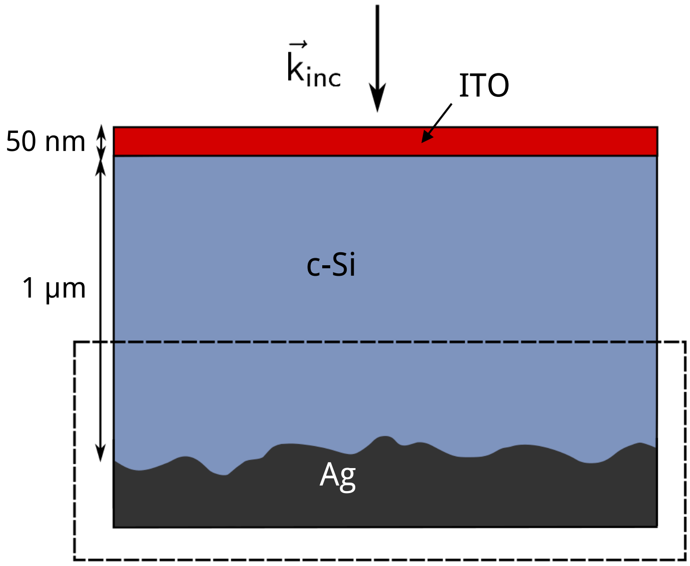

Figure 3.4: Two-dimensional cross section of the considered solar cell geometry: The silver back reflector is textured with the height profile obtained from the nanospheres-based bottom-up approach. The absorbing medium is c-Si with a thickness of 1 µm, followed by a planar ITO layer. Above that, air is assumed, and the light is incoming from the air side at normal incidence. The complete stack is simulated to obtain values for the short-circuit current density, while the dashed box encloses that part of the structure that is used for the diffraction simulations. Adapted from Ref. [108] (Copyright 2018 Optical Society of America).

3.2.1 Design Strategy

In the following, we will consider the multilayer structure shown in Fig. 3.4. It consists of a silver back reflector with the rough texture, a 1 µm thick crystalline silicon absorber layer (measured to the average height of the rough texture), and a flat ITO front anti-reflection layer with a thickness of 50 nm. The front was not patterned with any anti-reflection nanostructures to clearly identify the scattering properties of the back reflector.

First, we want to clarify in what kind of scattering response we are specifically interested. For absorption enhancement, the Beer-Lambert law (Eq. 2.88) prompts for an enlarged light path inside the absorbing medium. However, for thin-film cells the thickness of the absorbing medium is intrinsically limited. To mitigate this, the effective light path length in the absorbing medium can be enhanced and thereby the probability, that the traversing light is being absorbed, increased [54]. An extended light path corresponds to light that has a large wavevector component parallel to the interfaces, i. e. the considered plane wave propagates at a certain angle relative to the normal vector of the interface. Suppose we have incident light with parallel wavevector $\vec{k}_{||,\mathrm{inc}}$; according to the grating equation 2.61, first-order scattering to a wavevector with a component parallel to the surface, $\vec{k}_{||}$, can only occur if the height profile provides a corresponding spatial frequency $\vec{G}$, so that it holds $\vec{k}_{||} = \vec{k}_{||,\mathrm{inc}} + \vec{G}$.

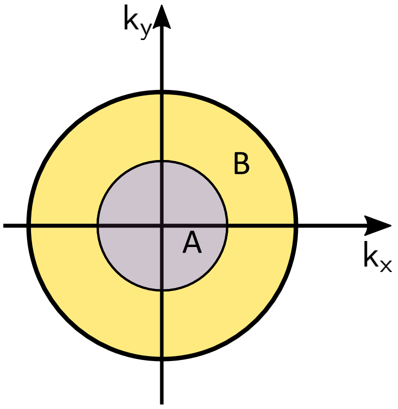

Figure 3.5: Envisioned annulus in Fourier space. Region A corresponds to the angular interval smaller than the critical angle, where light can couple out from crystalline silicon according to Eq. 2.25. The outer radius of region B is equivalent to the maximum propagating wavevector in c-Si. Hence, B is the favorable wavevector interval into which scattering should predominantly occur. Adapted from Ref. [108] (Copyright 2018 Optical Society of America).

We are considering normal incident light, $\vec{k}_{||,\mathrm{inc}} = 0$, which means that to achieve diffraction into modes with large parallel k-vector $\vec{k}_{||}$, the surface has to fully provide such a momentum, i. e. there have to be Fourier components with sufficiently large inverse grating vectors $|\vec{G}|$. This, however, does not mean that one should simply choose textures with very large G-vectors. If $|\vec{G}| > k_0 n_{\mathrm{Si}}$, the mode becomes evanescent, which can result in significant parasitic absorption in the metal back reflector due to the possible coupling to surface plasmon polaritons. An absorption gain in the c-Si due to the rough surface might thus be overshadowed by an increase of the parasitic absorption. This leads to the conclusion that $|\vec{G}|$ should not be too small, but also not too large. Using this reasoning, a minimal and a maximal value of $|\vec{G}|$ has to be defined in order to achieve the desired scattering properties in the absorbing material, so we are heading for an annulus region (see Fig. 3.5).

The annulus has to be chosen in a way to maximize the integrated absorption in the entire wavelength range of interest. The geometrical parameters of the annulus depend on the material properties and the incoming solar radiation. Photons with energy significantly higher than the bandgap, i. e. wavelengths shorter than 500 nm, are already absorbed to a large extent within the first few hundred nanometers. Absorption enhancement in this wavelength regime can thus already be achieved by incorporating a good anti-reflection coating at the front side of the cell. In principle, only for those wavelengths for which a double pass through the material is not enough to ensure complete absorption, light-trapping structures have a noticeable effect. This is the case for wavelengths beyond 600 nm. However, with the peak of the solar irradiation spectrum at around 500 nm (cf. Fig. 2.14a), light-trapping structures that predominantly affect wavelengths around 1000 nm would not yield a relevant absorption enhancement.

Taking these side conditions into account, for crystalline silicon the main target wavelength region to enhance the absorption is approximately 600 nm–900 nm. As a proof-of-principle, we will choose a wavelength of 700 nm to demonstrate how suitable parameters can be chosen to achieve good absorption enhancement. For the inner radius of the target annulus, we will choose a wavenumber that corresponds to the angle of total internal reflection at a c-Si/air interface at a wavelength of 700 nm. This means that diffracted light stays trapped within the light-absorbing layer when considering secondary diffraction events.

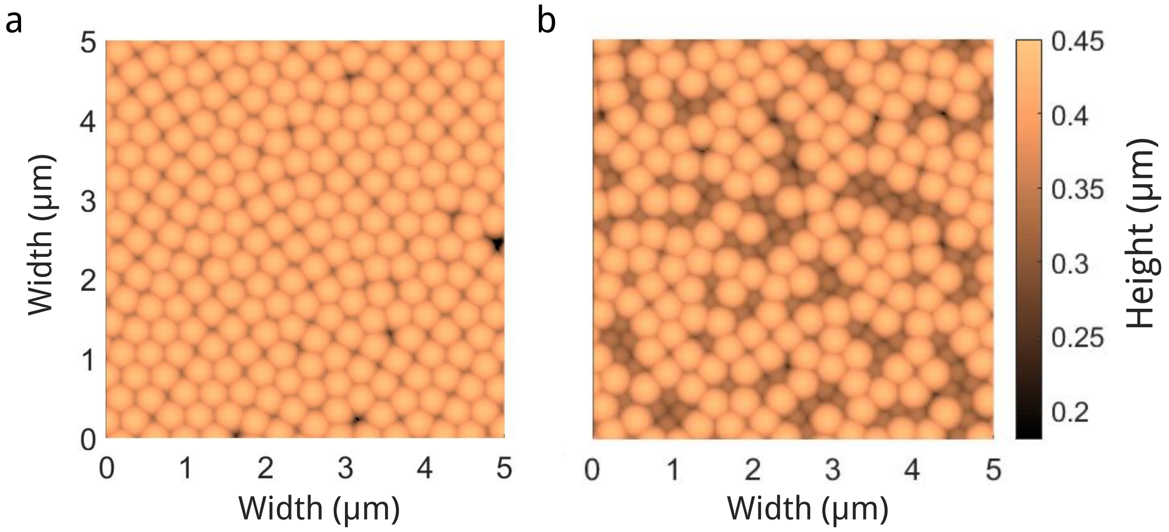

Figure 3.6: a) Height profile with one nanosphere size species (170 nm radius). b) Height profile with two nanosphere size species in the occurrence fraction 60 %:40 % (170 nm and 120 nm). Both height profiles were obtained with the algorithm described in Sec. 3.1.3. Afterwards, the nanospheres were enhanced radially by 100 nm to model the isotropic growth process of the atomic layer deposition. It is apparent that the addition of small nanospheres destroys the order that was locally present when only one nanosphere size was used. Adapted from Ref. [108] (Copyright 2018 Optical Society of America).

The outer radius will be, as already discussed, the wavenumber corresponding to the largest propagating mode in c-Si at this wavelength.

In the following, we try to achieve the desired scattering properties with nanospheres of two different sizes. We use the placement algorithm that yields densely-packed monolayers as described in Sec. 3.1.3. With two nanosphere sizes, we can be sure that we will obtain a sufficiently large degree of disorder. The statistical features of the rough textures resulting from such disordered nanosphere layers only depend on the nanosphere sizes and the fractions of the used size species. The idea behind using two nanosphere size species is to enable a larger positional disorder [110].

The thickness of the additional layer deposited by ALD has to be chosen with care: A too thick layer would result in smearing out the surface features, while a too thin layer might result in very steep surface features that can be detrimental for the electrical properties. While steep features are desirable for anti-reflection front textures, as we will show in the next section, very pronounced metallic features might lead to plasmonic losses. Unaffected by the ALD layer are the horizontal surface features, e. g. the correlation length, as long as the ALD thickness is not much larger than the nanosphere size. For our purposes, we will use in the following an ALD thickness of 100 nm. This ensures not too much smoothing of the surface roughness and retains a large enough root-mean square (RMS) roughness. In Fig. 3.6, we show two different monolayers generated with the placing algorithm that was described in Sec. 3.1.3. In Fig. 3.6a, only one nanosphere size species with a radius of 170 nm was used. One can see areas in which some local hexagonal order exists. In Fig. 3.6b, another size species with radius 120 nm was added so that the smaller nanospheres have an occurrence fraction of 40 %. In this case, no order is remaining.

Our simulations are done with periodic boundary conditions along the horizontal x-y-plane. In z-direction we use Perfectly Matched Layers at the top and bottom of the unit cell. More details of the FEM settings can be found in Ref. [108]. We use literature data for the permittivity of c-Si [15], ITO [111], and silver [27].

3.2.2 Semi-Analytical Treatment

As described in Sec. 3.1.3, it is numerically easy to infer the height profile from a given nanosphere distribution on the substrate. Consequently, one has also access to the Fourier components that are present in the rough surface. By tailoring the nanosphere sizes, one can tailor the amplitudes of the Fourier spectrum to achieve favorable textures. In Eq. 2.99, we have specified the Power Spectral Density (PSD) as a tool to access the Fourier picture of a height profile. For the numerically determined height profile, the formula has to be adapted to be applicable to discrete height profiles:

$$\mathscr{P}(\vec{G}) = \frac{1}{L_x L_y} \left| \sum_m \sum_n h(x_m, y_n) \mathrm{e}^{-\mathrm{i}(G_x^m x_m + G_y^n y_n)} \Delta L_x \Delta L_y \right|^2 . \tag{3.3}$$

Here, L_x and L_y are the lateral sizes of the texture and G_x^m and G_y^n are its spatial frequencies in x- and y-direction, respectively, belonging to diffraction orders m and n. ΔL_x (ΔL_y) is the step size of the discretization of the height profile in x- (y-)direction. It holds $G_x^m = \frac{2\pi}{L_x} m$ and similar for G_y^n.

The first step is to find an initial nanosphere size that yields maxima of the PSD in the target annulus region. As shown in Fig. 3.7a, such Fourier distribution can be obtained for a radius of $r_{\text{main}} = 170\,\text{nm}$. The depicted PSD spectrum was retrieved from a $5\,\mu\text{m} \times 5\,\mu\text{m}$ area. The white dashed circle marks the annulus size that we previously deduced. As we can see, the peaks of the PSD lie inside the annulus region. The size of the nanospheres and, in case of more than one size species, also the size difference determine the size of the vertical and lateral features. The latter have a direct impact on the components in Fourier space that are populated. If the radii and thus the lateral feature sizes are small, the PSD has maxima at large spatial frequencies. On the other hand, large radii lead to large lateral feature sizes and to PSD maxima at small spatial frequencies. With this in mind, the choice of $r_{\text{main}} = 170\,\text{nm}$ is made to avoid both PSD components at too small and too large spatial frequencies, and to get PSD components in the envisioned annulus region.

Having an initial nanosphere size with distinct circular peaks, the peaks shall be broadened to achieve a spectrally broadband absorption enhancement. With just one nanosphere size, the amount of disorder that is needed for a broadband response cannot be increased anymore, so we now introduce a second nanosphere size species. As it will turn out, two nanosphere sizes are sufficient to significantly increase the absorptance and the short-circuit current density. We chose the radius of the additional perturbing nanospheres as $r_{\text{pert}} = 120\,\text{nm}$; the reason for this choice is to introduce a size species with a large enough difference in radius to

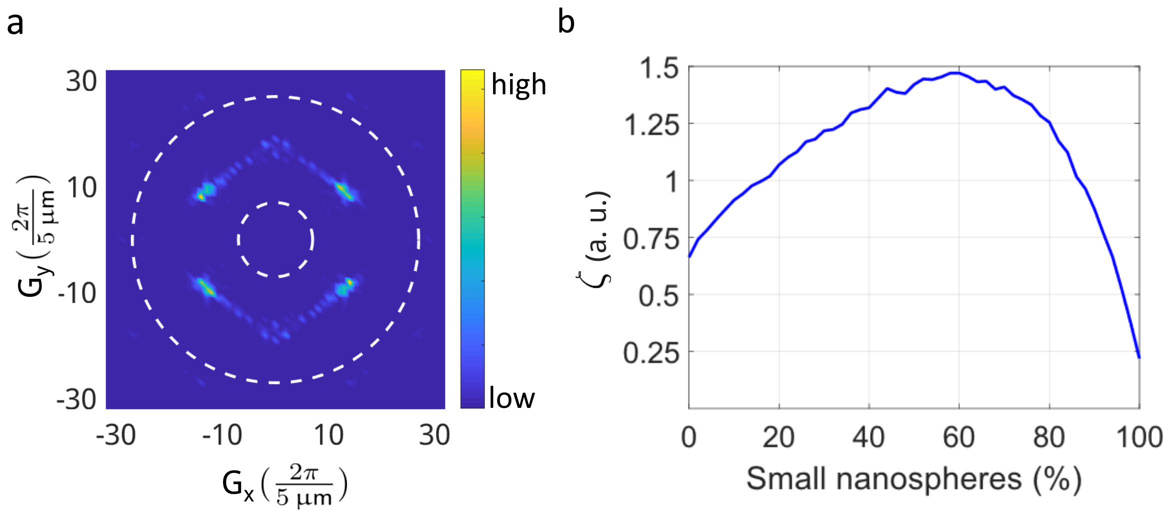

Figure 3.7: a) Example Power Spectrum Density of a 5 µm × 5 µm height profile that consists of one nanosphere size species with radius 170 nm and an ALD layer of 100 nm. The white dashed circles mark the target annulus region. b) The quantity ζ as defined in Eq. 3.4 is plotted for varying occurrence fraction of the two nanosphere size species 170 nm and 120 nm. At a fraction of 60 % of the small nanospheres, the sum of the PSD components in the annulus is maximal and then drops until the monolayer consists only of nanospheres with 120 nm radius. Adapted from Ref. [108] (Copyright 2018 Optical Society of America).

get a notable perturbation effect. Moreover, we chose it smaller than the original nanosphere sizes because smaller radii translate to PSD components at larger spatial frequencies, which is desirable.

We are interested in maximizing the PSD in the target annulus. We therefore define

$$\zeta = \sum_{\substack{G_x^m, G_y^n, \\ k_{\mathrm{TIR}} < G_{||} < k_{\mathrm{Si}}}} \mathscr{P}(G_x^m, G_y^n) \tag{3.4}$$

as figure of merit, with the in-plane spatial frequency $G_{||} = \sqrt{(G_x^m)^2 + (G_y^n)^2}$ scattering into diffraction channel (m, n). k_{TIR} is the wavenumber that belongs to the critical angle at the c-Si/air interface, and $k_{\mathrm{Si}} = n_{\mathrm{Si}} k_0$, both for a vacuum wavelength of 700 nm. The summation only considers those spatial frequencies G_x^m, G_y^n that lie within the annulus. A plot of ζ for the two nanosphere sizes 120 nm and 170 nm for increasing fraction of the small nanospheres is shown in Fig. 3.7b. ζ was calculated in steps of 2 %, and for each size fraction 20 different height profiles with the same occurrence fraction of the two size species have been evaluated. At 60 % occurrence fraction of the small perturbing nanospheres, a peak can be observed. This clearly indicates that for this particular fraction of perturbing nanospheres, the largest amount of the angular spectrum is contained in the desired domain.

A necessary condition that has to be considered in order to use the PSD as a reliable predictor for the scattering response of a rough interface is the size ratio between the incident wavelength and the typical vertical feature size of the texture. Only if the wavelength is much

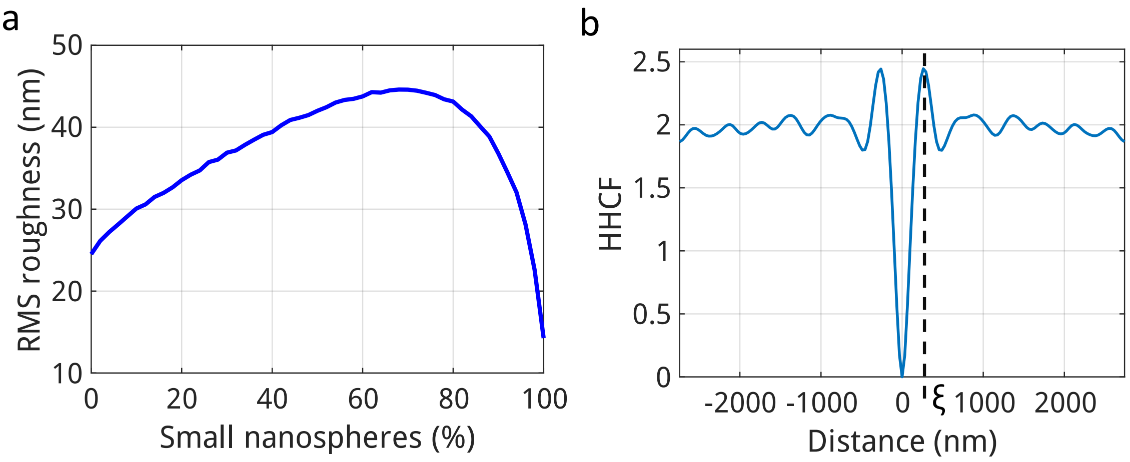

Figure 3.8: a) RMS roughness, calculated with Eq. 2.96, of the rough random height profile obtained from a nanosphere monolayer with additional ALD coating thickness of 100 nm. The monolayer consists of two size species (170 nm and 120 nm), and the relative occurrence fraction is varied in steps of 2 %. A maximum RMS roughness of 44 nm at 68 % is obtained. Adapted from Ref. [108] (Copyright 2018 Optical Society of America). b) Plot of the height-height correlation function of an example rough height profile made from 20 % nanospheres with radius 170 nm and 80 % nanospheres with radius 120 nm. The distance where the large slope changes into an almost horizonal function is the correlation length ζ.

longer than the vertical feature size, i. e. if the surface can be considered shallow, the PSD can be viewed as a good approximation to the diffraction pattern [75]. To further explore how the scattering behavior changes if ζ increases, we make use of another measure, namely the RMS roughness, defined in Eq. 2.96.

In Fig. 3.8a the RMS roughness is shown for two nanosphere sizes (170 nm and 120 nm) and increasing portion of the smaller nanospheres. Basically, we consider here the same interfaces as already considered in Fig. 3.7. The initial value in the case without perturbing nanospheres is 24 nm, and continuously increases up to 44 nm for the case of 68 % perturbing nanospheres. These are typical values of light-scattering surfaces, e. g. the well-known Asahi-U texture has an RMS roughness of 35 nm [75].

With decreasing average size of the building blocks of the monolayer, the RMS increases. This can be explained by the fact that two nanospheres of different sizes have a larger slope and potentially also larger gaps between them as compared to nanospheres of the same size species. However, an opposite effect sets in if the fraction of the small nanospheres is chosen too high. In particular, we can see that when the portion of the small nanospheres further increases, the RMS roughness decreases again. At a fraction of 100 % for the small nanospheres, the RMS roughness drops to 14 nm. This is, not surprisingly, below the RMS roughness for only nanospheres with radius 170 nm. The highest RMS roughness is not at 50 %, because the occurrence fraction pertains to the number of nanospheres, not to the area they cover. At a ratio of 50 %:50 %, the larger nanospheres still cover a much larger area than the smaller nanospheres. This makes it less probable to achieve steep feature sizes in-between two different-sized nanospheres.

Since the RMS roughness quantifies the corrugation of a surface, it can be regarded as a measure of how strong a surface scatters. However, it does not say anything about the spatial frequencies into which the scattering is most dominant. But we can combine now insights obtained from analyzing the PSD and RMS roughness depending on the fraction of the perturbing nanospheres. This leads to the conclusion that the increase of the PSD for increasing portion of perturbing nanospheres is actually due to larger scattering strength in the target annulus region, as desired. However, as we are using an incoming plane wave with a vacuum wavelength of 700 nm, the wavelength inside the c-Si (refractive index $n = 3.77$) is 186 nm. This is only around four or five times the RMS roughness, which indicates that the PSD might not be a good approximation when the nanospheres become quite large, or, considering two nanosphere sizes, when the size difference of the two nanospheres is quite large. We therefore now turn to full-wave diffraction simulations.

3.2.3 Diffraction Results

As shown in the previous subsection, the PSD can give a good initial guess, but might fail when the surface roughness gets too large. In comparison, full-wave simulations will yield exact, but computationally expensive results. Hence, we first limit ourselves to a simulation domain that is given by the dashed box in Fig. 3.4, since we are only interested in the diffraction orders and not in the absorption in the complete multilayer stack. For the same reason, we neglect the extinction coefficient of c-Si. Regarding the necessary size of the computational domain, it was shown that a statistically meaningful result can be ensured if the domain size exceeds either three times the correlation length or five times the typical lateral feature size [90]. For us, the lateral feature size can be approximated to be the diameter of the prevalent nanosphere size species. Assuming the larger nanospheres to be dominant, this means that $LFS \approx 2r_{\mathrm{main}} = 340\,\mathrm{nm}$. Having the smaller nanospheres as the dominant size species, the LFS is smaller accordingly. Consequently, by choosing the width of the simulation domain to be at least 2.5 µm × 2.5 µm (which is approx. seven times larger than the LFS), we can be confident that our results are statistically solid. Another way to see this is by calculating the correlation length directly for a few height profiles via the height-height correlation function (HHCF, Eq. 2.98). A plot of the HHCF for a height profile made from 20 % nanospheres with radius 170 nm and 80 % nanospheres with radius 120 nm is shown in Fig. 3.8b. From the condition that ξ is the distance where the large slope turns into a merely horizontal (albeit oscillating) function, we find $\xi \approx 300\,\mathrm{nm}$. This demands a size of the simulation domain of around 1.5 µm, confirming that the chosen spatial extent of the computational domain is sufficient.

Based on the same considerations that lead to the definition of ζ in Eq. 3.4, we now define the quantity δ as the sum of the diffraction components in the annulus region:

$$\delta = \sum_{\substack{k_x^m, k_y^n, \\ k_{\mathrm{TIR}} < k_{||} < k_{\mathrm{Si}}}} |\vec{E}_{\mathrm{ref}}(k_x^m, k_y^n)|^2 \frac{k_z}{k_{\mathrm{Si}}} \,. \tag{3.5}$$

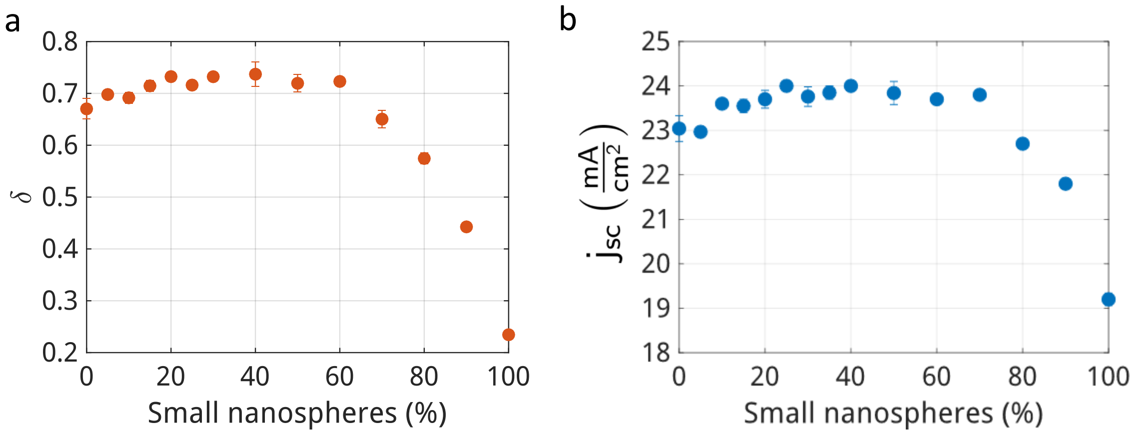

Figure 3.9: a) Plot of δ for increasing percentage of the perturbing small nanospheres. It is apparent that a plateau of δ is reached at around 20 % and maintained up to 60 %, before it quickly drops. b) Short-circuit current density for varying percentage of small perturbing nanospheres. The same tendency as for δ can be seen. In both diagrams, the small error bars indicate the standard deviation from at least three simulations with different height profiles for the same nanosphere occurrence fraction. Adapted from Ref. [108] (Copyright 2018 Optical Society of America).

$\vec{E}_{\text{ref}}(k_x^m, k_y^n)$ is the reflected electric field above the texture in Fourier space. To be precise, in principle there should also be a normalization factor $|\vec{E}_{\text{inc}}|^{-2}$ present in Eq. 3.5, but in the simulation, the incoming plane waves were already normalized to unity. Thus, δ is the portion of the incident light that is scattered into the target region in Fourier space.

δ is plotted in Fig. 3.9a for varying portion of perturbing nanospheres. Interestingly, the trend of the graph of δ shows the same dependency of the smaller nanospheres like the graph of ζ as shown in Fig 3.7b. For a hexagonally ordered nanospheres distribution comprising only the radius 170 nm, $\delta = 0.58$, while for a hexagonally ordered nanosphere distribution with radii 120 nm, $\delta = 0.13$. Both datapoints are not shown in the plot. The datapoints of δ for the mixtures of two nanospheres were obtained by averaging at least three simulations stemming from different height profiles with the same fraction of perturbing nanospheres. Similar to the PSD and RMS roughness, δ first increases. However, in contrast to the former two measures, a plateau is reached at around 30 % of small nanospheres, and δ is then approximately constant up to around 60 % perturbing nanospheres. The quantity δ defined in this way resembles the haze as introduced in Sec. 2.3, but as was already mentioned there, the haze does not allow to distinguish between large-angle and small-angle scattering distributions, therefore we do not use it here.

The insensitivity of the diffraction in the annulus to the exact portion of perturbing nanospheres suggests that the diffraction properties are still strongly influenced by the initial nanosphere size. The small nanospheres can be regarded as a perturbation up to high occurrence fractions, where removing or adding perturbing nanospheres does neither further broaden the diffraction spectrum nor heavily change the strength of the populated spatial frequencies.

3.2.4 Short-Circuit Current Density

We will now show results of full-wave FEM simulations to demonstrate that the approach using the diffraction efficiency indeed works as a good predictor for the suitability of a particular surface. We will calculate the absorptance in the crystalline silicon layer of the geometry depicted in Fig. 3.4 and from that the achievable short-circuit current density using Eq. 2.85. This serves, so to say, as the reference solution and the actual quantity we are mostly interested in to optimize. As before, the lateral size of our simulated domain spans at least 2.5 µm by 2.5 µm to ensure statistically stable results. The wavelength of the normal incident plane waves is chosen to be between 300 nm and 1200 nm in steps of 10 nm.

In Fig. 3.9b, we can see that the short-circuit current density follows the same trend as the quantity δ in the previously defined annulus region for a wavelength of 700 nm. This is a useful finding because it means that the computationally expensive full-wave simulations over the whole wavelength range and for the full stack can be replaced by a simulation at just one wavelength and without the need to consider the front interface. Especially, the diffraction efficiency turns out to be a better predictor than the PSD, at least for the height regime of the textures considered here. This, however, should not devaluate the PSD as a tool to get fast initial guidelines for finding promising nanosphere parameters.

If one uses a flat multilayer with the same geometrical settings (1 µm thick c-Si, 50 nm ITO, silver back reflector), the short-circuit current density is $j_{\mathrm{sc}} = 15.3\ \frac{\mathrm{mA}}{\mathrm{cm}^2}$. A silver back reflector that is textured with a hexagonal pattern with one nanosphere size of radius 170 nm, $j_{\mathrm{sc}} = 21.1\ \frac{\mathrm{mA}}{\mathrm{cm}^2}$. By allowing disorder while still retaining one size species, one can achieve a short-circuit current density of $23.0\ \frac{\mathrm{mA}}{\mathrm{cm}^2}$. This shows that by dropping the constraint of order, the short-circuit current density can already boosted by around 9 %. This can even be further improved by adding small perturbing nanospheres.

In our simulations, a maximum short-circuit current density of $j_{\mathrm{sc}} = 24.1\ \frac{\mathrm{mA}}{\mathrm{cm}^2}$ is obtained, which occurs at a portion of 60 % perturbing nanospheres. Compared to the flat surface, this is an improvement of 58 %, compared to the hexagonal ordered surface we gain 13.7 %, and compared to a surface with only one nanosphere size and allowed disorder, we still gain 4.8 %. These values for the short-circuit current density of the disordered textures have an uncertainty of around $0.1\ \frac{\mathrm{mA}}{\mathrm{cm}^2}$, showing that the results are statistically stable.

3.2.5 Summary of the Back Reflector Optimization Strategy

In this section, we have used the semi-analytical Power Spectral Density and full-wave diffraction results to circumvent the need to perform full-wave simulations over a large parameter space. With the PSD, we have chosen an initial nanosphere size to build the monolayer using the bottom-up approach. We then showed that for a very rough texture, the PSD is not a useful predictor for the short-circuit current density. Contrary, the diffraction efficiency in the target annulus shows the same trend as the short-circuit current density. We can therefore conclude that one can estimate the trend of the short-circuit current density by just calculating the diffraction response of a rough texture at a wavelength that is relevant for light-trapping.

3.3 Front Interface Analysis

Besides a good back reflector, optimal in-coupling of the sunlight into the solar cell is also of importance. Without any further structures, anti-reflection losses may significantly impair the generated short-circuit current density and hence the efficiency of a device. Therefore, we want to show in the following, how the bottom-up nanospheres approach may provide a useful possibility to strongly reduce the reflection losses at the front side of a solar cell. The results of this section have been published in Ref. [112].

3.3.1 Approach

There have already been published many strategies in literature, especially optical nanostructures with sub-wavelength features [100, 113–115]. These nanostructures shall mimic a graded-index transition with a smooth increase of the refractive index from air to the absorbing medium [116–119].

Most common anti-reflecting nanostructures are nanocylinders [120], nanorods [121], nanohemispheres [122], nanoneedles [123], or moth-eye structures [124]. A problem with these nanostructures is that they are usually fabricated using top-down methods, which are not readily scalable. One possible alternative is the usage of microstructures with larger feature sizes [125–127], or black silicon needles [128]. But due to their larger height, such structures are not usable for thin-film solar cells with a thickness of the absorbing material below 50 μm.

Not only the anti-reflection properties need to be optimized, but the structures should also provide large-angle forward scattering to enhance the light-path in the absorbing medium [129]. Furthermore, surface recombination can strongly impair solar cell efficiency and heavily depends on the geometry of the nanostructures [130]. Therefore, the task is to find an optimal roughness that accounts for these demands.

In the following, we will exploit the nanospheres-based bottom-up approach to obtain suitable textures for both reflection suppression and large-angle forward scattering. As in the previous section, we limit the analysis to two different nanosphere radii. This provides already enough freedom to achieve favorable anti-reflection properties. The nanospheres are distributed on the substrate as described in Sec. 3.1.3. However, in contrast to the optimization of the back reflector, here we use the negative of the resulting height profile. This ensures that the gaps that occur unavoidably between neighboring nanospheres translate into small needle-like features of the texture. The electrical properties of the textures are not analyzed, but we expect that the problem of surface recombination can be mitigated by new passivation techniques developed in the recent years [131].

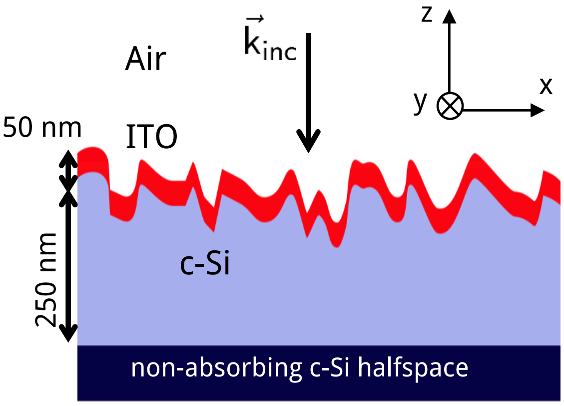

Figure 3.10: We analyze a multilayer system that consists of a c-Si absorber layer, textured with the rough height profile obtained from the bottom-up approach. Additionally, the c-Si is conformally coated with an ITO layer. For simulation purposes, the absorbing c-Si layer is truncated after 250 nm, and the semi-infinite half-space towards negative z-direction consists of non-absorbing c-Si. Adapted with permission from Ref. [112] (Copyright 2018 Wiley).

First, we will discuss to what extent the reflectance can be decreased with this kind of rough surfaces. After that, we will show the angle-insensitivity of the approach and the forward-scattering properties. Afterwards, we will use the Beer-Lambert law to calculate the absorptance in a several ten micrometer thick c-Si layer assuming a perfect flat back reflector.

3.3.2 Setup

We consider here a multilayer system consisting of a silicon absorber layer coated with a 50 nm thick ITO layer (see Fig. 3.10). The interface between c-Si and ITO will be patterned with the here analyzed rough texture retrieved with the placing algorithm that was described in Sec. 3.1.3. Because of the conformal nature of the ITO deposition, the ITO/air interface will have the same height profile. For computational purposes, in our simulations the c-Si absorber layer has a thickness of 250 nm, and is followed by a semi-infinite non-absorbing c-Si halfspace. This is done to enable incident plane waves from the bottom for the purpose of analyzing the ability of our textured interface to trap the light inside the absorber material.

As a start to find suitable nanosphere sizes, we seek to match the parameters of structures that have been shown in literature to provide good anti-reflection properties. These structures have periods in the range of 500 nm to 600 nm [118, 129]. This suggests that nanosphere radii in the range between 250 nm and 300 nm will work as useful starting values. However, just one nanosphere size would not yield sufficient surface roughness, as we have seen in the previous section in the discussion of the back reflector textures. To be able to obtain interfaces that comprise needle-like structures with steep slopes and small radius of curvature, we will add a second nanosphere size species with significantly smaller radii.

The generated height profiles have lateral feature sizes up to 300 nm (see Fig. 3.11a for an example texture). Using the same reasoning as in the previous section, we chose a simulation domain of at least 2 μm × 2 μm to ensure statistical stability of the scattering results.

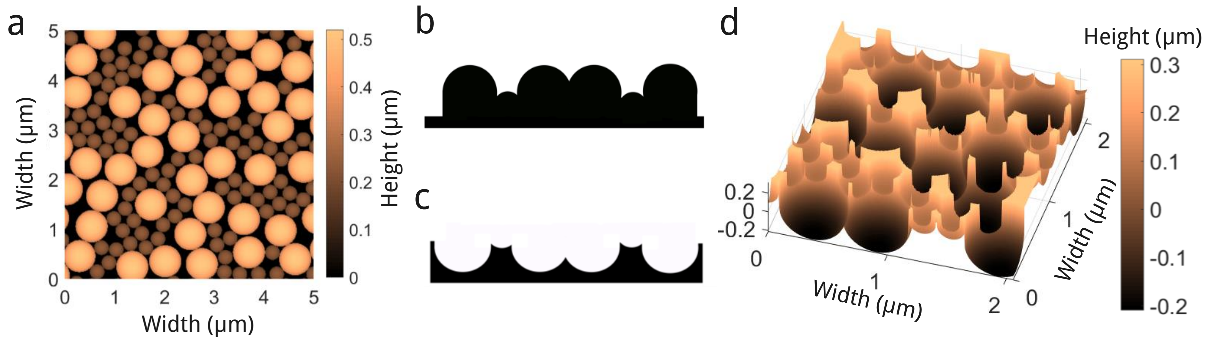

Figure 3.11: a) Example distribution of nanospheres forming a monolayer. The radii are 120 nm and 260 nm with an occurrence ratio of 70 %:30 %. b) Side view of the retrieved height profile. c) Inverted height profile comprising relatively sharp features. d) Tilted view of a final texture as used for the calculations. The mean height was set to zero. Reprinted with permission from Ref. [112] (Copyright 2018 Wiley).

3.3.3 Reflectance Results

To begin with, we simulated various configurations of nanospheres at a single wavelength (700 nm). We found that to achieve significantly corrugated textures, the occurrence fraction between the large and the small nanospheres should be around 30 %:70 %. This is in agreement with the results of the previous section, where we found that the largest RMS roughness is achieved for such occurrence fraction. We obtained reflectance values between 4.9 % and 6.5 %. We then proceeded to make simulations over the wavelength range for a few selected parameter choices. Here, only the wavelength range between 400 nm and 1200 nm is of interest for us.

Figure 3.12a shows the result for the reflectance at an air/ITO/c-Si interface for a few disordered configurations, and also a few reference structures. As can be seen, our textures are able to provide good anti-reflection properties, with reflectance values of 5 % on average. Especially for wavelengths above 500 nm, a large improvement in terms of reflection suppression could be achieved, considering that the flat interface has a reflectance that surpasses 20 % for wavelengths above 1000 nm. Notably is also the fairly constant average reflectance for the different nanosphere sizes and fractions. This means that the fabrication requirements are not very strict and provide tolerance in the nanosphere size and occurrence fraction.

We also show in Fig. 3.12a the reflectance spectra of a few reference textures which are discussed in literature with respect to anti-reflection properties. The red line shows the reflectance of hexagonally ordered nanospheres that are inverted and have a radius of 300 nm. The green line was calculated using random upright microstructure pyramids, where the height was chosen to be between 5 µm and 10 µm and the pyramids have a characteristic angle of 54.74° [132]. To calculate the reflectance, the raytracing tool OPAL 2 was employed [133]. The violet curve is the reflectance of a regular array of c-Si nanocylinders with diameter 250 nm, period 500 nm, and height 150 nm. Such nanocylinders have already been shown before to provide favorable anti-reflection properties [120]. In dashed black, the reflectance of a flat interface is shown. For all those textures, including the flat interface,

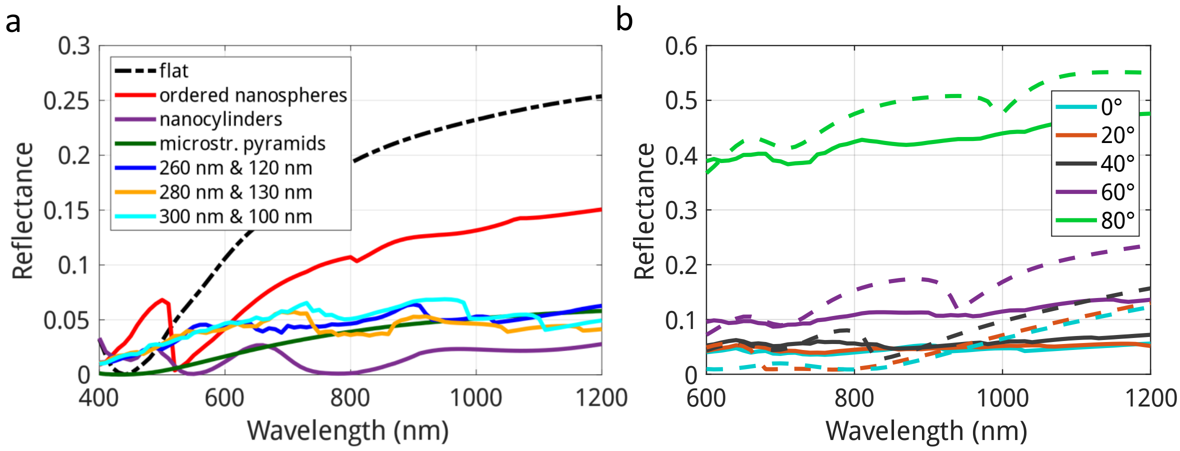

Figure 3.12: a) Plot of the spectrally calculated reflectance for some selected disordered textures and some reference structures, namely ordered inverted nanospheres, a periodic arrangement of nanocylinders, random pyramids with a height of a few micrometers, and a flat interface. b) The solid lines give the reflectance of the disordered texture with the nanosphere radii 260 nm and 120 nm and occurrence fraction 30 %:70 % for different angles of incidence. As a comparison, the dashed lines represent the reflectance of a texture consisting of periodically arranged nanocylinders for the same incoming angles. While the ordered nanocylinder array performs superior at small angles and short wavelengths, this changes when longer wavelengths and larger angles are considered; then, the disordered structure provides a lower reflectance. Adapted with permission from Ref. [112] (Copyright 2018 Wiley).

the same 50 nm thick conformal ITO anti-reflection coating is used. Hereby we ensure that comparability is given.

From the considered textures, the best anti-reflection properties are shown by the periodic nanocylinders. The microstructure pyramids and the disordered nanospheres are slightly worse. The hexagonally ordered nanospheres and the flat interface perform very inferior. However, due to the reciprocity, better light incoupling also means better light outcoupling of a device. So for a full picture, we will now investigate the light-trapping properties. Since we are here only concerned with textures that can be applied to thin-film devices with absorber thicknesses below 50 µm, we will not analyze the microstructure pyramids in the following.

A quantity that provides a useful answer to the question which of the different disordered textures can be regarded as most optimal for anti-reflection purposes, is the reflection loss-current density, defined by

$$j_{\text{loss}} = e \int_{400\text{ nm}}^{1200\text{ nm}} R(\lambda)\, \varphi(\lambda)\, \mathrm{d}\lambda\,. \tag{3.6}$$

Similar to the definition of the short-circuit current density in Eq. 2.85, it contains an integral over the wavelength with the solar irradiance spectrum $\varphi(\lambda)$ as integrand. But this time, we are not interested in the absorptance, but the reflectance, so $A(\lambda)$ was replaced by $R(\lambda)$. We find that among the considered mixtures, the lowest reflection loss-current density is achieved for the configuration with $r_1 = 260\,\text{nm}$ and $r_2 = 120\,\text{nm}$ (with occurrence fraction

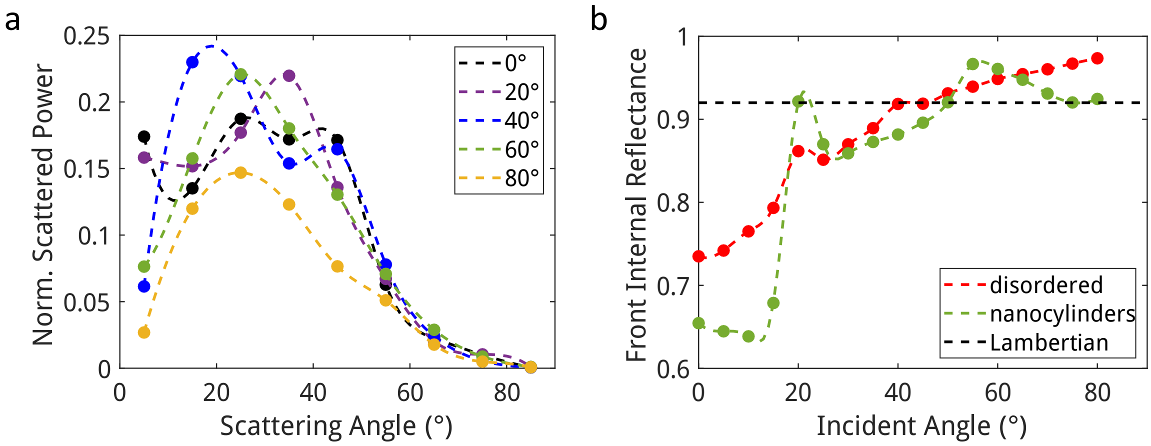

Figure 3.13: a) Angular distribution of power that is scattered in forward direction by the interface with the disordered texture. The angle of incidence was varied between 0° and 80° in steps of 20°, and the incoming wavelength was 900 nm. b) The graph shows the total reflectance occurring at the disordered c-Si/ITO/air interface for plane waves that are incoming from the negative z-direction at an oblique incidence. Again the vacuum wavelength was chosen to be 900 nm, and the steps of the incoming waves were 5° between 0° and 80°. TE and TM polarizations were simulated and the graph shows the average of both. The dashed line indicates the (angle- and polarization-independent) Lambertian reflectance. In a and b, the dots are the data points and the connecting dashed lines are a guide-to-the-eye which were obtained by spline interpolation. Adapted with permission from Ref. [112] (Copyright 2018 Wiley).

30 %:70 %), yielding $j_{\text{loss}} = 1.92\ \frac{\text{mA}}{\text{cm}^2}$. Consequently, this configuration will be used in the following for more specific reflection and light-trapping simulations. We want to mention again that the differences in the diverse nanosphere configurations are rather small and other size species do not show a significantly different behavior. To give a complete picture, the loss-current density of the nanocylinder array is $j_{\text{loss}}^{\text{cyl}} = 0.67\ \frac{\text{mA}}{\text{cm}^2}$ and that of the random microstructure pyramids is $j_{\text{loss}}^{\text{pyr}} = 1.42\ \frac{\text{mA}}{\text{cm}^2}$. As it will become clear in the next subsection, these lower loss-current densities are not decisive and other quantities, like the front internal reflectance and the reflectance under angled incidence, are required to determine which front texture is most beneficial in terms of light-trapping.

In a next step, the incidence angle dependency of the reflectance is explored. We made simulations for five angles between 0° and 80° in steps of 20° (see Fig. 3.12b), using the texture with $r_1 = 260\,\text{nm}$ and $r_2 = 120\,\text{nm}$ with occurrence fraction 30 %:70 % from the previous analysis. Simulations are done for TE and TM polarization; typically, disordered systems are not sensitive to the polarization, so we can just average the obtained reflectance spectra. To have a reference structure, we also calculated the TE and TM reflectance spectra for the periodic nanocylinders. The dashed line in Fig. 3.12b shows the reflectance for the nanocylinders as average of the two polarizations.

It turns out that the considered disordered texture is fairly angle-insensitive for the angular regime 0° to 60°, where throughout a reflectance below 14 % is achieved (cf. Fig. 3.12b). This behavior only breaks down at oblique angles larger than 60°, with reflectance values above 40 %. This can be explained by the significantly different scattering structure that is perceived by the light at such large angles compared to near normal incidence. Notably, the disordered texture offers a more stable reflection spectrum across the entire considered wavelength range than the periodic nanocylinders. Whereas at near normal incidence, the latter structure shows a lower reflectance, this changes for higher angles and longer wavelengths and the disordered texture then performs better.

We will now proceed to investigate the light-trapping potential of our disordered textures. In Fig. 3.13a, the power that is transmitted into the c-Si is plotted over the inclination angle, where 0° is the normal direction and 90° would be parallel to the interface. As incident angles, 0° to 80° in steps of 20° have been chosen. We focus on a wavelength of 900 nm, because at this wavelength, the extinction coefficient of c-Si is not strong enough to ensure complete absorption on a double pass through an absorber with a thickness of several micrometers, while the solar spectrum still provides enough incoming flux to make light-trapping desirable. For visualization in Fig. 3.13a, the scattering channels were collected in bins of 10° and all the contributions in one bin were summed up. It is apparent that the angle of forward scattering is to a large extent independent of the incoming angle. A peak occurs at a scattering angle of 30°, which could be potentially used to optimize back side textures to work best at a coupling angle of 30°. Last but not least, the total transmitted power decreases with increasing incoming angle, which can be expected based on the Fresnel equations (Eq. 2.18).

We also investigated the internal reflectance at the disordered c-Si/air interface after the light has undergone a double pass through the silicon layer. This was modelled by simulating the situation where plane waves are incident from the negative z-direction. For comparison, we also simulated the internal reflectance for an inverted hexagonal nanosphere array. Both results are shown in Fig. 3.13b. Also depicted is the Lambertian reflectance, which is constant for all angles, polarization-independent, and obtained from Eq. 2.92. This formula reads for the structure at hand

$$R_{\text{Lamb}} = 1 - \frac{1}{n_{\text{Si}}^2}\,, \tag{3.7}$$

with $n_{\text{Si}} = 3.62$ being the refractive index of c-Si at a wavelength of 900 nm.

As one can see in Fig. 3.13b, we find that the disordered texture scatters a large portion of the returning light back into the c-Si. Especially for angles that exceed 20°, both the disordered and the ordered texture show higher front internal reflectance than the Lambertian reference. This is however not the case for angles smaller than 20°, where the front internal reflectance is significantly lower than the Lambertian value. Although the disordered interface should provide more out-coupling channels into air as compared to the periodic nanocylinder grating, both front internal reflectances are very similar. This is notable and underpins the usability of such disordered interfaces for light-trapping. The high reflectance for all angles, but specifically for large incident angles, means that for further passes through the structure, the absorptance may increase further and will not be limited by the double-pass response.

3.3.4 Absorptance Results

In principle, it would be desirable to consider in the simulations an absorber layer with a thickness typically used in applications that involve absorption. However, to circumvent the need to perform computational very costly finite-element simulations with thicknesses in the order of several tens of μm, we extrapolate the obtained transmitted scattering orders to get an estimate for the expected absorption enhancement. The quantity that we calculate below is the sum of the extrapolated double-pass absorption computed for thicknesses 10 μm and 100 μm, and the absorption obtained in the 250 nm thick c-Si layer present in the FEM calculations. For the extrapolation, we use the Beer-Lambert formula given in Eq. 2.88, but adapted to account for discrete scattering channels and the presence of a back reflector:

$$A_{\text{ext}}(\lambda) = \sum_{ij} T_{ij}(\lambda) \left(1 - \mathrm{e}^{-2\alpha(\lambda)L/\cos\theta_{ij}}\right) . \tag{3.8}$$

The factor 2 in the exponent results from assuming two-pass absorption and a perfectly reflecting mirror at the backside of the solar cell. With T_{ij} we denote the transmittance that scatters into the c-Si layer into diffraction channel $k_x^{(i)}$, $k_y^{(j)}$ with an angle θ_{ij}. These values are retrieved from the FEM simulation. $\alpha(\lambda)$ is the wavelength-dependent absorption coefficient of c-Si. The factor $\frac{1}{\cos\theta_{ij}}$ is due to the different path lengths for the different scattering angles. Figures 3.14a and b show the expected total absorptance assuming absorber thicknesses of 10 μm and 100 μm, respectively. Also shown is the absorptance from Lambertian scattering as black dashed line. The blue dashed line is the absorptance of the periodic nanocylinder array, and the black solid curve is the absorptance of a flat air/ITO/c-Si interface. We obtained the Lambertian absorptance curve by assuming a cosine-dependence of the inclination angle for the transmitted field pattern, and then using the continuous Beer-Lambert formula to calculate the absorptance.

Using our disordered structure, one can see that the absorptance is slightly lower than the absorptance using the Lambertian texture. For the flat case, the absorptance is lower than unity in the wavelength regime up to 800 nm because of the significant reflection loss for light entering the silicon from the air side. If we would assume perfect transmission, the absorptance would come close to unity up to 800 nm.

A quantitative comparison of the absorptance performances can be drawn by calculating the short-circuit current densities using Eq. 2.85. The lower and upper integration limit for the wavelength are set to 500 nm and 1200 nm, respectively. We again assume that the internal quantum efficiency $\eta_{\text{int}} = 1$. In Tab. 3.1, we display the short-circuit current densities for the two evaluated thicknesses.

We observe a significant increase of the achievable short-circuit current density with our disordered texture in comparison to the flat case. Using the periodic nanocylinders, one may reach slightly larger short-circuit current densities, but at the expense of fabrication parameters that need to be precisely controlled. Also, the higher short-circuit current density of the nanocylinders is mainly a result of the lower reflection losses, which means that the light-trapping abilities of the disordered texture are superior. We hence expect that by tuning the nanosphere size distribution more, e. g. by allowing more than two nanosphere

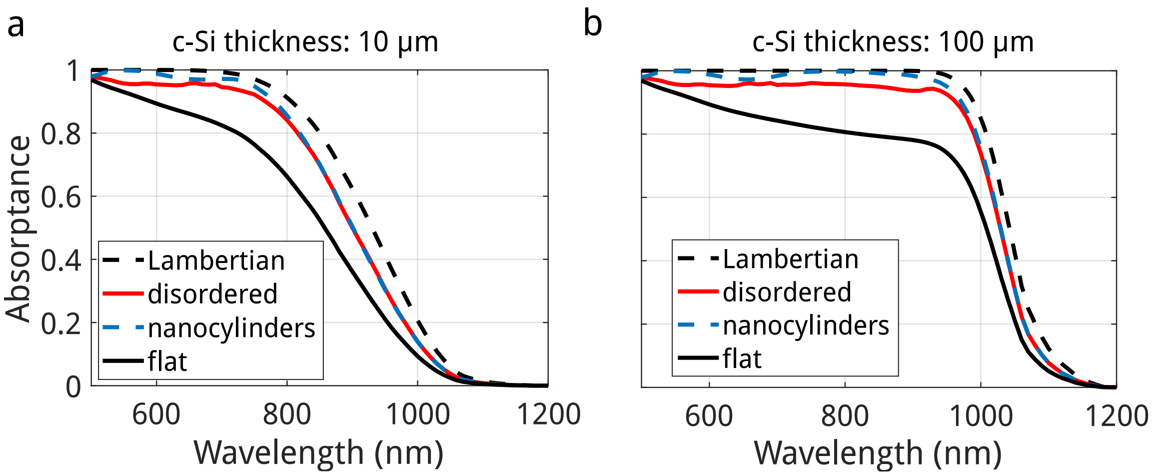

Figure 3.14: Displayed is the extrapolated absorptance for four different interfaces in the considered c-Si/ITO/air multilayer: Flat (black solid line), ordered nanocylinders (blue dashed line), disordered nanospheres (red solid line), and Lambertian (black dashed). The extrapolated absorptance was calculated for a) 10 µm and b) 100 µm thick c-Si. Adapted with permission from Ref. [112] (Copyright 2018 Wiley).

Table 3.1: Short-circuit current densities for four different types of possible front textures and two absorber thicknesses each. The values have been calculated from the absorptance spectra displayed in Fig. 3.14 by using Eq. 2.85. Reprinted with permission from Ref. [112] (Copyright 2018 Wiley).

	$j_{\mathrm{sc}}(10\,\mu\mathrm{m})\ \left(\frac{\mathrm{mA}}{\mathrm{cm}^2}\right)$	$j_{\mathrm{sc}}(100\,\mu\mathrm{m})\ \left(\frac{\mathrm{mA}}{\mathrm{cm}^2}\right)$
Lambertian	27.9	34.1
Period. Nanocylinders	25.8	32.5
Disordered	25.3	31.5
Flat	22.1	27.7

sizes to act as building blocks of the disordered texture, lower reflectance and thus higher absorptance can be achieved, maybe even close to the Lambertian result.

3.3.5 Summary of the Front Interface Analysis

In this section, we have exploited the bottom-up approach to design front interfaces for solar cells that decrease the reflection losses and also provide suitable light-trapping capabilities. It was found that disordered monolayers of nanospheres with two different size species are sufficient to largely decrease the reflectance for light entering the silicon absorber medium, while the internal reflectance is still high enough to achieve good light-trapping.

4 Emitters in Structured Environments

In the previous chapter, we have presented results of using disordered rough interfaces for solar cell devices. However, not only the light absorption, also the light emission is of interest in the context of various applications. To modify the emission properties of materials, the electromagnetic near-field has to be considered and engineered. The character of the near-field is in general very different compared to the far-field and there is also the necessity to include quantum effects in the analysis of the properties of emitters. In this sense, the near-field is more difficult to grasp, but the effects are also richer. In the present chapter, we will theoretically investigate the emission properties of electric and magnetic dipoles and discuss the effects in the presence of specifically tailored optical environments. Of interest is particularly the coupling of the emission to diffraction channels of gratings and guided modes in waveguides. The interplay of these mechanisms promises a paramount of interesting results.

First, we will continue the consideration of solar cells and analyze the second-order mechanism of photon recycling. Being ignored in typical numerical optimizations of solar cells, it can provide an important contribution to the overall efficiency. We numerically consider the radiative emission of photons as dipoles and calculate the reabsorptance and emission probabilities. Using these results, we will determine the additional contribution to the open-circuit voltage. The analysis is complemented by measurements done by collaborating partners from KIT.

We then go one step further and analyze the mechanisms that lead to the enhanced and directional emission of a dipole near a waveguide-grating structure. This was part of a collaboration with experimental partners at the Australian National University in Canberra. We found that the photoluminescence enhancement can be attributed to an increase of the local density of states (LDOS) at the pump wavelength and at the emission wavelength, respectively. The LDOS increase was caused by coupling to waveguide modes, which also shaped the strongly directional emission pattern as a consequence of the waveguide dispersion relations.

To extend these considerations even further, we then considered simultaneously electric and magnetic dipole emission. In this project, which has been carried out with an experimental group at the Friedrich-Schiller-Universität Jena, spectrally close electric and magnetic dipole transitions have been excited in the vicinity of a silicon nanodisk grating. It was found that with suitable nanodisk radii, the magnetic dipole transition can be stronger enhanced than the electric dipole transition. The measurements have been accompanied with simulations on our side.

4.1 Photon Recycling in Perovskite Solar Cells

As a higher order effect, photon recycling is typically ignored in the analysis of nanotextures for solar cells. However, particularly for very high-efficiency solar cells it cannot be ignored anymore and indeed is usually considered as the key for achieving new efficiency records. We have described the physical origins and general treatment of photon recycling in Sec. 2.6.3. Here, we will offer a comprehensive study regarding the quantitative impact of photon recycling in the highly relevant case of nanotextured perovskite solar cells. The insights of this work are particularly important when discussing materials with a very high radiative recombination rate. The experimentally available materials, unfortunately, are not yet sufficiently superior such that the analysis at the moment does not yet consider an entire solar cell. For simplicity, a suitably chosen multilayer structure is considered that resembles, nevertheless, many aspects of the solar cells that require attention in the near-future. A full solar cell stack is studied in simulation. The supporting experimental work was done in the group of Ulrich Paetzold at the Institute of Microstructure Technology (IMT)/Light Technology Institute (LTI) and in the group of Martin Wegener at the Institute of Applied Physics (APH), both at KIT. The results of this section have been reported in Ref. [134].

4.1.1 Motivation

So far, we have only studied silicon as absorber material for solar cells. This was justified by the dominant and prevalent role silicon plays in the solar cell market. However, strong research is done to explore alternative materials. One very promising material class, not only for solar cells but also for light-emitting devices [135–137], are the organo metal-halide perovskites. It has been demonstrated that the fabrication of thin-film perovskite layers can be achieved with low-cost precursor materials and fabrication processes [138]. It can even be directly printed. Perovskites are typically considered as having a direct bandgap, which renders them particularly useful for solar cell applications [139]. Even more intriguing is the fact that the bandgap of perovskites depends on its structure and can, therefore, be tailored by compositional engineering. This opens the possibility to use them in a broad spectral range for tandem solar cells and LEDs [140–143].

In contrast to other solar cell absorber materials, the radiative recombination in perovskite is an important process, especially for high quality perovskite thin-films [4]. Photon recycling may therefore yield a significant contribution to the overall efficiency. Particularly, the open-circuit voltage V_{oc} increases when the reabsorption of radiatively emitted photons is considered. A direct experimental observation of photon recycling is difficult and has not yet been achieved, but calculations for basic planar multilayers have already demonstrated that the mechanism of photon recycling is significant for currently achievable nonradiative lifetimes and therefore sufficiently small nonradiative decay rates [81, 82, 144]. As textured interfaces are an integral part of many solar cells, the impact of such textured interfaces on the photon recycling needs to be studied.

Quantifying the open-circuit voltage gain due to photon recycling faces several challenges: Numerically, one has to consider wave-optical effects in a system that consists of a single

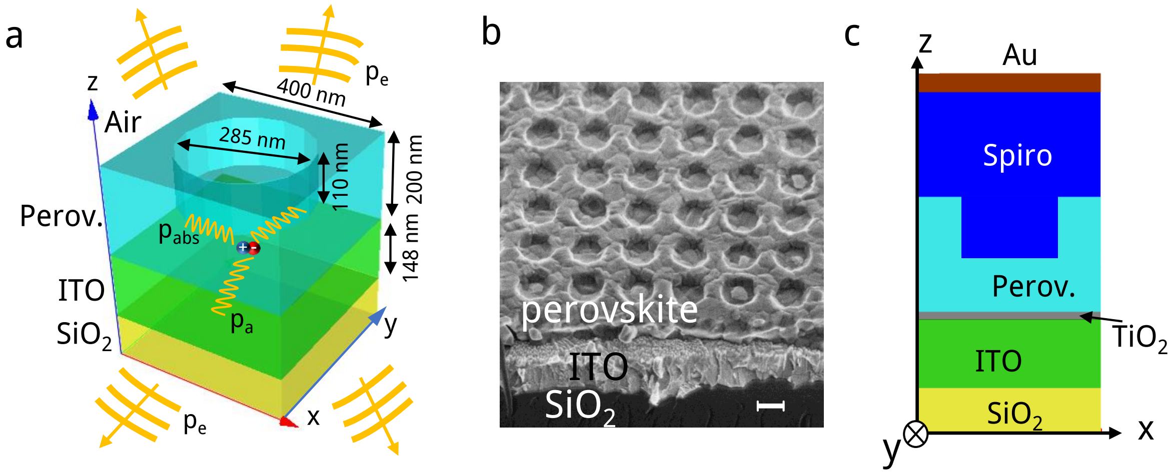

Figure 4.1: a) Simplified multilayer stack considered in the simulations: A glass substrate with ITO and perovskite, which is textured with cylindrical holes. Above the perovskite, we assume air. Also shown are the probabilities for radiative emission (p_e), parasitic absorption (p_a), and absorption in perovskite (p_{abs}). b) SEM micrograph of the imprinted multilayer taken by Raphael Schmager at IMT/LTI. The scale bar denotes 200 nm and the micrograph was taken under an angle of 45°. c) Two-dimensional cross section of the complete solar cell stack. Compared to the stack in a), an electron-transport layer (TiO_2) with a thickness of 20 nm, a hole-transport layer (Spiro-OMeTAD, 230 nm), and a gold back reflector have been added. Reprinted from Ref. [134], with the permission of AIP Publishing.

dipole emitter within a periodic photonic environment. When it comes to measurements, one needs to account for both the fraction of power that is reabsorbed in the absorber material and the power that radiatively escapes from the device, respectively. Both measurements are very difficult. Despite these challenges, there is the desire to quantify the additional voltage gain thanks to the photon recycling to reach a full understanding of the expected efficiency of a nanostructured solar cell. In the following, we will present a quantitative analysis of the impact of photon recycling for the case of a nanotextured thin-film perovskite multilayer that was optimized for light-trapping purposes [83–85].

4.1.2 Approach

For our calculations, we consider a simplified multilayer structure as shown in Fig. 4.1a: A glass substrate, followed by a 148 nm thick ITO layer, and an imprinted perovskite layer with different thicknesses. In Fig. 4.1a, a thickness of 200 nm is indicated. The texture is a regular square grating consisting of cylindrical holes with hole diameter 285 nm, hole depth 110 nm, and period 400 nm. These parameters have been shown to yield an optimized performance in terms of light-trapping and absorption [85], and similar textures were also reported to increase the photoluminescence of perovskite cells [145]. An SEM micrograph of the cross section of a fabricated sample is shown in Fig. 4.1b.

The reason to use such a simplified layer stack is to be able to excite it with a laser and measure the photoluminescence spectrum from opposite sides of the sample. This was

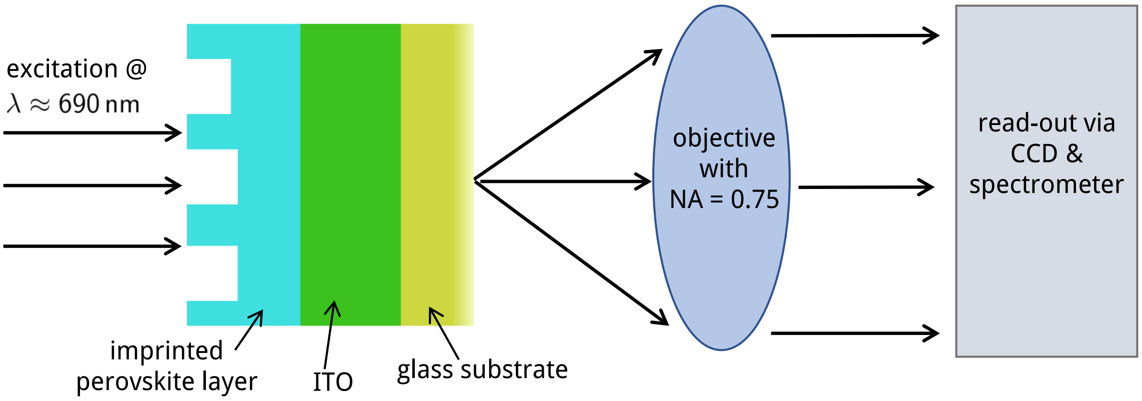

Figure 4.2: Setup of the back-focal plane measurements: The sample is excited from the textured side at a wavelength of 690 nm. The photoluminescence is then measured on the substrate side using an objective with a numerical aperture of 0.75 and a CCD camera. Reprinted from Ref. [134], with the permission of AIP Publishing.

possible with an already available experimental setup. Additionally, we will also consider the entire solar cell stack as shown in Fig. 4.1c. Here, additional layers are taken into account: Between the ITO and the perovskite, a 20 nm thick TiO_2 layer has been inserted, and above the perovskite, a 230 nm thick hole transport layer (Spiro-OMeTAD) and a gold mirror is added. The parameters of the grating and the ITO thickness are the same for both multilayers.

While considering the simplified multilayer structure, we will determine the angular spectrum of the radiatively emitted photons, both numerically and experimentally. In the calculations, we model the radiative recombination and photon emission with electric dipole emitters. After verifying that our calculations reproduce the measurements sufficiently accurate, we calculate the additional contribution to the open-circuit voltage due to photon recycling. For reference, we will also consider two additional perovskite/air interfaces: A planar interface, and an interface with ideal Lambertian scattering properties. Using these two interface types, we also calculate the absorptance in the perovskite and from that the open-circuit voltage enhancement. These two interface types are extreme cases and serve as upper and lower bounds of the additional open-circuit voltage contributions that can be expected due to photon recycling.

4.1.3 Calculations and Measurements

Experimental Setup

The measurement setup is schematically illustrated in Fig. 4.2. The sample is excited with a pulsed laser at a wavelength of 690 nm from the grating side. An objective lens with a numerical aperture of 0.75 is used to parallelize the emitted photoluminescence. A long-pass filter (not shown) filters out the wavelength of the laser beam. Afterwards, the back-focal plane of the objective lens is imaged onto a CCD camera using an exposure time of 1 second. This setup enables to obtain the photoluminescence spectrum in reciprocal space. The samples have been fabricated by Raphael Schmager at IMT/LTI, whereas the angular spectrum measurements were done by Andreas Wickberg at APH. For further details of the sample fabrication and measurements, we refer to Refs. [134] and [146].

Numerical Analysis

The numerical analysis consists of the following steps: First, the reabsorptance in the presence of planar and Lambertian textured interfaces is considered to compare it to the nanopatterned case. Afterwards, we compute the reabsorptance due to the nanotextured interfaces. The emission of radiatively emitted photons is modelled using electric dipole emitters that radiate at the wavelength corresponding to the photoluminescence peak of perovskite. In a last step, we calculate the open-circuit voltage enhancement from the obtained reabsorptance values.

To determine the spectral emission peak of the used perovskite, we performed spectrally-resolved measurements of the photoluminescence. In Fig. 4.3a, the emission intensity is plotted over the wavelength. We find that the emission peak is centered at 780 nm. Hence, we use this wavelength in our calculations. Furthermore, the complex refractive indices used in the simulations are $n_{\mathrm{ITO}} = 1.62 + 0.02\mathrm{i}$, $n_{\mathrm{Perov}} = 2.58 + 0.04\mathrm{i}$, $n_{\mathrm{Au}} = 0.15 + 4.74\mathrm{i}$, $n_{\mathrm{TiO_2}} = 2.12$, $n_{\mathrm{Spiro}} = 1.66 + 0.002\mathrm{i}$, and $n_{\mathrm{SiO_2}} = 1.45$. They have been taken from Ref. [147] and correspond to the emission wavelength.

Considering the Lambertian interface, the reabsorptance due to an emitter inside the perovskite layer can be derived analytically. For this purpose, the perovskite is assumed to be planar at the ITO side and Lambertian textured at the air side (see Fig. 4.3b). We neglect the glass substrate and assume the ITO to fill out the entire halfspace in negative z-direction. As described in Sec. 2.5.3, the Lambertian texture is characterized by a $\cos\theta$ reflectance and transmittance pattern upon irradiation.

We separately derive the reabsorptance for different dipole configurations. These configurations are given by the vectorial orientation (x, y, or z) and the vertical position of the dipole emitters inside the perovskite layer. The vertical positions are chosen equidistant. The reabsorption is calculated by assuming the validity of ray-optical equations that describe the traversal of the electric field through the perovskite layer. As initial dipole radiation patterns, we assume a $\cos^2\theta$ for the x- and y-oriented dipoles, and a $\sin^2\theta$ distribution for the z-oriented dipole. These patterns only remain until the first reflection at one of the interfaces. After reflection at the Lambertian texture, a $\cos\theta$ distribution emanates due to randomization, while the reflection at the perovskite/ITO interface provides a radiation pattern that only contains those rays that are outside of the escape cone.

To calculate the absorptance, we use an approach introduced in Ref. [61]. The absorption due to multiple traversals of the light through the perovskite layer is modelled as an attenuation of a propagating incoherent light ray in a slab waveguide with non-zero absorption

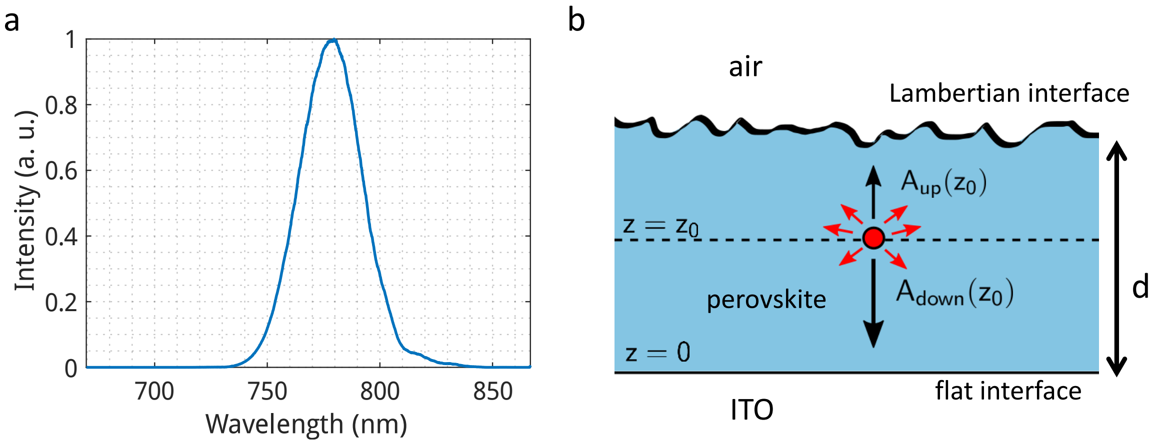

Figure 4.3: a) Measured spectrally resolved emission of the perovskite material that was used for the angular spectrum measurements. The peak is at 780 nm. b) Sketch of the geometry and the parameters that were used for the derivation of the Lambertian reabsorptance. The additional glass substrate was neglected and hence the ITO was assumed as semi-infinite. Adapted from Ref. [134], with the permission of AIP Publishing.

coefficient. Using this terminology, for radiation that initially travels towards the positive z-direction, the reabsorptance A_{up} for a dipole at position $z = z_0$ can be calculated as

$$A_{\mathrm{up}}(z_0) = 1 - \frac{T_{\mathrm{d}}(z_0)(1 - R^{\mathrm{f}}) + T_{\mathrm{d}}(z_0)R^{\mathrm{f}}T^{-}(1 - R^{\mathrm{b}})}{1 - R^{\mathrm{f}}T^{-}T^{+}R^{\mathrm{b}}} . \tag{4.1}$$

Similarly, the reabsorptance A_{down} of radiation that initially propagates towards the negative z-direction is

$$A_{\mathrm{down}}(z_0) = 1 - T_{\mathrm{d}}(z_0)(1 - R_{\mathrm{d}}^{\mathrm{b}}) - \frac{T_{\mathrm{d}}(z_0)R_{\mathrm{d}}^{\mathrm{b}}T_{\mathrm{d}}^{+}(1 - R^{\mathrm{f}}) + T_{\mathrm{d}}(z_0)R_{\mathrm{d}}^{\mathrm{b}}T_{\mathrm{d}}^{+}R^{\mathrm{f}}T^{-}(1 - R^{\mathrm{b}})}{1 - R^{\mathrm{f}}T^{-}T^{+}R^{\mathrm{b}}} . \tag{4.2}$$

The total absorptance is $A_{\mathrm{tot}}(z_0) = \frac{1}{2}(A_{\mathrm{up}}(z_0) + A_{\mathrm{down}}(z_0))$.

R^{f} is the reflectance at the Lambertian front interface (cf. Eq. 2.92) and R^{b} is the reflectance at the back interface for light with Lambertian distribution $\cos\theta$. Similarly, T^{-} (T^{+}) is the transmittance for light with $\cos\theta$ distribution travelling to negative (positive) z-direction. These quantities are explicitly given in Ref. [148] and are valid as long as the extinction coefficient is small compared to the real part of the refractive index. The remaining quantities $R_{\mathrm{d}}^{\mathrm{b}}$, T_{d}, and T_{d}^{+} depend on the dipole pattern and are detailed in Ref. [134].

The reabsorption in the presence of the planar interface is simulated using FEM. The unit cell consists of a stack comprising a semi-infinite glass half-space, an ITO layer (148 nm), the perovskite layer (different thicknesses), and a semi-infinite air half-space. In x- and y-direction, the width of the unit cell is chosen to be identical to the period in case of the nanotextured interface (400 nm). The unit cell is surrounded with transparent (PML) boundaries in all directions, which yields an environment with the multilayer being extended infinitely along x and y. The radiative recombination and subsequent emission of photons is numerically modelled with dipole emitters inside the perovskite. Each dipole emitter is enclosed in a small cylindrical cavity of non-absorbing perovskite with a height and diameter of 40 nm. Such an enclosure needs to be considered in numerical calculations, since the Green's function of an emitter that is located within an absorbing medium cannot be calculated and a minimal distance to the absorber medium has to be introduced artificially [149, 150].

We place dipole emitters at three different positions inside the perovskite layer (25 nm away from the perovskite/air and perovskite/ITO interface, respectively, and in the center). For each position, we simulated the three dipole polarizations in x-, y-, and z-direction. In our case, the total absorptance in the perovskite layer is then the power that is absorbed in the perovskite layer, plus the power flux that is transmitted from the perovskite into the PMLs. With the latter, we account for the fact that a large portion of the power is contained in waveguide modes that have a large in-plane propagation constant and decay only slowly. In a last step, the absorptance is averaged over the positions and polarizations.

For the nanotextured case (both for the simplified and complete multilayer stack), we make use of the inverse Floquet method described in Sec. 2.3.3. Only with this method, we will obtain an angular spectrum that approximates the spectrum of an isolated dipole in the periodic environment. We use a discretization for the Bloch vector of 64 values along both k_x- and k_y-axis. The calculations are performed for the perovskite thicknesses 200 nm and 250 nm. Hereby we account for the varying perovskite thickness in the fabricated samples. The glass substrate is modelled as semi-infinite to account for the several millimeters thick substrate in the measurements. In case of the full stack, the gold layer has a thickness of 40 nm, and is followed by a semi-infinite halfspace of gold where the extinction coefficient was set to zero.

To take into account the spatially varying LDOS in the perovskite layer, we individually calculate the emission response of dipoles that are placed equidistantly along the z-axis in distances of 10 nm. Furthermore, for each dipole, all three orientations along x, y, and z are considered. At a given z-position, four different horizontal positions are calculated: Edge, corner, half-diagonal, center (only in the bulk region), and close to the hole (only in the grating region). As in the case for the planar interface, the dipole emitters are enclosed in a small cavity. Although each individual simulation only takes a few minutes, the fact that we need 64×64 simulations for each z-layer considerably affects the time to obtain all results. Therefore, to be at least able to simulate all four positions within one simulation iteration, we do not use a cylindrical enclosure, but a slab with height 40 nm and width corresponding to the unit cell size.

The four different horizontal dipole positions were chosen to be in one of the four quadrants of the unit cell. This means that the resulting total angular spectrum is asymmetric. By rotating the spectrum according to the underlying symmetry of the lattice, we can obtain a rotationally symmetric angular spectrum. Finally, we average over the three different dipole orientations and various horizontal and vertical positions. The spectrum that needs to be compared to the measurements is the one to the negative z-direction. Since the FEM simulations yield the spectrum in glass, in a last step we analytically calculated the transmission of the field components through the glass/air interface using the Fresnel equations given in Eq. 2.18.

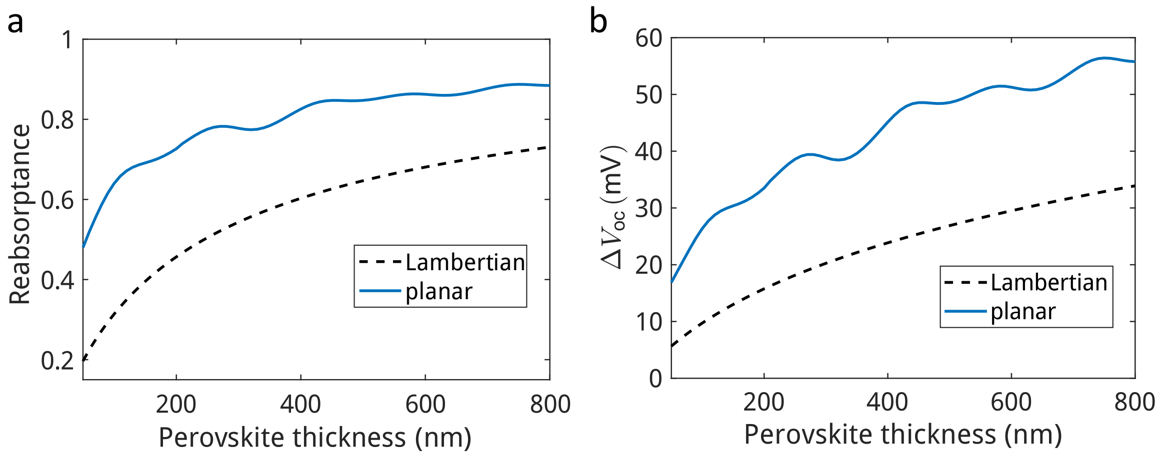

Figure 4.4: a) Reabsorptance in perovskite of the power emitted from the dipole for both, a planar and a Lambertian perovskite/air interface, respectively, as a function of the perovskite thickness. b) Open-circuit voltage contribution due to the reabsorptance plotted in (a), calculated with Eq. 2.95. Reprinted from Ref. [134], with the permission of AIP Publishing.

To calculate the additional gain in open-circuit voltage due to photon recycling, $\Delta V_{\mathrm{oc}}^{\mathrm{PR}}$, we use Eq. 2.95 that was introduced in Sec. 2.6.3. In the following, we will assume $T = 300$ K and only radiative recombination processes, i. e. from Eq. 2.94 we have $\eta_{\mathrm{lum}} = 1$. Also, the term $1 - p_{\mathrm{e}} - p_{\mathrm{a}}$ is nothing but the reabsorption probability p_{abs} in the perovskite layer, which is obtained from the simulations.

4.1.4 Results

We first calculated the reabsorptance in the perovskite layer assuming a planar and a Lambertian perovskite/air interface, respectively, as described in the previous section. Due to the lack of outcoupling channels in the case of the planar interface and hence total internal reflection, the light is largely trapped inside the perovskite. Contrary, the Lambertian texture has many out-coupling channels, so that the portion of trapped light is smaller. Thus, the reabsorptance is significantly higher for the planar interface than for the Lambertian texture, as shown in Fig. 4.4a. We can also identify small spectral oscillations in the reabsorptance for the planar interface. They are due to Fabry-Perot resonances in the perovskite thin-film [81]. For a single position and dipole orientation, they are even more pronounced, but after averaging over the positions and the orientations, the oscillations decrease.

The plot of the open-circuit voltage enhancement $\Delta V_{\mathrm{oc}}^{\mathrm{PR}}$ as shown in Fig. 4.4b was obtained by using Eq. 2.95 and the values for reabsorptance from Fig. 4.4a. Consequently, the overall trend in $\Delta V_{\mathrm{oc}}^{\mathrm{PR}}$ is the same as for the reabsorptance: The planar interface provides a higher $\Delta V_{\mathrm{oc}}^{\mathrm{PR}}$ than the Lambertian interface. However, in this discussion one should keep in mind that the reabsorptance after radiative recombination is just a minor part of the overall absorptance of a solar cell device, and the Lambertian texture will still be the better interface in terms of trapping light that impinges from outside. We can expect that a nanostructure that is optimized for light-trapping will yield reabsorptance and $\Delta V_{\mathrm{oc}}^{\mathrm{PR}}$ values somewhere

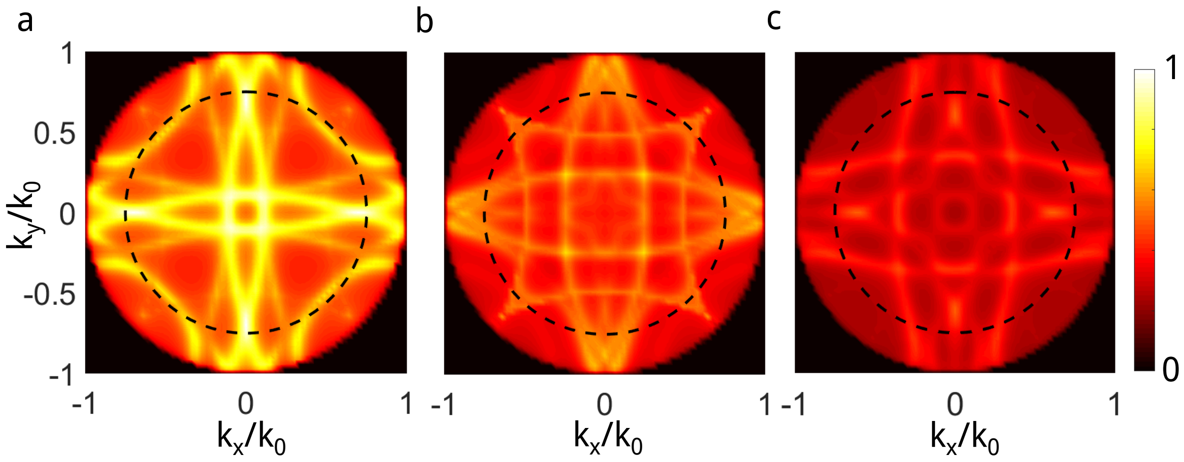

Figure 4.5: Plots of the numerically obtained angular spectra of the emission from structured perovskite layers. a) Grating period 400 nm, perovskite thickness 200 nm. b) Grating period 400 nm, perovskite thickness 250 nm. c) Grating period 450 nm, perovskite thickness 200 nm. In all three plots, the dashed line denotes the numerical aperture (0.75) as used in the measurements and the wavevector axes are normalized to the wavenumber in vacuum. Reprinted from Ref. [134], with the permission of AIP Publishing.

between the planar and the Lambertian interface. In the following, we will quantify this for a perovskite layer that is patterned with a two-dimensional periodic grating.

We performed simulations of the grating structure with different parameters of the perovskite thickness and unit cell period. The grating depth was kept constant at 110 nm. The resulting angular spectra are shown in Fig. 4.5. The spectrum of Fig. 4.5a was obtained with a period of 400 nm and a perovskite thickness of 200 nm. In Fig. 4.5b, the period was 400 nm and the perovskite thickness 250 nm. Finally, in Fig. 4.5c, we used a period of 450 nm and again a perovskite thickness of 200 nm. The black dashed line pertains to a numerical aperture of 0.75. This numerical aperture is important as it corresponds to the numerical aperture which was used in the measurements.

The three plots are normalized to the same scale, which shows that the total radiated power decreases with a larger thickness of the perovskite layer and a larger period. This can be attributed to an increase of the total reabsorbed power. Furthermore, one can observe that the emission is highly directional. Both the thickness increase and the period enlargement also lead to a shift of the high-intensity features to larger wavevectors. Additionally, in Fig. 4.5a a large intensity is obtained close to the largest propagating wavevector, indicating that the angles in which light is scattered can be quite large.

The large intensity features are intimately linked to waveguide modes that are sustained by the thin-film perovskite layer. To shed more light on this issue, we performed eigenmode calculations of the multilayer with only planar interfaces. From this, we obtained the effective refractive indices n_{eff} of the possible modes. These are plotted in Fig. 4.6a as a function of the thickness of the perovskite layer. At a thickness of 200 nm, we find three available modes: TE_0, TM_0, and TE_1. However, the latter one is hardly there and will be ignored in the following. Cross sections of the spatially resolved field intensities of the two

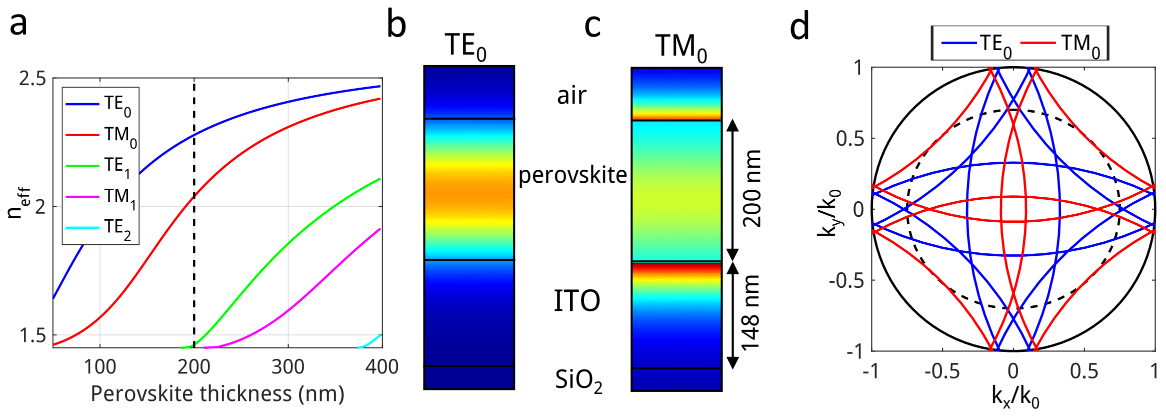

Figure 4.6: a) Plot of the effective refractive indices as a function of the perovskite thickness for the available modes in the simplified multilayer of Fig. 4.1a. b) and c) Field intensity cross sections for the simplified multilayer with a perovskite thickness of 200 nm for the two fundamental modes. d) First Brillouin zone showing the dispersion curves for the two fundamental modes TE$_0$ and TM$_0$ for a perovskite thickness 200 nm and a period of 400 nm. The dashed circle denotes the numerical aperture (0.75) and the solid line indicates the light cone, where the normalization is the vacuum wavenumber. Reprinted from Ref. [134], with the permission of AIP Publishing.

fundamental modes TE$_0$ and TM$_0$ are depicted in Fig. 4.6b and c for the planar multilayer. Along the z-axis, the intensity shows strong variations; for the TE$_0$, the largest intensity is quite in the center of the perovskite layer, while for the TM$_0$ mode, we encounter large intensity leaking out into the ITO, which then causes relatively large parasitic absorption.

To account for the periodicity of the imprinted grating, we assume for the moment that the effective refractive indices of the eigenmodes of the planar case do not change when the nanotextured interface is considered. This corresponds to the case of Fig. 2.10b. We look at the dispersion relations of the resulting guided modes in the first Brillouin zone and assume a period of 400 nm in both x- and y-direction, a perovskite thickness of 200 nm, and a vacuum wavelength of 780 nm. In Fig. 4.6d, the radii of the circles are given by the effective refractive indices of the two fundamental modes: $n_{\mathrm{TE}_0} = 2.28$ (blue lines) and $n_{\mathrm{TM}_0} = 2.04$ (red lines) displaced by an integer multiple of the reciprocal lattice vector. The graph was obtained by using Eq. 2.83 and normalizing all values by the vacuum wavenumber. The black dashed line indicates the light line in air.

From Fig. 4.6d, we can conclude that the TE$_0$ and TM$_0$ modes have the strongest effect on the emission patterns shown in Fig. 4.5. A clear distinction of the TE$_0$ and TM$_0$ dispersion curves is not possible. We attribute this to the presence of the grating, that perturbs the results obtained with the planar eigenmode calculations. For example, the TM$_0$ mode has a large fraction of its modal amplitude confined at the perovskite/air interface, i. e. in the vicinity of the grating, and distortions of the eigenmodes can be expected. In Fig. 4.5a, the intersection of the TE$_0$ and TM$_0$ dispersion lines that result from the periodicity in x- and in y-direction occurs at normalized in-plane wavenumbers of around 0.15. This intersection shifts to larger wavenumbers when the perovskite thickness is increased (Fig. 4.5b), in agreement with Fig. 4.6a, where the effective indices increase with increasing perovskite thickness. A similar shifting to larger emission angles can also be identified for a larger period (Fig. 4.5c), which

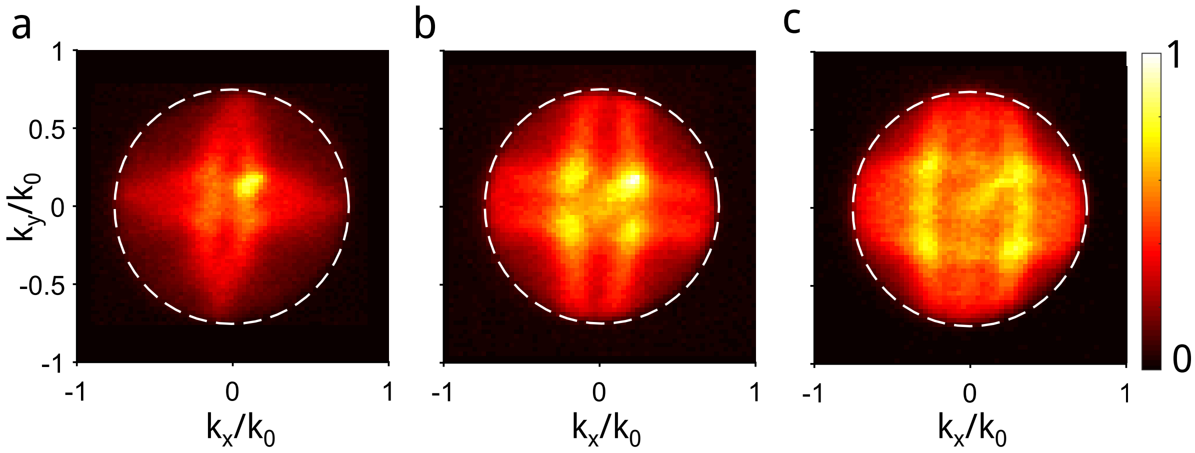

Figure 4.7: Angular intensity spectra obtained from measurements by Andreas Wickberg. The grating periods are a) 410 nm, b) 430 nm, and c) 460 nm. Confirming the numerical results, we notice that the features of large intensity shift to larger wavevectors if the period is increased. The numerical aperture of 0.75 is marked by the dashed circle and the axes are normalized to the wavenumber in vacuum. Reprinted from Ref. [134], with the permission of AIP Publishing.

is due to the smaller grating vector that leads to a smaller translation of the dispersion circles according to Eq. 2.83.

From comparing the calculated emission spectra with the dispersion calculations for the flat multilayer, we can conclude that the grating acts only as a small perturbation to the eigenmodes. This is surprising, since the cylindrical holes encompass around half of the total thickness of the perovskite layer.

We now turn to the back-focal plane angular spectrum measurements of fabricated devices. Results of the photoluminescent emitted power for three different samples are shown in Fig. 4.7: For the three plots, the periods are between 410 nm and 460 nm, with perovskite bulk thicknesses between 90 nm and 200 nm. The hole depth is for all three samples the same and approximately 110 nm. The same intensity peaks can be identified when compared to the measured angular distribution, with four peaks symmetrically located around the normal direction. We also see the TE_0 and TM_0 dispersion lines that are shifted by one grating vector in positive and negative x- and y-direction. The other minor features that can be seen in the calculated spectra are not present or not sufficiently resolved in the measurements, which might be because of insufficient resolution of the detector. We also note that the non-absorbing artificial layer as considered in the calculations might introduce additional deviations. Despite these deviations, the agreement between measurements and calculations is still sufficiently good such that we can be confident to reproduce the main physics of the system with our calculations.

Therefore, we now calculate the additional contribution to the open-circuit voltage resulting from photon recycling. For comparison, at a thickness of 200 nm the values for the planar and Lambertian texture are $\Delta V_{\mathrm{oc}}^{\mathrm{PR}} = 33.5$ mV and $\Delta V_{\mathrm{oc}}^{\mathrm{PR}} = 15.8$ mV, respectively (cf. Fig. 4.4b). The values that we obtain from the nanotextured grating are between these two extreme cases: For the geometry with perovskite thickness of 250 nm and period 400 nm (Fig. 4.5b), our calculations yield $p_{\mathrm{abs}} = 0.61$ for the absorptance in perovskite. This in turn leads to $\Delta V_{\mathrm{oc}}^{\mathrm{PR}} = 24.3$ mV. This compares to $p_{\mathrm{abs}} = 0.51$ and $\Delta V_{\mathrm{oc}}^{\mathrm{PR}} = 18.4$ mV for the geometry with period 400 nm and thickness 200 nm (Fig. 4.5a). Finally, $p_{\mathrm{abs}} = 0.55$ and $\Delta V_{\mathrm{oc}}^{\mathrm{PR}} = 20.8$ mV for the period of 450 nm and the thickness of 200 nm (Fig. 4.5c).

The complete solar cell stack as depicted in Fig. 4.1c with the perovskite thickness of 200 nm yields $\Delta V_{\mathrm{oc}}^{\mathrm{PR}} = 24.0\,\mathrm{mV}$, and the complete stack with perovskite thickness of 250 nm yields $\Delta V_{\mathrm{oc}}^{\mathrm{PR}} = 28.3\,\mathrm{mV}$. Due to the gold reflector, these values are higher than for the simplified multilayer. On the other hand, the additional layers also increase parasitic absorption, so the difference to the simplified multilayer is not very large. The obtained results for $\Delta V_{\mathrm{oc}}^{\mathrm{PR}}$ serve as a suitable guideline what can be expected in experiments using such nanostructured thin-film perovskites.

Since the short-circuit current density j_{sc} is the quantity that has to be optimized at the end of the day, we calculated it for the simplified multilayer using normal incident plane waves impinging on the multilayer from the negative z-direction (planar side). We apply Eq. 2.85 in the relevant wavelength regime between 330 nm and 820 nm and calculate the absorption in steps of 5 nm. We aim to compare the nanotextured structure with perovskite thickness 200 nm and period 400 nm to a planar multilayer. Since the absorptance is influenced by the perovskite volume, we adapt the perovskite thickness of the planar multilayer such that the total volume equals the perovskite volume with the imprinted nanotexture (i. e. the perovskite thickness was chosen to be 156 nm in the planar case).

We obtain $j_{\mathrm{sc}}^{\mathrm{plan}} = 16.3\,\frac{\mathrm{mA}}{\mathrm{cm}}$ for the planar multilayer, and $j_{\mathrm{sc}}^{\mathrm{grat}} = 18.1\,\frac{\mathrm{mA}}{\mathrm{cm}^2}$ for the multilayer with the nanopatterned interface. The increase in j_{sc} can be attributed to the nanotextured perovskite/air interface. For the full solar cell stack, the achievable short-circuit current densities have been reported in Ref. [85]. There, an increase of around 10 % for the nanopatterned structure was demonstrated. Therefore, we want to mention again that photon recycling is only a secondary effect, and the primary goal for the design of nanostructures has to be the light-trapping and absorption enhancement. To fully capture the performance of a solar cell, however, photon recycling needs to considered.

4.1.5 Summary of Photon Recycling in Perovskite Solar Cells

We have quantitatively investigated the photon recycling in a simplified perovskite multilayer and also in a complete perovskite solar cell device. Using the simplified stack, we could achieve good agreement with the emission measurements of fabricated samples and found strong directionality in the angular spectrum of the emitted power. Using eigenmode calculations, we could show that the dominant far-field features are intimately linked to the waveguide modes in the multilayer structure. Subsequently, we calculated the open-circuit voltage enhancement due to photon recycling, both for the simplified multilayer and the entire stack. In the case of the simplified stack, our nanograting shows a photon recycling performance between the planar case and the Lambertian case. For the full stack, we find that the additional gain in the open-circuit voltage can be a significant contribution to the total

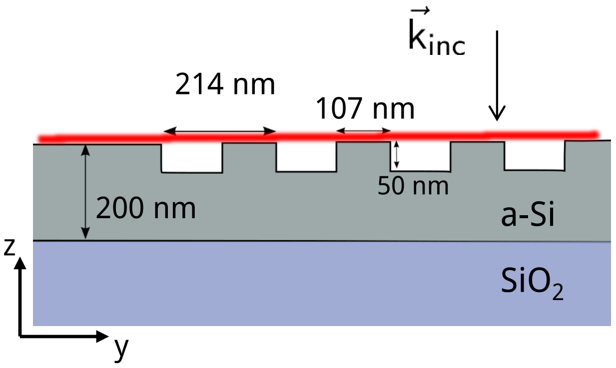

Figure 4.8: Schematic cross section of the grated multilayer waveguide. The WSe_2 monolayer is placed on top of the grating and indicated by the thin red layer (not to scale). The multilayer system is excited from the grating side with a laser.

open-circuit voltage. This demonstrates that photon recycling effects have to be considered in holistic approaches for optimizing the photon management in solar cell devices.

4.2 Directional Emission Enhancement

After the discussion of the impact of radiative reemission and reabsorption on the solar cell performance in the previous section, we will in this section consider a system where we specifically enhance and tailor the photoluminescence. Particularly, we will present results of resonantly coupling a two-dimensional WSe_2 monolayer to a nanotextured a-Si / SiO_2 waveguide structure. This was a joint project with the experimental group of Prof. Dragomir Neshev at the Australian National University in Canberra. Sample fabrication and measurements contained in this section have been performed by Haitao Chen, while we did the simulations and theoretical analyses. Through suitable design of the grating parameters, both excitation and emission wavelength can be coupled to waveguide modes in the multilayer system. By mediation of the grating, we could demonstrate, on the one hand, a directional preference of the emission depending on the polarization of the emitted electric field, and, on the other hand, a PL enhancement by a factor of around 8. The results of this section have been reported in Ref. [151].

4.2.1 Strategy and Methods

A commonly used strategy to enhance light-matter interaction is by tuning the local density of states of the photonic structure [152]. One aims for geometries where the structure couples to photonic modes at both the excitation and the emission wavelength. This would accelerate the excitation and the emission processes simultaneously, being obviously beneficial. This is possible if the system supports several resonances. With this in mind, we investigated a system consisting of a silicon waveguide grating on top of a glass substrate. As the emitting material we used a monolayer of WSe_2 that has been applied directly on top of the grating.

WSe_2 belongs to the material class of transition-metal dichalcogenides (TMDCs). Utilizing this material class, many possible usages as light sources have already been demonstrated [153, 154]. Among these applications are e. g. low-threshold lasers [155–157], single-

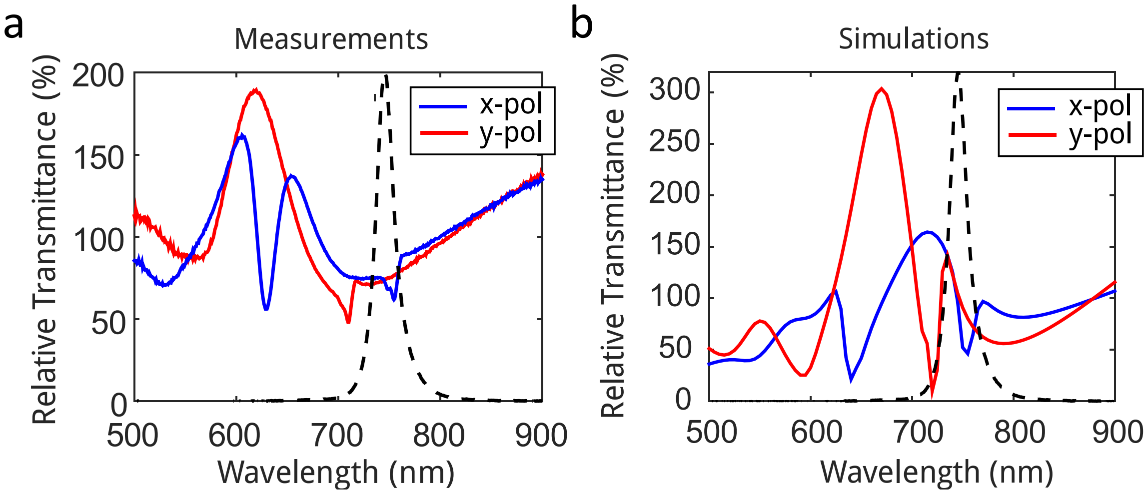

Figure 4.9: a) Measured and b) calculated relative transmittance of the grating-waveguide structure. The relative transmittance was calculated by normalizing the transmittance for the grating structure by the transmittance of the unpatterned multilayer. In both figures, the red curve refers to the polarization perpendicular to the grating, while the blue curve was obtained from the polarization parallel to the grating. The dashed black curve in both figures depicts the measured emission spectrum of the WSe_2 monolayer. Reprinted with permission from Ref. [151] (Copyright 2017 American Chemical Society).

photon emitters [158–162], excitonic light-emitting diodes [163, 164], cascaded single-photon emission [165] and second-harmonic generation [166–171]. These applications exploit that in the form of a two-dimensional monolayer, TMDCs have a direct bandgap [172–175].

A single layer of a TMDC shows a low emission efficiency due to its sub-nanometer thickness. As a consequence, many photonic structures have been put forward to enhance the emission. Among them, plasmonic structures were investigated [176–182] , but short-comings of them are their intrinsinc loss and confined near-field enhancements, which makes precise positioning necessary [181]. On the other hand, also dielectric photonic-crystal cavities have been proposed, where the emission enhancement relies on cavity modes [183–185]. While the application of TMDCs in silicon opto-electronic and on-chip applications is a highly sought target [9, 10], cavities are not feasible to be used in such devices [11], which is the reason why we are considering a silicon grating.

We proceed as follows: First, we optimize the grating parameters to facilitate the coupling at both the laser excitation wavelength and the emission wavelength of the WSe_2 monolayer. After a suitable grating period and height have been found where waveguide modes are supported at the desired wavelengths, we analyze in detail the different contributions to the total emission enhancement and the origin of the directional emission. We also demonstrate that the directionality of the far-field emission intensity can be filtered by using in the detection path a linear polarizer oriented parallel or perpendicular to the grating.

We used hydrogenated a-Si as the waveguiding layer (see Fig. 4.8), since its extinction coefficient is negligible in the relevant wavelength regime around 750 nm, which is due to its high optical bandgap of 1.73 eV [186]. Ellipsometry measurements were performed to determine the refractive index and extinction coefficient of the considered a-Si. On top of the grating, a monolayer of WSe_2 exfoliated from a bulk crystal was deposited. For the different measurements, the sample was excited from the positive z-direction with different lasers. For measuring the photoluminescence enhancement as a function of the excitation wavelength, a supercontinuum laser was used. For the time-resolved measurements, a pulsed laser with a central wavelength of 680 nm and a pulse duration of 140 fs was employed. The angular spectrum of the emission was measured using a He-Ne continuous-wave laser at a wavelength of 633 nm as the excitation source. To obtain the far-field in reciprocal space, a back-focal plane imaging method was used. This method enables to map every point in the image plane to an emission angle [187] and yields the angular spectrum as described in Sec. 2.3.1. In all cases, the photoluminescence measurements have been done from the same side as the laser excitation. Further details regarding the sample fabrication and measurements can be found in Ref. [151].

The numerical calculations are done with FEM. To calculate the transmittance, we used a layer stack of 200 nm thick glass substrate, 150 nm planar a-Si as guiding layer, an a-Si ridge with rectangular cross section, and finally just air. Top and bottom of the unit cell were set to PMLs, while in horizontal direction periodic boundary conditions were used. Plane waves were assumed to be incoming from the positive z-direction. In the measurements the laser was not completely paraxial, but showed a small defocusing. To account for this, the incoming laser pump light was described by a Gaussian pulse with a standard deviation of 2° and centered around normal incidence.

To numerically retrieve the far-field intensity of the emission from the WSe_2 monolayer, we again exploited the inverse Floquet method described in Sec. 2.3.3. The unit cell was kept the same as for the transmittance calculations. The emission that occurs in the WSe_2 monolayer was modeled as dipole emitters located vertically 1 nm above the grating. According to the measurements, the emission wavelength was chosen to be 750 nm, and the refractive index of a-Si at this wavelength is $n_{\mathrm{aSi}} = 3.91$. We solved for three different horizontal positions: In the center of the grating ridge, at the edge of the grating ridge, and close to the boundary of the unit cell. For all cases, the polarizations x and y (i. e. along and across the grating) were simulated, since out-of-plane dipole moments are not supported in the WSe_2 monolayer [187]. For the inverse Floquet method, the Bloch vector was discretized in 128×128 different values to get a sufficiently fine resolution of the angular spectrum of the far-field.

4.2.2 Analysis of the Photoluminescence Enhancement

From plane wave scattering calculations, we found that the optimal period and depth of the binary grating were $p = 214\,\mathrm{nm}$ and $h = 50\,\mathrm{nm}$ with a fill factor of 0.5. With these parameters, the coupling to waveguide modes at both, excitation and emission wavelength, was possible. In Fig. 4.9a and b, measured and calculated relative transmittance spectra are shown, respectively, that were obtained by dividing the transmittance in the grating region by the transmittance of the planar multilayer. In both graphs, the polarization in x-direction (blue curve) is equivalent to polarization parallel to the grating ridges, and the polarization

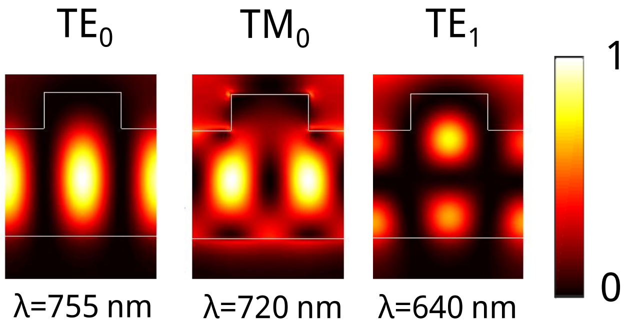

Figure 4.10: Calculated field intensity profiles at the wavelengths where the waveguide resonances occur. The modes are calculated for normal incident plane waves from the grating side. Adapted with permission from Ref. [151] (Copyright 2017 American Chemical Society).

in y-direction (red curve) is equivalent to polarization perpendicular to the grating ridges. The minima in the relative transmittance spectra correspond to the excitation of guided modes that propagate inside the structured a-Si layer. The strong pronunciation of these resonances suggests that a high coupling efficiency between the free-space radiation and the waveguide modes would be possible for the resonances of interest. At the positions of the resonances, we explicitly calculated the field intensity profiles (see Fig. 4.10) to clarify which modes were excited. These are the modes TE$_0$, TM$_0$, and TE$_1$. They are indicated in both transmittance plots are their respective position.

In Fig. 4.9a and b, we also show the PL emission spectrum of WSe$_2$ (black dashed line). It can be seen that there is an overlap of the emission with both TE$_0$ and TM$_0$ resonances. To also excite the TE$_1$ mode, the excitation wavelength has to be chosen around 640 nm so that it spectrally coincides with the respective mode resonance. There are discrepancies between the measurements and the calculations regarding the magnitudes and line shapes of the spectra, which are most likely due to fabrication and measurement inaccuracies. Besides that small deviations, the simulations capture well the relevant physical effects at the resonant wavelengths and linewidths of the waveguide mode resonances.

In Fig. 4.11a, an optical microscope image and a PL image of the sample are shown, respectively. It is apparent that the grating region shows a much higher photoluminescence than the flat region. For our purposes, we define the PL enhancement factor PL$_{\mathrm{ef}}$ to be the average on-grating intensity divided by the off-grating intensity, as given by the formula in Fig. 4.11a. In Fig. 4.11b, we show the emission spectra for the WSe$_2$, both above the grating and above the planar waveguide. As pump wavelength, we chose 633 nm to match the TE$_1$ resonance of the waveguide. The photoluminescence yield from the monolayer in the presence of the grating is up to 8 times larger than the photoluminescence yield for the off-grating area.

With the following measurements, we aim for distinguishing the contributions of excitation and emission enhancement to the total observed enhancement. Since we do not have any influence on the emission wavelength, we varied the excitation wavelength by using a supercontinuum laser. The plot of the wavelength-dependent photoluminescence enhancement is shown in Fig. 4.12a. We can observe the largest enhancement at the wavelength of 630 nm, which is exactly the wavelength of the TE$_1$ resonance of the multilayer. Due to the excitation being spectrally broader and pulsed, the total excitation enhancement is smaller than in the

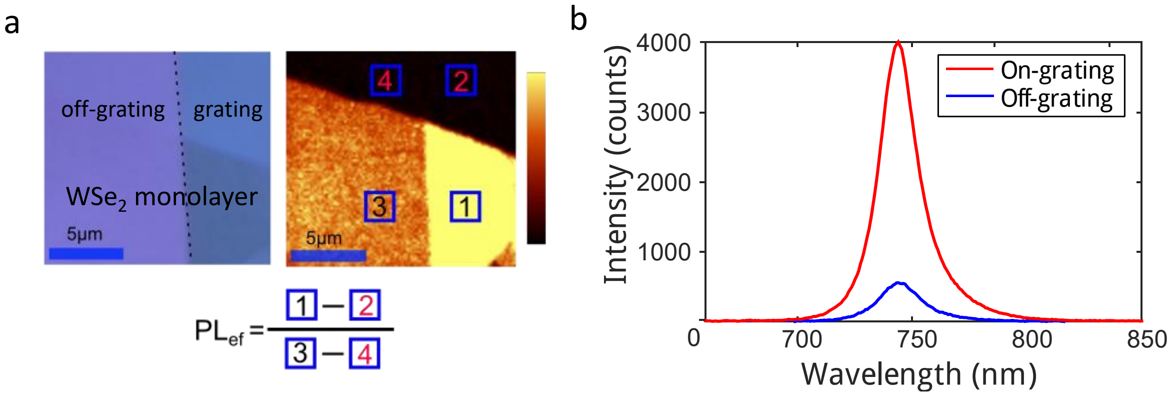

Figure 4.11: a) On the top right, a photograph of the sample is shown. The four areas refer to a planar region with (3) and without (4) the WSe$_2$ monolayer, as well as to a grated region with (1) and without (2) the WSe$_2$ monolayer. b) Photoluminescence spectra of the WSe$_2$ monolayer. The red curve was measured above the grating, the blue curve above a planar area. Large photoluminescence enhancement up to 8 times due to the grating can be observed. Reprinted with permission from Ref. [151] (Copyright 2017 American Chemical Society).

measurements with the continuous-wave laser. As a side effect, we hereby show that one can easily tailor the PL enhancement factor by changing the pump wavelength.

The influence of the grating on the coupling efficiency at the emission wavelength can be indirectly measured by considering that the radiative lifetime of the emitters is inversely proportional to the decay rate (cf. Eq. 2.45). To this end, time-resolved measurements with a laser at 680 nm excitation wavelength and resolution of 2 ps were done. In Fig. 4.12b, the decay curves are shown, both for on-grating and off-grating. Note that the intensity axis is logarithmic and that the initial intensity for both measurements was individually normalized to unity. The dots are measurements, the lines are bi-exponential fits [188]. For the sample on top of the grating (blue curve), the decay of WSe$_2$ is approximately two times faster, translating to a larger local density of states and thus to an increased coupling efficiency in the vicinity of the grating. The fact that the decay curves are not straight lines, but have a kink at around 90 ps suggests that at least two lifetimes are playing a role here. Finally, multiplying the enhancements at the excitation wavelength and at the emission wavelength, we indeed retrieve a total PL enhancement of around 8 times, hereby confirming the initially found enhancement value.

4.2.3 Directional Emission

Another important aspect that is worth to investigate, is the directionality of the emission due to the coupling to waveguide modes. The total angular spectrum of the far-field intensity (Fig. 4.13a) shows features at four distinct angular regions. They can be split by introducing a polarizer in the detection path. The far-field polarized across the grating (Fig. 4.13b) and along the grating (Fig. 4.13c) yield very different emission patterns. In the first case, the intensity is concentrated at angles corresponding to $k_y \approx 0.3k_0$, while in the latter case, most of the emission occurs in paraxial direction. This means that one can tailor the emission

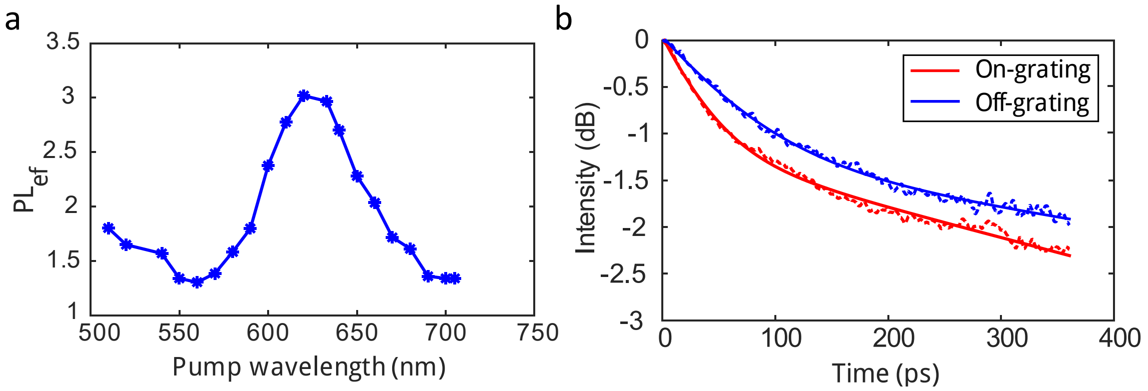

Figure 4.12: a) Photoluminescence enhancement factor PL_{ef} plotted over the laser pump wavelength. b) Time-resolved intensity measurement (dots) for both the on-grating and off-grating region of the sample, and bi-exponential fit (solid lines). Reprinted with permission from Ref. [151] (Copyright 2017 American Chemical Society).

properties by tuning the polarization state of the far-field. For comparison, in Fig. 4.13d, the far-field intensity pattern of a planar a-Si layer is shown. As expected, the intensity is basically rotationally symmetric and decays with increasing distance from the center.

With FEM calculations, we were able to reproduce these measured angular spectra. Figure 4.14a shows the calculated total far-field angular spectrum. We obtain very good agreement with the measurement results in Fig. 4.13a. Projecting the total far-field onto the axis perpendicular to the grating ridges yields Fig. 4.14b, which coincides with Fig. 4.13b. On the other hand, by projecting onto the axis parallel to the grating ridges (Fig. 4.14c), the emission pattern of Fig. 4.13c is reproduced.

The origin of the directional emission are the dispersion relations of the available waveguide modes. Figure 4.14d shows the two dispersion relations of the fundamental modes in a flat multilayer (SiO_2/175 nm a-Si/air): The green curve has as radius the effective refractive index of the TE_0 mode ($n_{TE_0} = 3.58$), while the red curves pertain to the TM_0 mode ($n_{TM_0} = 3.32$). The figure was obtained by considering the grating-mediated dispersion relations for the diffraction orders ± 1 in the first Brillouin zone using Eq. 2.83. The matching to the experimental and numerical results is excellent, so that we can conclude that the directionality indeed is caused by the dispersion of the waveguide modes to which the emission couples to.

At the emission wavelength of 750 nm, a-Si is barely absorbing, which means that the waveguide modes are only decaying due to outcoupling into the air or the glass side. This results in a large propagation length. 2D simulations consisting of 100 unit cells having a line dipole source placed above the central ridge are shown in Fig. 4.15: In a, the line dipole is polarized parallel to the grating ridge, whereas in b the line dipole is polarized perpendicular to the ridge. In further simulations also shown in Fig. 4.15a and b, we placed the dipole line source above a flat a-Si layer; in this case, there was much less outcoupled power visible, so that we can conclude that the radiation pattern is dominated by the radiative properties of the leaky waveguide modes. Without the grating, the waveguide modes do not outcouple into air and hence do not contribute to the measured PL signal.

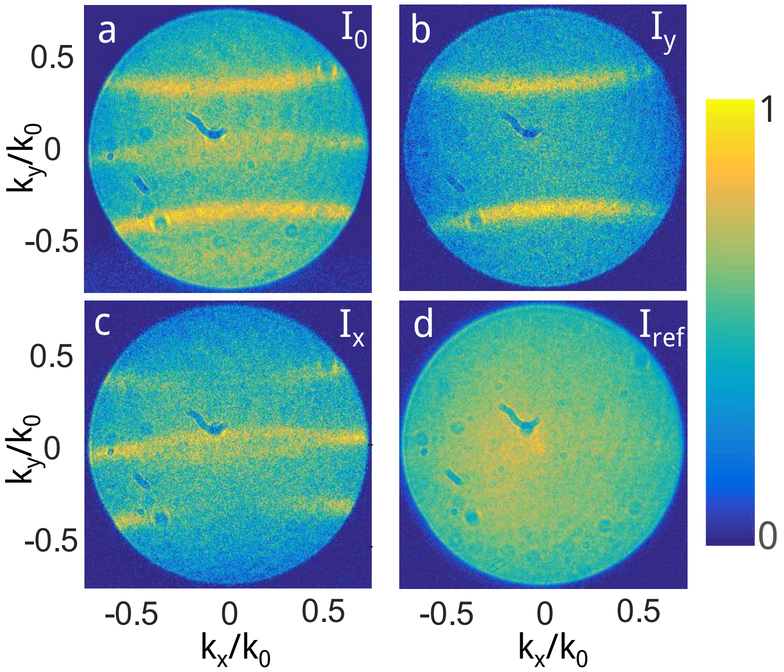

Figure 4.13: Measurement results of the WSe_2 emission using a back-focal plane method. a) Entire emission of the WSe_2 monolayer. b) Emission component polarized perpendicular (I_y) to the grating ridges. c) Emission component polarized parallel (I_x) to the grating ridges. Figures a-c have been obtained from the emission in the grating region. In d), for reference the emission of WSe_2 above a planar region is shown. Reprinted with permission from Ref. [151] (Copyright 2017 American Chemical Society).

4.2.4 Numerical Retrieval of the Emission Enhancement

From the single-dipole calculations, we can also obtain enhancement values for the photoluminescence by comparing the simulated spectra for the grating case with the corresponding results of a planar waveguide system. The planar multilayer is assumed to consist of a glass substrate with a 200 nm thick flat a-Si layer on top, and the dipole is again assumed to be 1 nm above the silicon. For both dipole orientations, we divide the total dipole emission power in the grating system, $P_{\text{tot}}^{\text{grat}}$, by the total dipole emission power for a flat system, $P_{\text{tot}}^{\text{flat}}$. This yields

$$\frac{P_{\text{tot},\perp}^{\text{grat}}}{P_{\text{tot}}^{\text{flat}}} = 1.5\,, \qquad \frac{P_{\text{tot},\|}^{\text{grat}}}{P_{\text{tot}}^{\text{flat}}} = 1.01\,. \tag{4.3}$$

Using Eq. 2.45, we can conclude that the dipoles oriented perpendicular to the grating have a shorter lifetime as in the planar system. The factor of 1.5 is comparable to the measured lifetime enhancement, where we found that the decay is approximately twice as fast in the presence of the grating compared to the planar waveguide. The parallel polarized dipoles have roughly the same lifetime as in the planar system.

For both the grating and the planar structure, the portion of outcoupled power of the WSe_2 emission was calculated by dividing the power that is radiated into air, P_{rad}, by the total

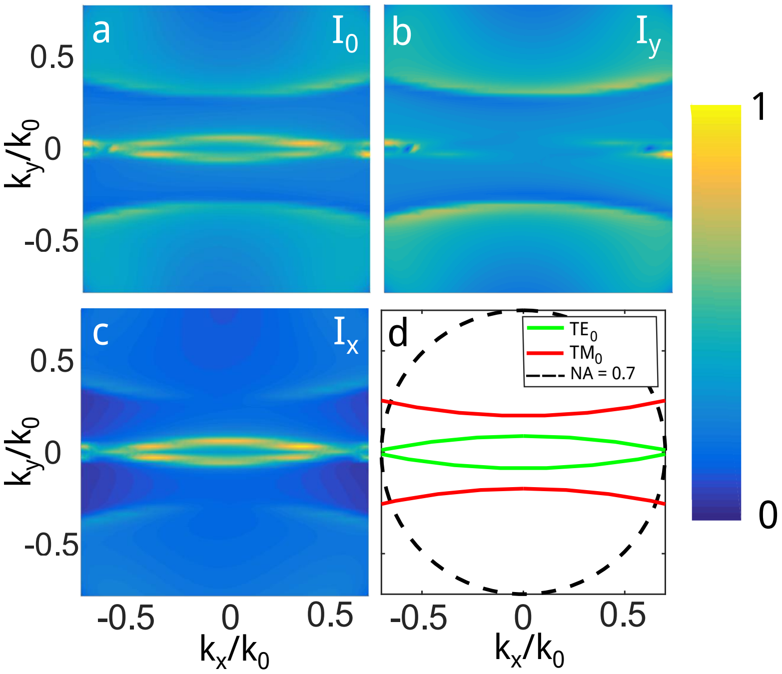

Figure 4.14: Numerically obtained angular spectra of the emission from a single dipole emitter. a) Total far-field angular spectrum averaged. b) Far-field angular spectrum calculated from the electric field components perpendicular (I_y) to the grating ridges. c) Far-field angular spectrum calculated from the electric field components parallel (I_x) to the grating ridges. d) Dispersion relations of the TE$_0$ and TM$_0$ waveguide modes, calculated for a wavelength of 750 nm. The radii of the two circle sections correspond to the effective refractive indices that were obtained from a planar eigenmode calculation, and the shift of the circles pertains to a grating period of 214 nm in y-direction. Reprinted with permission from Ref. [151] (Copyright 2017 American Chemical Society).

emitted power P_{tot}:

$$\frac{P_{\text{rad}}^{\text{grat}}}{P_{\text{tot}}^{\text{grat}}} = 0.26\,, \qquad \frac{P_{\text{rad}}^{\text{flat}}}{P_{\text{tot}}^{\text{flat}}} = 0.11\,. \tag{4.4}$$

Thus, the outcoupled power into air is larger in the presence of the grating, and the enhancement factor is $0.26/0.11 = 2.36$. Considering the decay rate enhancement factor of 1.5, both enhancements at the emission wavelength do not yield the experimentally measured factor of eight times PL enhancement. This, again, implies that not only the emission is enhanced by the grating.

To also gain access to the enhancement at the excitation wavelength, we calculated the field intensity 1 nm above the grating ridge for both the planar and textured waveguide. We simulated TE-polarized plane waves in angular incidence from the positive z-direction, hereby assuming for the incoming radiation again the same Gaussian profile as for the transmittance calculations to account for the slight defocusing of the laser. The wavelength range was chosen between 500 nm and 700 nm to capture the relevant pump wavelength at 633 nm. The intensity enhancement was calculated by dividing the average field intensity in the grating system by the intensity obtained in the planar calculation. A plot of the enhancement

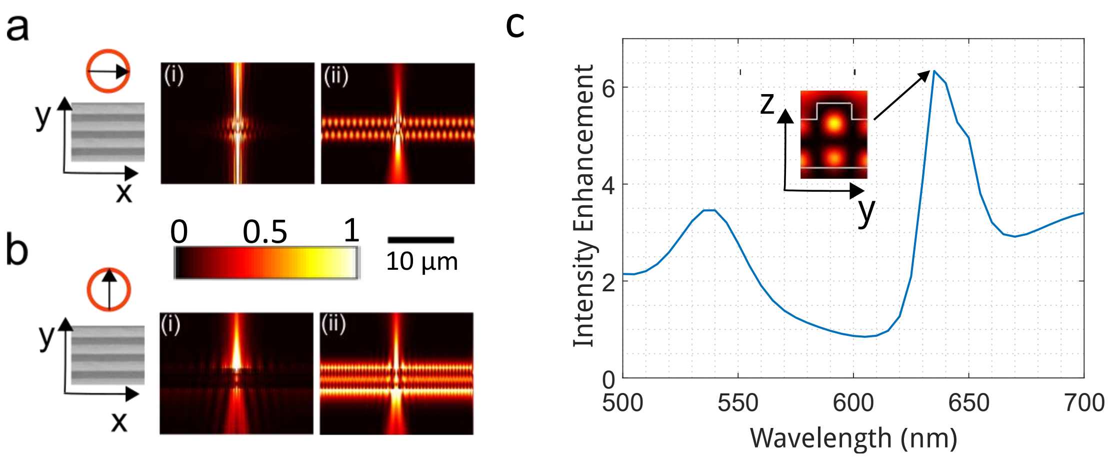

Figure 4.15: Two-dimensional simulation results for an electric line dipole oriented a) parallel and b) perpendicular to the grating ridges. In both a) and b), (i) refers to a flat multilayer, whereas (ii) was simulated considering the grating. For each case, 100 unit cells are considered and the line dipole is placed 1 nm above the texture (for the grating, the distance is measured to the grating ridge) and in the center of the computational domain. c) Calculated intensity enhancement above the grating compared to the flat waveguide as a function of the excitation wavelength. For both cases, the field intensity 1 nm above the grating was calculated considering incoming plane waves with TE polarization and the same Gaussian angle distribution that was used to obtain Fig. 4.9b. In the inset, the field profile for normal incidence at the peak intensity wavelength (640 nm) is shown. Reprinted with permission from Ref. [151] (Copyright 2017 American Chemical Society).

factor as a function of the wavelength is shown in Fig. 4.15c. Around 640 nm one can see a clear peak in the enhancement. The position of the peak is in good agreement with the measurement shown in Fig. 4.12a. The field profile at normal incidence and 640 nm (inset figure) shows that a TE mode is excited at this wavelength, which causes the enhancement factor to peak at around 6. This enhancement factor roughly translates to an enhancement factor of 6 of the absorption by the WSe_2 monolayer.

4.2.5 Summary of the Directional Emission Enhancement

In this project, the main scope was on the investigation of the enhanced and directional emission obtained from a WSe_2 monolayer above a grating structure. We demonstrated that the total photoluminescence enhancement can be attributed to an increase of the excitation and also to an increase of the emission. This is due to waveguide resonances that occur at the pump and also at the emission wavelength. The photoluminescence in the presence of the grating was up to 8 times larger than without the grating. Furthermore, the features of the directional emission could be excellently reproduced and explained by finite-element calculations. Notably, we are able to filter the dominant far-field intensity features for specific angles by simply applying polarization filters in the detection path.

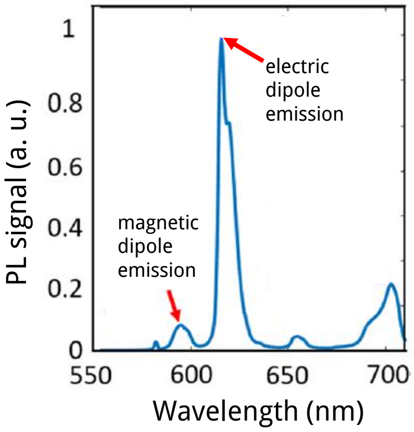

Figure 4.16: Photoluminescence spectrum of Eu^{3+}. Marked are the peaks of the magnetic-dipole dominated emission at 590 nm and the electric-dipole dominated emission at 610 nm. It is also visible that the emission at 610 nm is much stronger than at 590 nm, demanding for a normalization to be able to compare the emission enhancement. Reprinted with permission from Ref. [189] (Copyright 2017 American Chemical Society).

4.3 Relative Magnetic Dipole Enhancement

So far, we have only analyzed electric dipoles and their emission behavior when placed near to textured interfaces. A reason why this was done is the in general stronger interaction with electromagnetic fields that electric dipoles exhibit compared to magnetic dipoles. However, with progressing experimental techniques, the selective enhancement of magnetic dipole transitions has gained attention in recent years. In the following section, we will discuss how the magnetic dipole emission can be enhanced compared to the electric dipole emission. The approach is similar compared to the approach in the previous section regarding the enhanced and directional emission of the electric dipoles and also makes use of the inverse Floquet tranformation. In contrast, here we evoke the duality of Maxwell's equations as introduced in Sec. 2.1.3 to be able to simulate magnetic dipole emitters. The work discussed in this section is motivated by a collaboration with experimental partners. The experiments reported here were mainly performed at the Friedrich-Schiller-Universität Jena in the group of Isabelle Staude. Parts of the results that are presented here were reported in Ref. [189].

4.3.1 Approach and Methods

Dielectric nanoparticles and metasurfaces were shown in the past to enhance the electric dipole emission of fluorescent emitters [190–195]. For the magnetic dipole emission, similar experimental studies were not yet reported. Here, we consider as emitting material Eu^{3+} as a part of a polymer. This ion features spectrally close electric and magnetic dipole emission transitions, as can be seen in the photoluminescence spectrum in Fig. 4.16.

At a wavelength of $\lambda = 590\,\text{nm}$, Eu^{3+} predominantly emits as a magnetic dipole, whereas at $\lambda = 610\,\text{nm}$, the emission mainly stems from an electric dipole transition. This spectral vicinity is particularly useful, as in lowest-order approximation we can consider the local density of states in this spectral interval as constant. This decouples the effects due to intrinsic emission properties from the effects due to the environment, therefore we will focus on the geometrical parameters to engineer and evaluate the relative emission strength of the two transitions. The magnetic-dipole transition of such trivalent lanthanide ions has

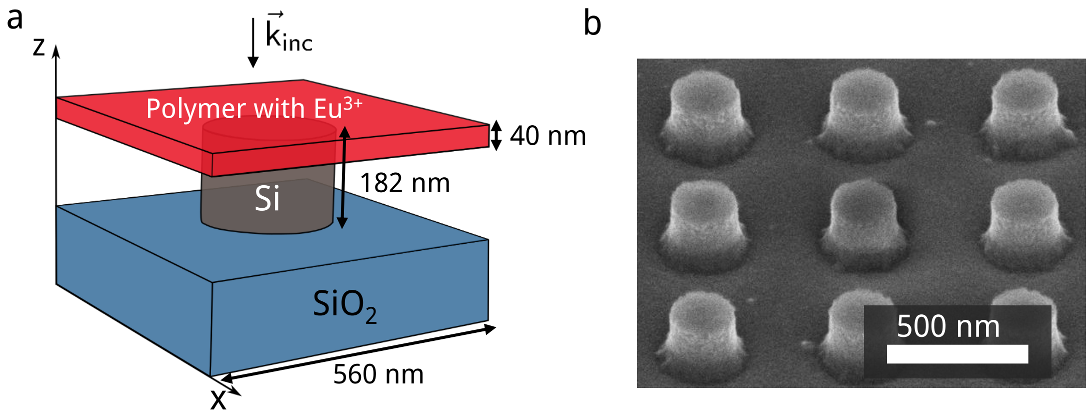

Figure 4.17: a) Sketch of the silicon nanodisk grating on the glass substrate with the polymer layer that contains the Eu^{3+} on top of it. The radius of the nanodisks was varied in the experiments between 90 nm and 146 nm. b) SEM micrograph of the nanodisk grating before adding the polymer. Adapted with permission from Ref. [189] (Copyright 2017 American Chemical Society).

already been investigated [196, 197]. To achieve magnetic emission enhancement, the LDOS was often manipulated with photonic structures in general, but mostly metallic elements were considered that sustain surface plasmon polaritons [190, 198, 199]. However, then the emission is typically quenched due to the intrinsic losses of metallic structures, which prompts to consider dielectric materials.

In the following, we will present experimental and numerical results concerning the enhancement of the magnetic dipole transition of Eu^{3+} compared to its electric dipole transition. This is achieved by engineering the optical environment of Eu^{3+} via a grating structure. The grating that we consider consists of a glass substrate with silicon nanodisks on top of it. The grating has a fixed period of 560 nm and the nanodisks have a fixed height of 182 nm. In the measurements, the radius of the nanodisks was varied between 96 nm and 146 nm. This size regime was chosen because the intrinsic quadrupolar-dominated resonances of the nanodisks with these sizes were in the spectral regime of the investigated dipole transitions, and quadrupole resonances had been shown before to enable magnetic dipole emission enhancement [200]. By varying the radius of the nanodisks, we can vary the spectral position of the quadrupole resonance and experimentally demonstrate that the magnetic dipole emission enhancement is indeed affected by the quadrupolar resonance and therefore by the nanodisk radius. Figure 4.17a shows a schematic sketch of the grating unit cell and in Fig. 4.17b, an SEM micrograph of the nanodisks grating is shown. In the experiments, the polymer is excited with a He-Cd laser with a central wavelength $\lambda = 325$ nm and the emission of Eu^{3+} was collected with an objective with NA $= 0.4$. The measurements in this section were done by Aleksander Vaskin at the Friedrich-Schiller-Universität Jena. For details of the sample fabrication and measurements procedure, we refer to Ref. [189].

To gain insights into the emission pattern of the two dipole transitions, we performed single-dipole FEM simulations for one unit cell. This was the main contribution of our side in this project. We numerically considered only one nanodisk radius, because the calculations are computationally very expensive. Furthermore, the experimental geometry was not totally known to us, and therefore our results are not intended to reproduce the experimental results perfectly. We simulated the electric dipole at the emission wavelength of 610 nm, and the magnetic dipole at the emission wavelength of 590 nm. The dipolar emitters were modelled as being placed inside a thin slab of the polymeric waveguide that has a wavelength-independent refractive index $n_{\mathrm{Eu}} = 1.6$ and a thickness of 40 nm. The layer was placed directly above the nanodisks. The emission occurring in the polymer layer from the dissolved emitters is modeled as a superposition of different dipole emitters. We considered the dipole to be placed at four horizontal positions: In the center of the unit cell, close to the corner, close to the edge, and half-way on the diagonal that goes through one corner and the center of the nanodisk. We also consider for each position the three polarizations along x, y, and z, respectively. The z-position of the dipoles was kept constant at a distance of 20 nm above the silicon nanodisk, which corresponds to the center plane of the polymer layer. For the refractive index of the silicon nanodisks, we used $n_{\mathrm{Si}}(590\,\mathrm{nm}) = 4.44 + 0.15\mathrm{i}$ and $n_{\mathrm{Si}}(610\,\mathrm{nm}) = 4.36 + 0.1\mathrm{i}$, which was provided by our experimental colleagues. To retrieve the angular spectrum of a single magnetic or electric dipole in this periodic environment, we employed the inverse Floquet method described in Sec. 2.3.3. Due to the calculations being computationally costly, we only considered the nanodisk radius where the measured relative enhancement was largest. We used a discretization into 64×64 different Bloch vectors for the simulations, which provided enough accuracy while still being computationally feasible. The reference simulations in the absence of the nanodisks were performed with PMLs as horizontal boundary conditions.

JCMsuite has a few limitations that we had to circumvent: It does neither allow a direct simulation of magnetic dipoles, nor does it provide the magnetic field of an electric dipole. Therefore, we exploited the duality of Maxwell's equations as described in Sec. 2.1.3: Having permittivity and permeability of the materials interchanged, we simulated an electric dipole. The resulting electric field $\vec{E}_{\mathrm{d}}$ is then proportional to the magnetic field of a magnetic dipole with regular material parameters: $\vec{E}_{\mathrm{d}} = -c\vec{B}$. To retrieve the electric field of the magnetic dipole, we applied in a last step the Maxwell-Ampere equation in Fourier space (Eq. 2.9) to the magnetic field. This was done by decomposing the far-field into plane waves by applying the angular spectrum method described in Sec. 2.3.1.

4.3.2 Results

We compared the normalized radiation at the emission wavelength of 590 nm ($G_{\mathrm{m}}(590\,\mathrm{nm})$) to the normalized emission at the emission wavelength of 610 nm ($G_{\mathrm{e}}(610\,\mathrm{nm})$). In both cases, the normalization is done by considering the emission of Eu^{3+} above the glass substrate without the nanodisks. The normalization is required, because the emission strengths of the two dipole transitions are intrinsically different, and a direct comparison would not yield any evidence about the relative enhancement. Hence, we calculate the figure of merit

$$\mathscr{G}_{\mathrm{r}} = \frac{G_{\mathrm{m}}(590\,\mathrm{nm})}{G_{\mathrm{e}}(610\,\mathrm{nm})}\,, \tag{4.5}$$

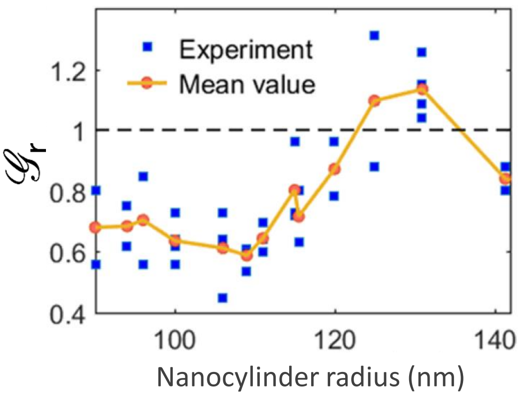

Figure 4.18: Relative emission enhancement $\mathscr{G}_\mathrm{r} = \mathrm{G_m}(590\,\mathrm{nm})/\mathrm{G_e}(610\,\mathrm{nm})$ of the magnetic dipole transition compared to the electric dipole transition as a function of the silicon nanodisk radius. The blue dots are the measurement results, the yellow curve is the mean value. A peak at a radius of 131 nm with a maximum relative enhancement of 1.12 is obtained. Reprinted with permission from Ref. [189] (Copyright 2017 American Chemical Society).

where $G_\mathrm{m,e}$ is defined for both dipole transitions as

$$G_\mathrm{m,e} = \frac{P^\mathrm{grat}_\mathrm{m,e}}{P^\mathrm{flat}_\mathrm{m,e}} \,. \tag{4.6}$$

Due to the numerical aperture, for the measurement results only power that is radiated into the angular cone corresponding to $k_{||}/k_0 \leq 0.4$ is considered.

The measured values for $\mathscr{G}_\mathrm{r}$ are plotted in Fig. 4.18 as a function of the nanodisk radius. We can observe that the emission enhancement ratio $\mathscr{G}_\mathrm{r}$ depends on the radius of the nanodisks. While for radii below 120 nm, the electric dipole emission is stronger enhanced than the magnetic dipole, the opposite occurs for radii larger than 120 nm. The minimum enhancement of the magnetic dipole relative to the electric dipole occurs at a radius of 109 nm and amounts to 0.6. More importantly, the maximum enhancement is 1.12 and occurs at a radius of 131 nm.

For the radius of 131 nm, we numerically calculated the far-field spectra of the dipole radiation in positive z-direction. This radius was chosen because it corresponds to the largest magnetic dipole emission enhancement. The far-fields are shown in Fig. 4.19. The spectra are averaged over the dipole orientations x, y, and z, and also over the four horizontal positions as described above. Since the four positions are in one quadrant of the unit cell, we rotated the resulting angular spectra to retrieve a resulting angular spectrum that corresponds to the symmetry of the underlying structure. Figure 4.19a displays the far-field spectrum of the electric dipole at the wavelength of 610 nm and in Fig. 4.19b, the far-field spectrum of the magnetic dipole at the emission wavelength of 590 nm is shown. Both emission spectra are normalized to the respective total emitted power. It is visible that the electric dipole emits significantly more power. This again suggests that one has to utilize normalized values in order to obtain the correct relative emission enhancement. The visible dispersion lines resemble the square grating.

We calculated the normalized total emission enhancement $\mathscr{G}^\mathrm{tot}$ and the enhancement of the

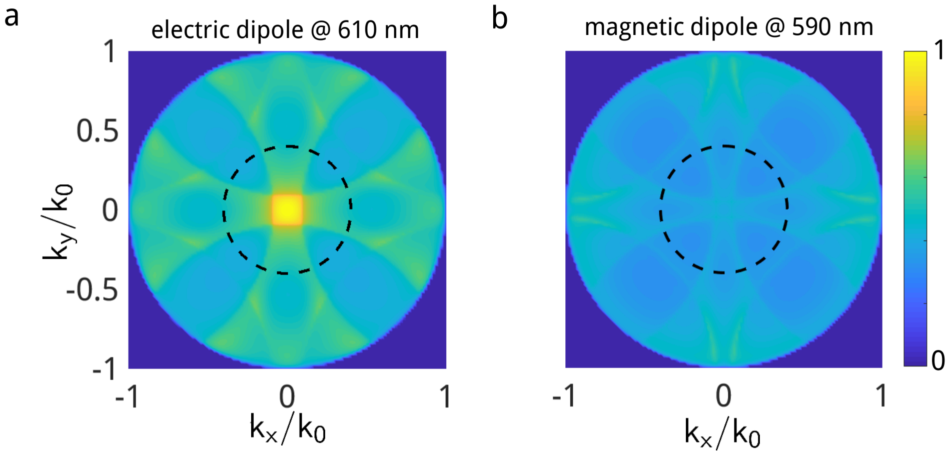

Figure 4.19: Far-field angular intensity distributions of a single dipole, averaged over the four considered horizontal positions and the three dipole orientations in x-, y-, and z-direction. The vertical position is 20 nm above the nanodisk, which corresponds to the center of the polymer layer. In a), the electric dipole far-field intensity pattern is shown at the emission wavelength of 610 nm, whereas in b), the magnetic dipole far-field intensity pattern is displayed for the emission wavelength of 590 nm. Both plots are individually normalized to the total emitted power at the respective wavelength. The color scale is the same and the axes are normalized to the wavevector in vacuum.

radiated power into air $\mathscr{G}^{\mathrm{rad}}$ with the relations

$$\mathscr{G}^{\mathrm{tot}} = \frac{G_{\mathrm{m}}^{\mathrm{tot}}(590\,\mathrm{nm})}{G_{\mathrm{e}}^{\mathrm{tot}}(610\,\mathrm{nm})} = 0.96\,, \qquad \mathscr{G}^{\mathrm{rad}} = \frac{G_{\mathrm{m}}^{\mathrm{rad}}(590\,\mathrm{nm})}{G_{\mathrm{e}}^{\mathrm{rad}}(610\,\mathrm{nm})} = 0.69. \tag{4.7}$$

For $\mathscr{G}^{\mathrm{rad}}$, we obtain a value smaller than unity, meaning that our simulations can not reproduce the experimental result. Reasons for this can be, e. g. the fact that we consider the total radiation into air, whereas the measurements use NA$=0.4$. Another error source can be that in the experiments, the polymer fills the entire space between the nanodisks. In our simulations, we considered only a thin layer above the nanodisks. Lastly, the distribution of the dipole emitters inside the polymer also has an effect on the total emission: The relative enhancement for the emitter in the center of the unit cell is $\mathscr{G}^{\mathrm{rad}}_{\mathrm{center}} = 5.64$, indicating that the dipoles near the center of the unit cell contribute stronger to the total emission.

4.3.3 Summary of the Relative Magnetic Dipole Enhancement

To summarize, in this project we could engineer the parameters of a dielectric grating to achieve enhancement of magnetic dipole emission relative to a spectrally close electric dipole emission of the same material. By varying the radii of the nanodisks, different relative enhancements have been obtained. The measurements were accompanied by simulations of the far-field emission spectrum that exploited the duality of Maxwell's equations. Due to a few simplifications of the considered geometry, agreement in the relative enhancement factor could not be achieved for the average dipole emission.

5 Summary and Outlook

The scope of this thesis was the numerical analysis of scattering interfaces of various kinds. We spanned the arc from the analysis of rough textures in solar cells to the investigation of magnetic dipole transitions near periodically arranged nanodisks. All these systems had in common that the interaction of light with the environment was key to understand the physics.

Let us now recapitulate the main results that we have presented in this thesis.

One important contribution that this thesis comprises is the analysis of a bottom-up approach that bears the hope to fabricate inexpensive and on large-scale broadband-efficient solar cells. Considering the results, we think we can be confident that the approach is indeed suitable for usages in the photovoltaic industry, although the experimental realization of textures that can be actually used in solar cells still requires further efforts.

We also contributed to the small but nevertheless important area of photon recycling. Due to being a second order mechanism, it is not widely known in the solar cell research community. The results that we obtained show that the consideration of photon recycling should constitute an integral part of solar cell optimization. This holds particularly true when working towards record-efficiency solar cells. As a by-product, the waveguide modes in a thin-film perovskite layer have been obtained, and we could show correspondence to the angular spectrum of the far-field emitted from a dipole inside the perovskite. This section concluded the solar cell related topics.

We also considered dipole emission in the vicinity of grating structures, with the ultimate goal to enhance the total power emitted by the dipole. The first project revolved around the investigation of the mechanisms that led to a considerable PL enhancement of an emitting TMDC monolayer above a silicon waveguide grating. The challenging idea was to design a grating structure that would couple, on the one hand, to the wavelength at which the dipole emits, but on the other hand also to the pump laser wavelength. With the numerical results we obtained, we could conclusively show how the total PL enhancement results from an increase of the LDOS at the pump wavelength and also from an enhanced outcoupling from the grating waveguide at the emission wavelength.

Last but not least, we have also studied the emission of magnetic dipoles. Here, not the total enhancement, but the relative enhancement of the magnetic dipole emission as compared to the electric dipole emission was of interest. We could identify a grating geometry where this could be achieved in the experiments. The measurements were accompanied by simulations that exploited the duality of Maxwell's equations. This enabled the computation of the response of a magnetic dipole.

Not just various questions have been answered in this thesis, but, moreover, multiple questions where found that could unfortunately not be addressed in this thesis anymore. First, the bottom-up approach using the nanospheres can also be used to fabricate binary structures with nanocylinders or nanoholes, whose position and diameter are determined by the position and size of the nanospheres. Such binary structures are e. g. relevant in the context of metasurfaces. Such metasurfaces could offer unprecedented possibilities to manipulate light propagation and scattering, while at the same time providing an inexpensive fabrication method. Another application of such binary textures could be the wavefront shaping of light that propagates through a stack of multiple such textures. There are many possible applications that are waiting to be tackled using this kind of bottom-up approach.

Another relevant aspect that could not be investigated is the behavior of emitters close to disordered textures. Disordered interfaces promise to show effects like light localization, and if one could systematically identify such localization spots, the radiative emission could be boosted significantly. In the field of photon recycling, the calculations as presented in this thesis could be extended to many other nanotextures and possibly even tandem cells. This would provide more insights into the quantitative contributions of photon recycling in such devices.

Having said that, we conclude these remarks and the thesis.

Acknowledgements

First of all, I would like to thank Carsten Rockstuhl for giving me the possibility to do both my master thesis and my PhD thesis in his group. With this, I had the pleasure to spend more than five years under his supervision and experience the growth of his newly formed group at KIT. His scientific guidance and enthusiasm about science in general was a great motivating factor during the whole time. Equally important, he provided the frame for my personal development and encouraged me also to disseminate my research results in conferences and workshops all over the world.

I also want to thank Aimi Abass for providing lots of advice and support during my PhD time. His experience in the field of solar cells was a great help for my work. I also consider his efforts to improve my scientific abilities an invaluable contribution to my PhD time. I learnt a lot in plenty of discussions with him and I really enjoyed working with him. I also thank him for proofreading all my manuscripts and also parts of this thesis.

I thank all colleagues who were responsible for the measurements for the productive collaborations and the inspiring discussions. Particularly, I am grateful to Peter Piechulla and Alexander Sprafke at the University of Halle, Haitao Chen at the University of Canberra, Aleksander Vaskin at the University of Jena, and Raphael Schmager, Ulrich Paetzold, and Guillaume Gomard at the Light Technology Institute of KIT.

I want to thank Prof. Ulrich Lemmer for agreeing to act as second referee. Furthermore, I want to thank the people from JCMwave for freely providing the versatile Maxwell solver JCMsuite, and for being available for technical support. In this regard, I am especially obliged to Sven Burger and Philipp Gutsche.

I would like to thank all present and past members of the photonics group for the enjoyable years, scientific discussions, and joint activities. I also want to thank the Karlsruhe School of Optics and Photonics for providing a graduate program. Particularly, the MBA Fundamentals program provided insights into interesting topics beyond physics. Also, I want to thank the Deutsche Forschungsgemeinschaft for financial support within the program 'Tailored Disorder'.

I want to thank Matthias Bard and my brother Philipp for proofreading the thesis. Furthermore, I would like to thank Andreas Poenicke for excellent IT support. I also want to thank Andreas Vetter for the joint learning sessions in the months before the PhD defense. I also would like to thank all my friends for the great time that we spent together. Last but not least, I would like to thank my family for unconditional support during my education.

Bibliography

[1] M. Powalla, S. Paetel, D. Hariskos, R. Wuerz, F. Kessler, P. Lechner, W. Wischmann, and T. M. Friedlmeier, *Advances in Cost-Efficient Thin-Film Photovoltaics Based on Cu(In,Ga)Se*$_2$, Engineering **3** (2017), 445–451.

[2] S. Wiesendanger, M. Zilk, T. Pertsch, F. Lederer, and C. Rockstuhl, *A path to implement optimized randomly textured surfaces for solar cells*, Appl. Phys. Lett. **103** (2013), 131115.

[3] P. M. Piechulla, L. Muehlenbein, R. B. Wehrspohn, S. Nanz, A. Abass, C. Rockstuhl, and A. Sprafke, *Fabrication of Nearly-Hyperuniform Substrates by Tailored Disorder for Photonic Applications*, Adv. Opt. Mater. **6** (2018), 1701272, doi:10.1002/adom.201701272.

[4] X. Zhang, J.-X. Shen, W. Wang, and C. G. Van de Walle, *First-Principles Analysis of Radiative Recombination in Lead-Halide Perovskites*, ACS Energy Lett. **3** (2018), 2329–2334.

[5] J. E. Parrott, *Radiative recombination and photon recycling in photovoltaic solar cells*, Sol. Energy Mater. Sol. Cells **30** (1993), 221–231.

[6] V. Badescu and P. T. Landsberg, *Influence of photon recycling on solar cell efficiencies*, Semicond. Sci. Technol. **12** (1997), 1491–1497.

[7] L. M. Pazos-Outon, M. Szumilo, R. Lamboll, J. M. Richter, M. Crespo-Quesada, M. Abdi-Jalebi, H. J. Beeson, M. Vrucinic, M. Alsari, H. J. Snaith, B. Ehrler, R. H. Friend, and F. Deschler, *Photon recycling in lead iodide perovskite solar cells*, Science **351** (2016), 1430–1433.

[8] Z. Gan, W. Chen, L. Yuan, G. Cao, C. Zhou, S. Huang, X. Wen, and B. Jia, *External stokes shift of perovskite nanocrystals enlarged by photon recycling*, Appl. Phys. Lett. **114** (2019), 011906.

[9] D. Sell, J. Yang, S. Doshay, K. Zhang, and J. A. Fan, *Visible light metasurfaces based on single-crystal silicon*, ACS Photonics **3** (2016), 1919–1925.

[10] I. Staude and J. Schilling, *Metamaterial-inspired silicon nanophotonics*, Nat. Photonics **11** (2017), 274–284.

[11] D. J. Lockwood and L. Pavesi, *Silicon Photonics*, Springer-Verlag, New York, 2004.

[12] J. D. Jackson, *Classical Electrodynamics*, 3rd ed., John Wiley & Sons, New York City, New York, 1998.

[13] R. B. Wehrspohn, U. Rau, and A. Gombert (eds.), *Photon Management in Solar Cells*, Wiley-VCH, Weinheim, 2015.

[14] D. Drosdoff and A. Widom, *Snell's law from an elementary particle viewpoint*, Am. J. Phys. **73** (2005), 973–975.

[15] M. Green and M. Keevers, *Optical properties of intrinsic silicon at 300* K, Prog. Photov. Res. Appl. **3** (1995), 189–192.

[16] I. Fernandez-Corbaton and G. Molina-Terriza, *Role of duality symmetry in transformation optics*, Phys. Rev. B **88** (2013), 085111.

[17] I. Fernandez-Corbaton, X. Zambrana-Puyalto, N. Tischler, X. Vidal, M. L. Juan, and G. Molina-Terriza, *Electromagnetic Duality Symmetry and Helicity Conservation for the Macroscopic Maxwell's Equations*, Phys. Rev. Lett. **111** (2013), 060401.

[18] M. Paulus, P. Gay-Balmaz, and O. J. F. Martin, *Accurate and efficient computation of the Green's tensor for stratified media*, Phys. Rev. E **62** (2000), 5797–5807.

[19] S. Y. Buhmann, *Dispersion Forces I: Macroscopic Quantum Electrodynamics and Ground-State Casimir, Casimir-Polder and van der Waals Forces*, Springer Tracts in Modern Physics, Springer-Verlag, 2012.

[20] T. M. Søndergaard, *Green's Function Integral Equation Methods in Nano-Optics*, CRC Press, Boca Raton, Florida, 2019.

[21] J. E. Sipe, *New Green-function formalism for surface optics*, J. Opt. Soc. Am. B **4** (1987), 481–489.

[22] P. Johansson, *Electromagnetic Green's function for layered systems: Applications to nanohole interactions in thin metal films*, Phys. Rev. B **83** (2011), 195408.

[23] L. Novotny and B. Hecht, *Principles of Nano-Optics*, 2nd ed., Cambridge University Press, Cambridge, 2012.

[24] E. M. Purcell, *Spontaneous Emission Probabilities at Radio Frequencies*, Phys. Rev. **69** (1946), 681.

[25] S.-A. Biehs and J.-J. Greffet, *Statistical properties of spontaneous emission from atoms near a rough surface*, Phys. Rev. A **84** (2011), 052902.

[26] K. H. Drexhage, *Influence of a dielectric interface on fluorescence decay time*, J. Lumin. **1-2** (1970), 693–701.

[27] P. B. Johnson and R. W. Christy, *Optical Constants of the Noble Metals*, Phys. Rev. B **6** (1972), 4370–4379.

[28] J. Goodman, *Introduction to Fourier Optics*, 3rd ed., Roberts and Company Publishers, Greenwood Village, Colorado, 2005.

[29] M. Nieto-Vesperinas, *Scattering and Diffraction in Physical Optics*, 1st ed., vol. 1st, John Wiley & Sons, New York City, New York, 1991.

[30] N. Sahraei, K. Forberich, S. Venkataraj, A. G. Aberle, and M. Peters, *Analytical solution for haze values of aluminium-induced texture (AIT) glass superstrates for a-Si:H solar cells*, Opt. Express **22** (2014), A53–A67.

[31] O. K. Ersoy, *Diffraction, Fourier Optics and Imaging*, John Wiley & Sons, Hoboken, New Jersey, 2006.

[32] J. D. Joannopoulos, S. G. Johnson, J. N. Winn, and R. D. Meade, *Photonic Crystals – Molding the Flow of Light*, 2nd ed., Princeton University Press, 2008.

[33] L. Zschiedrich, H. J. Greiner, S. Burger, and F. Schmidt, *Numerical analysis of nanostructures for enhanced light extraction from OLEDs*, Proc. SPIE **8641** (2013), 86410B.

[34] D. Sjöberg, C. Engström, G. Kristensson, D. J. N. Wall, and N. Wellander, *A Floquet–Bloch Decomposition of Maxwell's Equations Applied to Homogenization*, Multiscale Model. Simul. **4** (2005), 149–171.

[35] B. E. A. Saleh and M. C. Teich, *Fundamentals of Photonics*, 2nd ed., John Wiley & Sons, Hoboken, New Jersey, 2007.

[36] K. K. Y. Lee, Y. Avniel, and S. G. Johnson, *Rigorous sufficient conditions for index-guided modes in microstructured dielectric waveguides*, Opt. Express **16** (2008), 9261–9275.

[37] A. Abass, *Light Absorption Enhancement and Electronic Properties of Thin-Film Solar Cells*, Doctoral Thesis, Ghent University, September 2014.

[38] T. Tamir and S. T. Peng, *Analysis and Design of Grating Couplers*, Appl. Phys. **14** (1977), 235–254.

[39] P. Würfel, *Physik der Solarzellen*, 2nd ed., Springer Spektrum, 2000.

[40] D. K. Gupta, M. Langelaar, M. Barink, and F. van Keulen, *Optimizing front metallization patterns: Efficiency with aesthetics in free-form solar cells*, Renew. Energ. **86** (2016), 1332–1339.

[41] ASTM, *Standard Tables for Reference Solar Spectral Irradiances: Direct Normal and Hemispherical on* 37° *Tilted Surface*, 2012, West Conshohocken (PA): American Society for Testing and Materials. Available from https://www.astm.org.

[42] W. Shockley and H. J. Queisser, *Detailed Balance Limit of Efficiency of p-n Junction Solar Cells*, J. Appl. Phys. **32** (1961), 510–519.

[43] S. Rühle, *Tabulated values of the Shockley–Queisser limit for single junction solar cells*, Sol. Energy **130** (2016), 139–147.

[44] A. De Vos, *Detailed balance limit of the efficiency of tandem solar cells*, J. Phys. D: Appl. Phys. **13** (1980), 839–846.

[45] O. D. Miller, E. Yablonovitch, and S. R. Kurtz, *Strong Internal and External Luminescence as Solar Cells Approach the Shockley–Queisser Limit*, IEEE J. Photovolt. **2** (2012), 303–311.

[46] B. Blank, T. Kirchartz, S. Lany, and U. Rau, *Selection Metric for Photovoltaic Materials Screening Based on Detailed-Balance Analysis*, Phys. Rev. Appl. **8** (2017), 024032.

[47] M. Padilla, B. Michl, B. Thaidigsmann, W. Warta, and M. C. Schubert, *Short-circuit current density mapping for solar cells*, Sol. Energy Mater. Sol. Cells **120** (2014), 282–288.

[48] S. Jain, V. Depauw, V. D. Miljkovic, A. Dmitriev, C. Trompoukis, I. Gordon, P. Van Dorpe, and O. El Daif, *Broadband absorption enhancement in ultra-thin crystalline Si solar cells by incorporating metallic and dielectric nanostructures in the back reflector*, Prog. Photov. Res. Appl. **23** (2015), 1144–1156.

[49] J. Krepelka, *Maximally flat antireflection coatings*, J. Me. Op. **37** (1992), 53–56.

[50] D. Poitras and J. A. Dobrowolski, *Toward perfect antireflection coatings. 2. Theory*, Appl. Opt. **43** (2004), 1286–1295.

[51] K.-H. Kim and Q-H. Park, *Perfect anti-reflection from first principles*, Sci. Rep. **3** (2013), 1062.

[52] U. W. Paetzold, *Light trapping with plasmonic back contacts in thin-film silicon solar cells*, Doctoral Thesis, RWTH Aachen, 2013.

[53] E. M. Salido, L. N. Servalli, J. C. Gomez, and C. Verrastro, *Phototransduction early steps model based on Beer-Lambert optical law*, Vis. Res. **131** (2017), 75–81.

[54] S. J. Fonash, *Introduction to Light Trapping in Solar Cell and Photo-detector Devices*, 1st ed., Academic Press, 2015.

[55] R. Yu, Q. Lin, S.-F. Leung, and Z. Fan, *Nanomaterials and nanostructures for efficient light absorption and photovoltaics*, Nano Energy **1** (2012), 57–72.

[56] S. Mokkapati and K. R. Catchpole, *Nanophotonic light trapping in solar cells*, J. Appl. Phys. **112** (2012), 101101.

[57] H.-P. Wang, D.-H. Lien, M.-L. Lien, C.-A. Lin, H.-C. Chang, K.-Y. Lai, and J.-H. He, *Photon management in nanostructured solar cells*, J. Mater. Chem. C **2** (2014), 3144–3171.

[58] C. S. Solanki and H. K. Singh, *Anti-reflection and Light Trapping in c-Si Solar Cells*, Springer Singapore, 2017.

[59] R. B. Wehrspohn and J. Üpping, *3D photonic crystals for photon management in solar cells*, J. Opt. **14** (2012), 024003.

[60] M. Wellenzohn and R. Hainberger, *On the light trapping mechanism in silicon solar cells with backside diffraction gratings*, Proc. SPIE **8981** (2014), 89811O.

[61] C. S. Schuster, A. Bozzola, L. C. Andreani, and T. F. Krauss, *How to assess light trapping structures versus a Lambertian Scatterer for solar cells?*, Opt. Express **22** (2014), A542–A551.

[62] G. H. Meeten, *Refractive index errors in the critical-angle and the Brewster-angle methods applied to absorbing and heterogeneous materials*, Meas. Sci. Technol. **8** (1997), 728–733.

[63] E. Yablonovitch, *Statistical ray optics*, J. Opt. Soc. Am. **72** (1982), 899–907.

[64] Z. Yu, A. Raman, and S. Fan, *Fundamental limit of nanophotonic light trapping in solar cells*, Proc. Natl. Acad. Sci. U.S.A. **107** (2010), 17491–17496.

[65] C. Eisele, C. E. Nebel, and M. Stutzmann, *Periodic light coupler gratings in amorphous thin film solar cells*, J. Appl. Phys. **89** (2001), 7722–7726.

[66] A. Abass, K. Q. Le, A. Alu, M. Burgelman, and B. Maes, *Dual-interface gratings for broadband absorption enhancement in thin-film solar cells*, Phys. Rev. B **85** (2012), 115449.

[67] S. Pillai, K. R. Catchpole, T. Trupke, and M.A. Green, *Surface plasmon enhanced silicon solar cells*, J. Appl. Phys. **101** (2007), 093105.

[68] M. A. Green and S. Pillai, *Harnessing plasmonics for solar cells*, Nat. Photon. **6** (2012), 130–132.

[69] C. Rockstuhl, F. Lederer, K. Bittkau, and R. Carius, *Light localization at randomly textured surfaces for solar-cell applications*, Appl. Phys. Lett. **91** (2007), 171104.

[70] S. Fahr, T. Kirchartz, C. Rockstuhl, and F. Lederer, *Approaching the Lambertian limit in randomly textured thin-film solar cells*, Opt. Express **19** (2011), A865–A874.

[71] C. Battaglia, C.-M. Hsu, K. Söderström, J. Escarré, F.-J. Haug, M. Charrière, M. Boccard, M. Despeisse, D.T.L. Alexander, M. Cantoni, Y. Cui, and C. Ballif, *Light Trapping in Solar Cells: Can Periodic Beat Random?*, ACS Nano **6** (2012), 2790–2797.

[72] M. Peters, C. Battaglia, K. Forberich, B. Bläsi, N. Sahraei, and A. G. Aberle, *Comparison between periodic and stochastic parabolic light trapping structures for thin-film microcrystalline silicon solar cells*, Opt. Express **20** (2012), 29488–29499.

[73] P. Kowalczewski, A. Bozzola, M. Liscidini, and L. C. Andreani, *Light trapping and electrical transport in thin-film solar cells with randomly rough textures*, J. Appl. Phys. **115** (2014), 194504.

[74] U. W. Paetzold, M. Smeets, M. Meier, K. Bittkau, T. Merdzhanova, V. Smirnov, D. Michaelis, C. Waechter, R. Carius, and U. Rau, *Disorder improves nanophotonic light trapping in thin-film solar cells*, Appl. Phys. Lett. **104** (2014), 131102.

[75] M.-C. van Lare and A. Polman, *Optimized Scattering Power Spectral Density of Photovoltaic Light-Trapping Patterns*, ACS Photonics **2** (2015), 822–831.

[76] C. Trompoukis, I. Massiot, V. Depauw, O. El Daif, K. Lee, A. Dmitriev, I. Gordon, R. Mertens, and J. Poortmans, *Disordered nanostructures by hole-mask colloidal lithography for advanced light trapping in silicon solar cells*, Opt. Express **24** (2016), A191–A201.

[77] A. Oskooi, P. A. Favuzzi, Y. Tanaka, H. Shigeta, Y. Kawakami, and S. Noda, *Partially disordered photonic-crystal thin films for enhanced and robust photovoltaics*, Appl. Phys. Lett. **100** (2012), 181110.

[78] A. Yangui, *Etude des propriétés optiques et structurales des matériaux hybrides organiques-inorganiques à base de Plomb : émission de lumière blanche*, Doctoral Thesis, Université Paris-Saclay, 2016.

[79] E. F. Schubert, *Light-Emitting Diodes*, 2nd ed., Cambridge University Press, Cambridge, 2010.

[80] H. Zhao, G. Liu, J. Zhang, R. A. Arif, and N. Tansu, *Analysis of Internal Quantum Efficiency and Current Injection Efficiency in III-Nitride Light-Emitting Diodes*, J. Disp. Technol. **9** (2013), 212–225.

[81] T. Kirchartz, F. Staub, and U. Rau, *Impact of Photon Recycling on the Open-Circuit Voltage of Metal Halide Perovskite Solar Cells*, ACS Energy Lett. **1** (2016), 731–739.

[82] M. G. Abebe, A. Abass, G. Gomard, L. Zschiedrich, U. Lemmer, B. S. Richards, C. Rockstuhl, and U. W. Paetzold, *Rigorous wave-optical treatment of photon recycling in thermodynamics of photovoltaics: Perovskite thin-film solar cells*, Phys. Rev. B **98** (2018), 075141.

[83] T. K. Nguyen, P. T. Dang, and K. Q Le, *Numerical design of thin perovskite solar cell with fiber array-based anti-reflection front electrode for light-trapping enhancement*, J. Opt. **18** (2016), 1–6.

[84] Y. Wang, P. Wang, X. Zhou, C. Li, H. Li, X. Hu, F. Li, X. Liu, M. Li, and Y. Song, *Diffraction-Grated Perovskite Induced Highly Efficient Solar Cells through Nanophotonic Light Trapping*, Adv. Energy Mater. **8** (2018), 1702960.

[85] R. Schmager, G. Gomard, B. S. Richards, and U. W. Paetzold, *Nanophotonic perovskite layers for enhanced current generation and mitigation of lead in perovskite solar cells*, Sol. Energy Mater. Sol. Cells **192** (2019), 65–71.

[86] J. M. Richter, M. Abdi-Jalebi, A. Sadhanala, M. Tabachnyk, J. P.H. Rivett, L. M. Pazos-Outón, K. C. Gödel, M. Price, F. Deschler, and R. H. Friend, *Enhancing photoluminescence yields in lead halide perovskites by photon recycling and light out-coupling*, Nat. Commun. **7** (2016), 1–8.

[87] S. V. Makarov, V. Milichko, E. V. Ushakova, M. Omelyanovich, A. Cerdan Pasaran, R. Haroldson, B. Balachandran, H. Wang, W. Hu, Y. S. Kivshar, and A. A. Zakhidov, *Multifold Emission Enhancement in Nanoimprinted Hybrid Perovskite Metasurfaces*, ACS Photonics **4** (2017), 728–735.

[88] T. Tayagaki, K. Makita, R. Oshima, H. Mizuno, and T. Sugaya, *Impact of nanometer air gaps on photon recycling in mechanically stacked multi-junction solar cells*, Opt. Express **27** (2019), A1–A10.

[89] U. Rau, U. W. Paetzold, and T. Kirchartz, *Thermodynamics of light management in photovoltaic devices*, Phys. Rev. B **90** (2014), 035211.

[90] K. Jäger, D. N. P. Linssen, O. Isabella, and M. Zeman, *Ambiguities in optical simulations of nanotextured thin-film solar cells using the finite-element method*, Opt. Expr. **23** (2015), A1060–A1071.

[91] T. Itoh and N. Yamauchi, *Surface morphology characterization of pentacene thin film and its substrate with under-layers by power spectral density using fast Fourier transform algorithms*, Appl. Surf. Sci. **253** (2007), 6196–6202.

[92] J.-M. Jin, *The Finite Element Method in Electromagnetics*, 3rd ed., Wiley-IEEE, 2014.

[93] J. Pomplun, S. Burger, L. Zschiedrich, and F. Schmidt, *Adaptive finite element method for simulation of optical nano structures*, Phys. Stat. Sol. B **244** (2007), 3419–3434.

[94] A. Polycarpou, *Introduction to the Finite Element Method in Electromagnetics*, Synthesis Lectures on Computational Electromagnetics, Morgan and Claypool Publishers, 2006.

[95] J.-P. Berenger, *A Perfectly Matched Layer for the Absorption of Electromagnetic Waves*, J. Comput. Phys. **114** (1994), 185–200.

[96] F.-J. Haug and C. Ballif, *Light management in thin film silicon solar cells*, Energy Environ. Sci. **8** (2015), 824–837.

[97] B. Rech, O. Kluth, T. Repmann, T. Roschek, J. Springer, J. Müller, F. Finger, H. Stiebig, and H. Wagner, *New materials and deposition techniques for highly efficient silicon thin film solar cells*, Sol. Energy Mater. Sol. Cells **74** (2002), 439–447.

[98] C. Becker, T. Sontheimer, S. Steffens, S. Scherf, and B. Rech, *Polycrystalline silicon thin films by high-rate electronbeam evaporation for photovoltaic applications – Influence of substrate texture and temperature*, Energy Procedia **10** (2011), 61–65.

[99] A. Ciftja, L. Zhang, T. A. Engh, and A. Kvithyld, *Purification of solar cell silicon materials through filtration*, Rare Metals **25** (2006), 180–185.

[100] M. Kroll, S. Fahr, C. Helgert, C. Rockstuhl, F. Lederer, and T. Pertsch, *Employing dielectric diffractive structures in solar cells – a numerical study*, Phys. Stat. Sol. A **205** (2008), 2777–2795.

[101] S. Wiesendanger, M. Zilk, T. Pertsch, C. Rockstuhl, and F. Lederer, *Combining randomly textured surfaces and photonic crystals for the photon management in thin film microcrystalline silicon solar cells*, Opt. Express **21** (2013), A450–A459.

[102] E. R. Martins, J. Li, Y. Liu, J. Zhou, and T. F. Krauss, *Engineering gratings for light trapping in photovoltaics: The supercell concept*, Phys. Rev. B **86** (2012), 041404(R).

[103] E. R. Martins, J. Li, Y. Liu, V. Depauw, Z. Chen, J. Zhou, and T. F. Krauss, *Deterministic quasi-random nanostructures for photon control*, Nat. Commun. **4** (2013), 2665.

[104] S. Fahr, C. Rockstuhl, and F. Lederer, *Engineering the randomness for enhanced absorption in solar cells*, Appl. Phys. Lett. **92** (2008), 171114.

[105] F. Priolo, T. Gregorkiewicz, M. Galli, and T. F. Krauss, *Silicon nanostructures for photonics and photovoltaics*, Nat. Nanotechnol. **9** (2014), 19–32.

[106] X. Guo, D. Wang, B. Liu, S. Li, and X. Sheng, *Enhanced light absorption in thin film silicon solar cells with Fourier-series based periodic nanostructures*, Opt. Express **24** (2016), A408–A413.

[107] X. Meng, V. Depauw, G. Gomard, O. El Daif, C. Trompoukis, E. Drouard, C. Jamois, A. Fave, F. Dross, I. Gordon, and C. Seassal, *Design, fabrication and optical characterization of photonic crystal assisted thin film monocrystalline-silicon solar cells*, Opt. Express **20** (2012), A465–A475.

[108] S. Nanz, A. Abass, P. M. Piechulla, A. Sprafke, R. B. Wehrspohn, and C. Rockstuhl, *Strategy for tailoring the size distribution of nanospheres to optimize rough backreflectors of solar cells*, Opt. Express **26** (2018), A111–A12, doi:10.1364/OE.26.00A111.

[109] S. M. George, *Atomic Layer Deposition: An Overview*, Chem. Rev. **110** (2010), 111–131.

[110] S. G. Romanov, S. Orlov, D. Ploss, C. K. Weiss, N. Vogel, and U. Peschel, *Engineered disorder and light propagation in a planar photonic glass*, Sci. Rep. **6** (2016), 27264.

[111] Z. C. Holman, M. Filipic, A. Descoeudres, S. De Wolf, F. Smole, M. Topic, and C. Ballif, *Infrared light management in high-efficiency silicon heterojunction and rear-passivated solar cells*, J. Appl. Phys. **113** (2013), 013107.

[112] S. Nanz, A. Abass, P. M. Piechulla, A. Sprafke, R. B. Wehrspohn, and C. Rockstuhl, *Light-Trapping Front Textures for Solar Cells from Tailored Mixtures of Nanospheres: A Numerical Study*, Phys. Stat. Sol. A **215** (2018), 1800699, doi:10.1002/pssa.201800699.

[113] R. Dewan, M. Marinkovic, R. Noriega, S. Phadke, A. Salleo, and D. Knipp, *Light trapping in thin-film silicon solar cells with submicron surface texture*, Opt. Express **17** (2009), 23058.

[114] D. Domine, F.-J. Haug, C. Battaglia, and C. Ballif, *Modeling of light scattering from micro- and nanotextured surfaces*, J. Appl. Phys. **107** (2010), 044504.

[115] M. Zeman, O. Isabella, S. Solntsev, and K. Jäger, *Modelling of thin-film silicon solar cells*, Sol. Energ. Mat. Sol. Cells. **119** (2013), 94–111.

[116] W. H. Southwell, *Pyramid-array surface-relief structures producing antireflection index matching on optical surfaces*, J. Opt. Soc. Am. A **8** (1991), 549–553.

[117] J. A. Dobrowolski, D. Poitras, P. Ma, H. Vakil, and M. Acree, *Toward perfect antireflection coatings: numerical investigation*, Appl. Opt. **41** (2002), 3075–3083.

[118] S. A. Boden and D. M. Bagnall, *Tunable reflection minima of nanostructured antireflective surfaces*, Appl. Phys. Lett. **93** (2008), 133108.

[119] J. Cai and L. Qi, *Recent advances in antireflective surfaces based on nanostructure arrays*, Mater. Horiz. **2** (2015), 37–53.

[120] P. Spinelli, M. A. Verschuuren, and A. Polman, *Broadband omnidirectional antireflection coating based on subwavelength surface Mie resonators*, Nat. Commun. **3** (2012), 1–5.

[121] J.-Q. Xi, F. Schubert, J. K. Kim, E. F. Schubert, M. Chen, S.-Y. Lin, W. Liu, and J. A. Smart, *Optical thin-film materials with low refractive index for broadband elimination of Fresnel reflection*, Nature Phot. **1** (2007), 176–179.

[122] Y. Wang, R. Tummala, L. Chen, L. Qing Guo, W. Zhou, and M. Tao, *Solution-processed omnidirectional antireflection coatings on amorphous silicon solar cells*, J. Appl. Phys. **105** (2009), 103501.

[123] L.-K. Yeh, W.-C. Tian, K.-Y. Lai, and J.-H. He, *Exceptionally omnidirectional broadband light harvesting scheme for multi-junction concentrator solar cells achieved via ZnO nanoneedles*, Sci. Rep. **6** (2016), 39134.

[124] W. Qarony, M. I. Hossain, R. Dewan, S. Fischer, V. B. Meyer-Rochow, A. Salleo, D. Knipp, and Y. H. Tsang, *Approaching Perfect Light Incoupling in Perovskite and Silicon Thin Film Solar Cells by Moth Eye Surface Textures*, Adv. Theory Simul. **1** (2018), 1800030.

[125] K. X. Wang, Z. Yu, V. Liu, Y. Cui, and S. Fan, *Absorption Enhancement in Ultrathin Crystalline Silicon Solar Cells with Antireflection and Light-Trapping Nanocone Gratings*, Nano Lett. **12** (2012), 1616–1619.

[126] V. Magnin, J. Harari, M. Halbwax, S. Bastide, D. Cherfi, and J.-P. Vilcot, *Angle-dependent ray tracing simulations of reflections on pyramidal textures for silicon solar cells*, Solar Energy **110** (2014), 378–385.

[127] S. Sivasubramaniam and M. M. Alkaisi, *Inverted nanopyramid texturing for silicon solar cells using interference lithography*, Microelectron. Eng. **119** (2014), 146–150.

[128] H. M. Branz, V. E. Yost, S. Ward, K. M. Jones, B. To, and P. Stradins, *Nanostructured black silicon and the optical reflectance of graded-density surfaces*, Appl. Phys. Lett. **94** (2009), 231121.

[129] S. Chattopadhyay, Y. F. Huang, Y. J. Jen, A. Ganguly, K. H. Chen, and L. C. Chen, *Antireflecting and photonic nanostructures*, Mater. Sci. Eng. R **69** (2010), 1–35.

[130] Y. Da and Y. Xuan, *Role of surface recombination in affecting the efficiency of nanostructured thin-film solar cells*, Opt. Express **21** (2013), A1065–A1077.

[131] R. S. Bonilla, B. Hoex, P. Hamer, and P. R. Wilshaw, *Dielectric surface passivation for silicon solar cells: A review*, Phys. Stat. Sol. A **214** (2017), 1700293.

[132] S. C. Baker-Finch and K. R. McIntosh, *Reflection of normally incident light from silicon solar cells with pyramidal texture*, Prog. Photovolt: Res. Appl. **19** (2011), 406–416.

[133] K. R. McIntosh and S. C. Baker-Finch, *OPAL 2: Rapid Optical Simulation of Silicon Solar Cells*, Proceedings of the 38th IEEE Photovoltaic Specialists Conference, pp. 000265–000271, IEEE, Austin, 2012.

[134] S. Nanz, R. Schmager, M. G. Abebe, C. Willig, A. Wickberg, A. Abass, G. Gomard, M. Wegener, U. W. Paetzold, and C. Rockstuhl, *Photon Recycling in Nanopatterned Perovskite Thin-Films for Photovoltaic Applications*, APL Photonics **4** (2019), 076104, doi:10.1063/1.5094579.

[135] F. Staub, H. Hempel, J.-C. Hebig, J. Mock, U. W. Paetzold, U. Rau, T. Unold, and T. Kirchartz, *Beyond Bulk Lifetimes: Insights into Lead Halide Perovskite Films from Time-Resolved Photoluminescence*, Phys. Rev. Appl. **6** (2016), 044017.

[136] M. H. Futscher and B. Ehrler, *Efficiency Limit of Perovskite/Si Tandem Solar Cells*, ACS Energy Lett. **1** (2016), 863–868.

[137] W. Tress, *Perovskite Solar Cells on the Way to Their Radiative Efficiency Limit – Insights Into a Success Story of High Open-Circuit Voltage and Low Recombination*, Adv. Energy Mater. **7** (2017), 1602358.

[138] Z. Liu, L. Krückemeier, B. Krogmeier, B. Klingebiel, J. A. Marquez, S. Levcenko, S. Öz, S. Mathur, U. Rau, T. Unold, and T. Kirchartz, *Open-Circuit Voltages Exceeding 1.26 V in Planar Methylammonium Lead Iodide Perovskite Solar Cells*, ACS Energy Lett. **4** (2019), 110–117.

[139] V. Sarritzu, N. Sestu, D. Marongiu, X. Chang, Q. Wang, S. Masi, S. Colella, A. Rizzo, A. Gocalinska, E. Pelucchi, M. L. Mercuri, F. Quochi, M. Saba, A. Mura, and G. Bongiovanni, *Direct or Indirect Bandgap in Hybrid Lead Halide Perovskites?*, Adv. Opt. Mater. **6** (2018), 1701254.

[140] M. A. Green, A. Ho-Baillie, and H. J. Snaith, *The emergence of perovskite solar cells*, Nature Phot. **8** (2014), 506–514.

[141] P. Brenner, M. Stulz, D. Kapp, T. Abzieher, U. W. Paetzold, A. Quintilla, I. A. Howard, H. Kalt, and U. Lemmer, *Highly stable solution processed metal-halide perovskite lasers on nanoimprinted distributed feedback structures*, Appl. Phys. Lett. **109** (2016), 141106.

[142] P. Brenner, T. Glöckler, D. Rueda-Delgado, T. Abzieher, M. Jakoby, B. S. Richards, U. W. Paetzold, I. A. Howard, and U. Lemmer, *Triple cation mixed-halide perovskites for tunable lasers*, Opt. Mater. Express **7** (2017), 4082–4094.

[143] J.-P. Correa-Baena, M. Saliba, T. Buonassisi, M. Grätzel, A. Abate, W. Tress, and A. Hagfeldt, *Promises and challenges of perovskite solar cells*, Science **358** (2017), 739–744.

[144] C. H. Swartz, S. Paul, L. M. Mansfield, and M. W. Holtz, *Absolute photoluminescence intensity in thin film solar cells*, J. Appl. Phys. **125** (2019), 053103.

[145] H. Wang, S.-C. Liu, B. Balachandran, J. Moon, R. Haroldson, Z. Li, A. Ishteev, Q. Gu, W. Zhou, A. Zakhidov, and W. Hu, *Nanoimprinted perovskite metasurface for enhanced photoluminescence*, Opt. Express **25** (2017), A1162–A1171.

[146] I. M. Hossain, D. Hudry, F. Mathies, T. Abzieher, S. Moghadamzadeh, D. Rueda-Delgado, F. Schackmar, M. Bruns, R. Andriessen, T. Aernout, F. Di Giacomo, U. Lemmer, B. S. Richards, U. W. Paetzold, and A. Hadipour, *Scalable Processing of Low-Temperature* TiO_2 *Nanoparticles for High-Efficiency Perovskite Solar Cells*, ACS Appl. Energy Mater. **2** (2019), 47–58.

[147] M. van Eerden, M. Jaysankar, A. Hadipour, T. Merckx, J. J. Schermer, T. Aernouts, J. Poortmans, and U. W. Paetzold, *Optical Analysis of Planar Multicrystalline Perovskite Solar Cells*, Adv. Opt. Mater. **5** (2017), 1700151.

[148] M. A. Green, *Lambertian Light Trapping in Textured Solar Cells and Light-Emitting Diodes: Analytical Solutions*, Prog. Photovolt: Res. Appl. **10** (2002), 235–241.

[149] S. M. Barnett, B. Huttner, R. Loudon, and R. Matloob, *Decay of excited atoms in absorbing dielectrics*, J. Phys. B: At. Mol. Opt. Phys. **29** (1996), 3763–3781.

[150] C. T. Tai and R. E. Collin, *Radiation of a Hertzian Dipole Immersed in a Dissipative Medium*, IEEE Trans. Antennas Propag. **48** (2000), 1501–1506.

[151] H. Chen, S. Nanz, A. Abass, J. Yan, T. Gao, D.-Y. Choi, Y. S. Kivshar, C. Rockstuhl, and D. N. Neshev, *Enhanced Directional Emission from Monolayer* WSe_2 *Integrated onto a Multiresonant Silicon-Based Photonic Structure*, ACS Photonics **4** (2017), 3031–3038, doi:10.1021/acsphotonics.7b00550.

[152] M. Boroditsky, R. Vrijen, T. F. Krauss, R. Coccioli, R. Bhat, and E. Yablonovitch, *Spontaneous Emission Extraction and Purcell Enhancement from Thin-Film 2-D Photonic Crystals*, J. Light. Technol. **17** (1999), 2096–2112.

[153] N. Youngblood and M. Li, *Integration of 2D materials on a silicon photonics platform for optoelectronics applications*, Nanophotonics **6** (2016), 1205–1218.

[154] Z. Sun, A. Martinez, and F. Wang, *Optical modulators with 2D layered materials*, Nat. Photonics **10** (2016), 227–238.

[155] S. Wu, S. Buckley, J. R. Schaibley, L. Feng, J. Yan, D. G. Mandrus, F. Hatami, W. Yao, J. Vučković, and A. Majumdar, *Monolayer semiconductor nanocavity lasers with ultralow thresholds*, Nature **520** (2015), 69–72.

[156] Y. Ye, Z. J. Wong, X. Lu, X. Ni, H. Zhu, X. Chen, Y. Wang, and X. Zhang, *Monolayer excitonic laser*, Nat. Photonics **9** (2015), 733–737.

[157] O. Salehzadeh, M. Djavid, N. H. Tran, I. Shih, and Z. Mi, *Optically pumped two-dimensional* MoS_2 *lasers operating at room-temperature*, Nano Lett. **15** (2015), 5302–5306.

[158] A. Srivastava, M. Sidler, A. V. Allain, D. S. Lembke, A. Kis, and A. Imamoğlu, *Optically active quantum dots in monolayer* WSe_2, Nat. Nanotechnol. **10** (2015), 491–496.

[159] Y.-M. He, G. Clark, J. R. Schaibley, Y. He, M.-C. Chen, Y.-J. Wei, X. Ding, Q. Zhang, W. Yao, and X. Xu, *Single quantum emitters in monolayer semiconductors*, Nat. Nanotechnol. **10** (2015), 497–502.

[160] M. Koperski, K. Nogajewski, A. Arora, V. Cherkez, P. Mallet, J. Y. Veuillen, J. Marcus, P. Kossacki, and M. Potemski, *Single photon emitters in exfoliated* $\mathrm{WSe_2}$ *structures*, Nat. Nanotechnol. **10** (2015), 503–506.

[161] C. Chakraborty, L. Kinnischtzke, K. M. Goodfellow, R. Beams, and A. N. Vamivakas, *Voltage-controlled quantum light from an atomically thin semiconductor*, Nat. Nanotechnol. **10** (2015), 507–511.

[162] T. T. Tran, K. Bray, M. J. Ford, M. Toth, and I. Aharonovich, *Quantum emission from hexagonal boron nitride monolayers*, Nat. Nanotechnol. **11** (2016), 37–41.

[163] A. Pospischil, M. M. Furchi, and T. Mueller, *Solar-energy conversion and light emission in an atomic monolayer p-n diode*, Nat. Nanotechnol. **9** (2014), 257–261.

[164] J. S. Ross, P. Klement, A. M. Jones, N. J. Ghimire, J. Yan, D. G. Mandrus, T. Taniguchi, K. Watanabe, K. Kitamura, W. Yao, D. H. Cobden, and X. Xu, *Electrically tunable excitonic light-emitting diodes based on monolayer* $\mathrm{WSe_2}$ *p-n junctions*, Nat. Nanotechnol. **9** (2014), 268–272.

[165] Y.-M. He, O. Iff, N. Lundt, V. Baumann, M. Davanco, K. Srinivasan, S. Höfling, and C. Schneider, *Cascaded emission of single photons from the biexciton in monolayered* $\mathrm{WSe_2}$, Nat. Commun. **7** (2016), 13409.

[166] L. M. Malard, T. V. Alencar, A. P. M. Barboza, K. F. Mak, and A. M. de Paula, *Observation of intense second harmonic generation from* $\mathrm{MoS_2}$ *atomic crystals*, Phys. Rev. B **87** (2013), 201401.

[167] Y. Li, Y. Rao, K. F. Mak, Y. You, S. Wang, C. R. Dean, and T. F. Heinz, *Probing Symmetry Properties of Few-Layer* $\mathrm{MoS_2}$ *and* $\mathrm{h-BN}$ *by Optical Second-Harmonic Generation*, Nano Lett. **13** (2013), 3329–3333.

[168] C. Janisch, Y. Wang, D. Ma, N. Mehta, A. L. Elías, N. Perea-López, M. Terrones, V. Crespi, and Z. Liu, *Extraordinary second harmonic generation in tungsten disulfide monolayers*, Sci. Rep. **4** (2014), 5530.

[169] G. Wang, X. Marie, I. Gerber, T. Amand, D. Lagarde, L. Bouet, M. Vidal, A. Balocchi, and B. Urbaszek, *Giant enhancement of the optical second-harmonic emission of* $\mathrm{WSe_2}$ *monolayers by laser excitation at exciton resonances*, Phys. Rev. Lett. **114** (2015), 097403.

[170] M. Weismann and N. C. Panoiu, *Theoretical and computational analysis of second-and third-harmonic generation in periodically patterned graphene and transition-metal dichalcogenide monolayers*, Phys. Rev. B **94** (2016), 035435.

[171] H. Chen, V. Corboliou, A. S. Solntsev, D.-Y. Choi, M. A. Vincenti, D. de Ceglia, C. De Angelis, Y. Lu, and D. N. Neshev, *Enhanced second harmonic generation from two-dimensional* $\mathrm{MoSe_2}$ *on a silicon waveguide*, Light. Sci. Appl. **6** (2017), e17060.

[172] Q. H. Wang, K. Kalantar-Zadeh, A. Kis, J. N. Coleman, and M. S. Strano, *Electronics and optoelectronics of two-dimensional transition metal dichalcogenides*, Nat. Nanotechnol. **7** (2012), 699–712.

[173] G. Xia, H. Wang, D. Xiao, M. Dubey, and A. Ramasubramaniam, *Two-dimensional material nanophotonics*, Nat. Photonics **8** (2014), 899–907.

[174] K. F. Mak and J. Shan, *Photonics and optoelectronics of 2D semiconductor transition metal dichalcogenides*, Nat. Photonics **10** (2016), 216–226.

[175] J. S. Ponraj, Z.-Q. Xu, S. C. Dhanabalan, H. Mu, Y. Wang, J. Yuan, P. Li, S. Thakur, M. Ashrafi, K. Mccoubrey, Y. Zhang, S. Li, H. Zhang, and Q. Bao, *Photonics and optoelectronics of two-dimensional materials beyond graphene*, Nanotechnology **27** (2016), 462001.

[176] A. Sobhani, A. Lauchner, S. Najmaei, C. Ayala-Orozco, F. Wen, J. Lou, and N. J. Halas, *Enhancing the photocurrent and photoluminescence of single crystal monolayer* MoS_2 *with resonant plasmonic nanoshells*, Appl. Phys. Lett. **104** (2014), 031112.

[177] S. Najmaei, A. Mlayah, A. Arbouet, C. Girard, J. Léotin, and J. Lou, *Plasmonic Pumping of Excitonic Photoluminescence in Hybrid* MoS_2–Au *Nanostructures*, ACS Nano **8** (2014), 12682–12689.

[178] S. Butun, S. Tongay, and K. Aydin, *Enhanced light emission from large-area monolayer* MoS_2 *using plasmonic nanodisc arrays*, Nano Lett. **15** (2015), 2700–2704.

[179] G. M. Akselrod, T. Ming, C. Argyropoulos, T. B. Hoang, Y. Lin, X. Ling, D. R. Smith, J. Kong, and M. H. Mikkelsen, *Leveraging nanocavity harmonics for control of optical processes in 2D semiconductors*, Nano Lett. **15** (2015), 3578–3584.

[180] D.-H. Lien, J. S. Kang, M. Amani, K. Chen, M. Tosun, H.-P. Wang, T. Roy, M. S. Eggleston, M. C. Wu, and M. Dubey, *Engineering light outcoupling in 2D materials*, Nano Lett. **15** (2015), 1356–1361.

[181] H. Chen, J. Yang, E. Rusak, J. Straubel, R. Guo, Y. W. Myint, J. Pei, M. Decker, I. Staude, C. Rockstuhl, Y. Lu, Y. S. Kivshar, and D. Neshev, *Manipulation of photoluminescence of two-dimensional* $MoSe_2$ *by gold nanoantennas*, Sci. Rep. **6** (2016), 22296.

[182] Z. Wang, Z. Dong, Y. Gu, Y.-H. Chang, L. Zhang, L.-J. Li, W. Zhao, G. Eda, W. Zhang, G. Grinblat, S. A. Maier, J. K. W. Yan, C.-W. Qiu, and A. T. S. Wee, *Giant photoluminescence enhancement in tungsten-diselenide–gold plasmonic hybrid structures*, Nat. Commun. **7** (2016), 11283.

[183] S. Wu, S. Buckley, A. M. Jones, J. S. Ross, N. J. Ghimire, J. Yan, D. G. Mandrus, W. Yao, F. Hatami, J. Vučković, A. Majumdar, and X. Xu, *Control of two-dimensional excitonic light emission via photonic crystal*, 2D Mater. **1** (2014), 011001.

[184] Y. J. Noori, Y. Cao, J. Roberts, C. Woodhead, R. Bernardo-Gavito, P. Tovee, and R. J. Young, *Photonic Crystals for Enhanced Light Extraction from 2D Materials*, ACS Photonics **3** (2016), 2515–2520.

[185] T. Galfsky, Z. Sun, C. R. Considine, C.-T. Chou, W.-C. Ko, Y.-H. Lee, E. E. Narimanov, and V. M. Menon, *Broadband enhancement of spontaneous emission in two-dimensional semiconductors using photonic hypercrystals*, Nano Lett. **16** (2016), 4940–4945.

[186] X. Gai, D.-Y. Choi, and B. Luther-Davies, *Negligible nonlinear absorption in hydrogenated amorphous silicon at 1.55 μm for ultra-fast nonlinear signal processing*, Opt. Express **22** (2014), 9948–9958.

[187] J. A. Schuller, S. Karaveli, T. Schiros, K. He, S. Yang, I. Kymissis, J. Shan, and R. Zia, *Orientation of luminescent excitons in layered nanomaterials*, Nat. Nanotechnol. **8** (2013), 271–276.

[188] T. Yan, X. Qiao, X. Liu, P. Tan, and X. Zhang, *Photoluminescence properties and exciton dynamics in monolayer* $\mathrm{WSe_2}$, Appl. Phys. Lett. **105** (2014), 101901.

[189] A. Vaskin, S. Mashhadi, M. Steinert, K. E. Chong, D. Keene, S. Nanz, A. Abass, E. Rusak, D.-Y. Choi, I. Fernandez-Corbaton, T. Pertsch, C. Rockstuhl, M. A. Noginov, Y. S. Kivshar, D. N. Neshev, N. Noginova, and I. Staude, *Manipulation of Magnetic Dipole Emission from* $\mathrm{Eu^{3+}}$ *with Mie-Resonant Dielectric Metasurfaces*, Nano Lett. **19** (2019), 1015–1022, doi:10.1021/acs.nanolett.8b04268.

[190] N. Noginova, G. Zhu, M. Mayy, and M. A. Noginov, *Magnetic dipole based systems for probing optical magnetism*, J. Appl. Phys. **103** (2008), 07E901.

[191] X. Ni, G. V. Naik, A. V. Kildishev, Y. Barnakov, A. Boltasseva, and V. M. Shalaev, *Effect of metallic and hyperbolic metamaterial surfaces on electric and magnetic dipole emission transitions*, Appl. Phys. B: Lasers Opt. **103** (2011), 553.

[192] L. Aigouy, A. Cazé, P. Gredin, M. Mortier, and R. Carminati, *Mapping and Quantifying Electric and Magnetic Dipole Luminescence at the Nanoscale*, Phys. Rev. Lett. **113** (2014), 076101.

[193] R. Hussain, S. S. Kruk, C. E. Bonner, M. A. Noginov, I. Staude, Y. S. Kivshar, N. Noginova, and D. N. Neshev, *Enhancing* $\mathrm{Eu^{3+}}$ *magnetic dipole emission by resonant plasmonic nanostructures*, Opt. Lett. **40** (2015), 1659.

[194] B. Choi, M. Iwanaga, Y. Sugimoto, K. Sakoda, and H. T. Miyazaki, *Selective Plasmonic Enhancement of Electric- and Magnetic-Dipole Radiations of* Er *Ions*, Nano Lett. **16** (2016), 5191.

[195] S. Murai, M. Saito, H. Sakamoto, M. Yamamoto, R. Kamakura, T. Nakanishi, K. Fujita, M. A. Verschuuren, Y. Hasegawa, and K. Tanaka, *Directional outcoupling of photoluminescence from* Eu(III)*-complex thin films by plasmonic array*, APL Photon. **2** (2017), 026104.

[196] M. Kasperczyk, S. Person, D. Ananias, L. D. Carlos, and L. Novotny, *Excitation of Magnetic Dipole Transitions at Optical Frequencies*, Phys. Rev. Lett. **114** (2015), 163903.

[197] N. R. Brewer, Z. N. Buckholtz, Z. J. Simmons, E. A. Mueller, and D. D. Yavuz, *Coherent Magnetic Response at Optical Frequencies Using Atomic Transitions*, Phys. Rev. X **7** (2017), 011005.

[198] S. Karaveli and R. Zia, *Spectral Tuning by Selective Enhancement of Electric and Magnetic Dipole Emission*, Phys. Rev. Lett. **106** (2011), 193004.

[199] R. Hussain, D. Keene, N. Noginova, and M. Durach, *Spontaneous emission of electric and magnetic dipoles in the vicinity of thin and thick metal*, Opt. Express **22** (2014), 7744.

[200] M. K. Schmidt, R. Esteban, J. J. Sáenz, I. Suárez-Lacalle, S. Mackowski, and J. Aizpurua, *Dielectric antennas - a suitable platform for controlling magnetic dipolar emission*, Opt. Express **20** (2012), 13636.